APPLICATIONS OF FUMED SILICA INTEGRATING CAVITIES

A Dissertation

by

JOHN DAVID MASON

Submitted to the Office of Graduate and Professional Studies of
Texas A&M University
in partial fulfillment of the requirements for the degree of

DOCTOR OF PHILOSOPHY

Chair of Committee,	Edward S. Fry
Committee Members,	George W. Kattawar
	Aleksei M. Zheltikov
	Vladislav V. Yakovlev
Head of Department,	Peter M. McIntyre

December 2016

Major Subject: Physics

ABSTRACT

Integrating cavities have been used in radiometric and photometric measurements since their creation by Frederick Ulbricht in 1900. Modern commercial integrating cavities use Spectralon, a PTFE-based diffuse reflector with a reflectivity $> 97.5\%$ from 350-1600 nm, as a diffuse reflector. However, Spectralon's reflectivity diminishes in the ultraviolet which limits the potential for short wavelength experiments. The high reflectivity of a recently characterized diffuse reflector, fumed silica, in the UV, as well as the VIS-NIR, has improved the sensitivity of integrating cavity based measurements.

With the increased ultraviolet reflectivity, measurements of the optical absorption coefficient of pure water were performed using an improved version of the Integrating Cavity Absorption Meter (ICAM), the ICAM-II. The ICAM-II replaces Spectralon of the inner and outer cavity from the original ICAM with fumed silica powder. The fumed silica diffuse reflector, along with increased volume in the sample region, extended the optical pathlength by a factor of 2.5 at 532 nm and much more in the UV at 250 nm. Scattering-independent measurements of the absorption coefficient of pure water from 250-550 nm were made with this instrument.

Furthermore, the increased reflectivity of fumed silica, the new scattering-independent integrating cavity ring-down spectroscopy technique can be applied to measuring the absorption coefficient of highly scattering media. ICRDS measurements were made of various biological cells and tissues. The results from these measurements were compared with the well-established Inverse Adding-Doubling (IAD) technique.

DEDICATION

To my parents, my sister and her fiancé, Christie and Trey, my loving fiancé, Emily, and her family, my many mentors along the way, and Dr. John Bevan

ACKNOWLEDGEMENTS

The research provided in this dissertation was performed with the help and assistance of many different people from many different points in my life. I had always had a passion for science from a young age. It was not until high school however that I discovered my passion for physics. During my junior year of high school, I took my first physics course from a teacher named Mr. David Wright. Mr Wright pushed me to explore my curiosity and helped me to discover my desire for a career in physics. From there, I continued my education at Rensselaer Polytechnic Institute where I pursued a bachelor's of science in physics. There, I met a professor named Dr. Jim Napolitano. Dr. Napolitano provided me with my initial research experience and afforded me the opportunity to join a multinational collaboration in Daya Bay, China. Because of my experiences in Dr. Napolitano's lab, I knew that I wanted to further my education and pursue a PhD in Physics at Texas A&M University.

I initially came to Texas A&M to study high energy physics. I was first introduced to Dr. Fry in August of 2011 when I recognized his name from a paper published by Pope and Fry which measured the absorption coefficient of pure water from 380-700 nm. Dr. Fry has been a phenomenal mentor who has pushed me to grow as a scientist and as a person. He has taught me the the meticulousness and patience required to make a sensitive measurement. In addition to Dr. Fry, my committee, Dr. George Kattawar, Dr. Aleksei Zheltikov, Dr. Vladislav Yakovlev and Dr. John Bevan (whose untimely passing has left a huge hole in the community) has served as an exceptional resource along the way. Furthermore, the support staff of Texas A&M has provided countless hours to ensure that I could efficiently spend my time focused on my research. I must specifically thank Veronica Rodriguez, Jay Jones, Cheryl Picone, Minnette Bilbo, Yasa Rathnayaka,

Michelle Sylvester Barbara Siems, Garrick Garza, John Newkirk, Steve Payne, James Kirby and Bill Merka.

I must thank the tremendous support from the many of my fellow graduate students and faculty who supported me along the way. In particular, I must thank Michael Cone, Ellie Figueroa, Brett Hokr, Jonathan Thompson, Joel Bixler, Dawson Nodurft, Xinmei Qu, Ryan Mueller, Jacob Gayles, Sean Wu, James Gerity, Jeff Roe, Frank Echeveria, Dr. Tatiana Erukhimova, and Michael Mehlman.

My most sincerest gratitude must be extended to my parents. My mother served as my emotional support for every year of my life. She has endured my constant stress induced rants and always knows the right things to say. My father has provided tremendous technical discussions and always offered insight as to new avenues to explore in research. I must also recognize my sister, Christie, and her fiance, Trey. My sister has always provided me with important moral support and valuable mental breaks from work. Trey's timely sense of humor coupled with his positive attitude was always helpful in alleviating the stress of work. The contributions from the newest members of my family have not gone unnoticed. Sarah and John Winston have been incredibly supportive and treated me like their own son. The trips to North Carolina with them have allowed me to refresh my mind during the most stressful of situations.

Finally, during my time at graduate school, I have begun to build a family that has been incredibly supportive while I conducted my research. My cat, Yoda, has been with me since he was two days old. His laid back attitude and constant quest for food has given me laughs on my worst days. My dog, Ernie, has been a constant companion who enjoys snuggling in bed and long car rides. He has been a great friend who has helped to take data during many long nights. Finally, my wonderful fiance, Emily Winston, has been my best friend, confidante, and teammate during this study. She has provided dinners, laughs, movies, support, and most importantly love. I am extremely fortunate to have her and

excited for our future together.

CONTRIBUTORS AND FUNDING SOURCES

Contributors

This work was supervised by a dissertation committee consisting of Professor Edward S. Fry [advisor], Professor George W. Kattawar of the Department of Physics and Astronomy, Professor Aleksei M. Zheltikov of the Department of Physics and Astronomy, and Dr. Vladislav V. Yakovlev of the Department of Physics and Astronomy and the Department of Biomedical Engineering.

The derivations in Chapter IV were initially performed by Dr. Edward S. Fry, Dr. George W. Kattawar, and Dr. Robin M. Pope of the Department of Physics and were published in 1992. The initial characterization of the fumed silica diffuse reflector was carried out by Dr. Michael T. Cone of the Department of Physics and Astronomy and was published in 2015.

All other work conducted for the dissertation was completed by the student independently.

Funding Sources

This work was made possible in part by the National Science Foundation (NSF) under grant number 1333425, the Oak Ridge Institute for Science and Education, TASC Inc., the George P. Mitchell Chair in Experimental Physics and the Herman F. Heep and Minnie Belle Heep Texas A&M University Endowed Fund.

NOMENCLATURE

V	Volts
A	Amperes
ICRDS	Integrating Cavity Ring-Down Spectroscopy
CRDS	Cavity Ring-Down Spectroscopy
IAD	Inverse Adding Doubling
ICAM	Integrating Cavity Absorption Meter
LIA	Lock-In Amplifier
ASTM	American Society for Testing and Materials
ISO	International Organization for Standardization
USP	United States Pharmacopoeia
CLSI	Clinical and Laboratory Standards Institute
TOC	Total Organic Carbon
VI	Visual Interface
PMT	Photomultiplier Tube
P	Pressure
T	Time

TABLE OF CONTENTS

LIST OF FIGURES

LIST OF TABLES

CHAPTER I

INTRODUCTION

The interaction of light and matter contains important information about the structure of atoms and molecules. Spectroscopy, the study of the interaction between matter and electromagnetic radiation, is a useful tool to investigate the atoms and molecules involved in many different interdisciplinary phenomena ranging from atomic chemistry to molecular biology [18, 79]. Details about the energy structure of electronic transitions, vibrational and rotational modes, and atomic composition can be ascertained by probing atoms and molecules with different frequencies of light [23]. Since the structure of molecules and atoms can be complex, different spectroscopic techniques have been developed to investigate the structure of an atom or molecule at different photon energies. These techniques include, but are not limited to, Raman spectroscopy, emission spectroscopy, and absorption spectroscopy [20].

Each of these techniques exploits a different physical phenomena to probe the energy structure of a sample. When the interaction between light and the sample is weak, the signal can be enhanced by passing light through large sample volumes. This is referred to as increasing the path length. For situations where increasing the sample volume is impractical or cost-prohibitive, the path length can be artificially increased by placing the sample in an optical cavity. In a traditional two-mirror cavity, light bounces between two mirrors and interacts with the sample each time it traverses the length of the cavity [3, 32, 53, 82]. If the sample has strong scattering properties, light will be lost through the sides of the cavity with each pass. This problem can be fixed by employing a three dimensional cavity that reflects light back through the sample even if it is scattered. An example of a three dimensional cavity is an integrating sphere which will be introduced in

the next section.

Integrating Cavities

Integrating cavities have been a staple in photometric measurements since their creation by Frederick Ulbricht in 1900. Ulbricht had been attempting to find the best way to light railway stations when he observed that in a hollow sphere, the wall illumination is proportional to the total luminous flux [54, 27]. Independently, William Edward Sumpner was developing the theory for an integrating cavity used in a field of light measurement. Sumpner published his work for a box geometry in 1910 [74]. An integrating cavity consists of an enclosed structure whose walls are coated with a diffuse reflector. Diffuse reflection is different than specular reflection from a mirror. In specular reflection, the angle of incidence with respect to the normal of the surface is equal to the angle of reflection. In contrast, diffuse reflection occurs when the incident light is reflected at all angles from the surface. Specular reflection is usually caused by reflection from smooth surfaces while diffuse reflection is caused by reflection from rough surfaces. A schematic demonstrating the difference between specular and diffuse reflection is shown in Fig. I.1

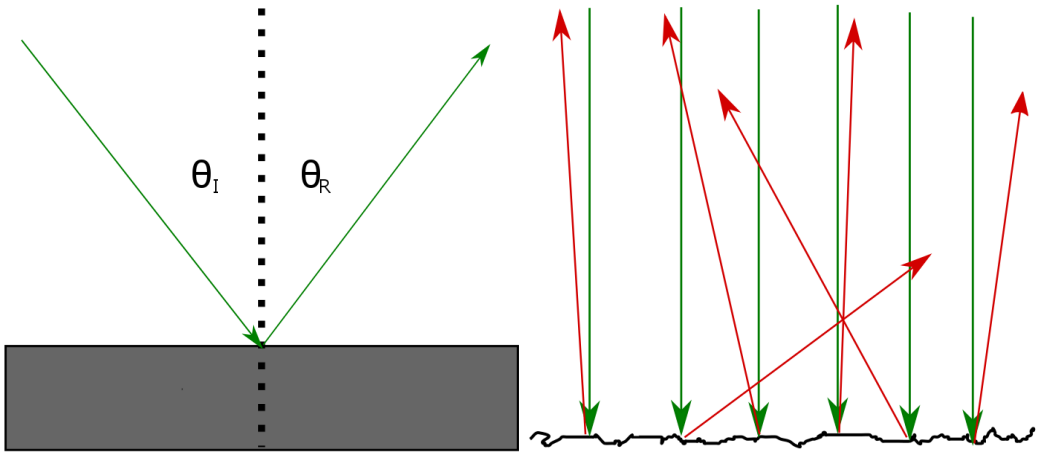

Figure I.1: (Left) A representation of the specular reflection from a mirror with θ_I representing the incident angle and θ_R representing the reflected angle. (Right) A representation of a diffuse reflector.

A special case of diffuse reflector is called a Lambertian reflector. A Lambertian reflector is an ideal diffuse reflector where the observed intensity is directly proportional to the cosine of the angle between the normal to the surface and the reflected light [43] (see Fig. I.2). In simpler terms, the apparent brightness of a reflection from a Lambertian surface is the same to an observer regardless of their viewing angle.

Integrating spheres are typically made from (nearly) Lambertian reflectors. Light reflected from the wall of a spherical integrating cavity will irradiate all other points equally [77]. As a result, an isotropic and homogeneous illumination will be generated after only a few bounces from the cavity wall. A uniform illumination from a cavity with an arbitrary geometry can be similarly obtained if the cavity reflectivity is sufficiently large [21].

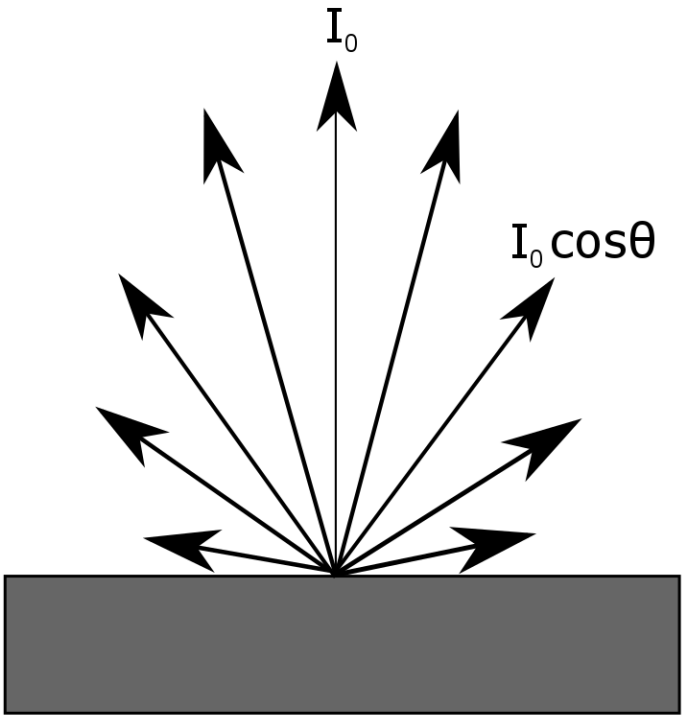

Figure I.2: A model of the reflection of optical radiation from a quartz surface

The most commonly used integrating cavity is manufactured by Labsphere. Labsphere integrating cavities use a PTFE based diffuse reflector called, Spectralon. Spectralon is quoted as having "the highest diffuse reflectance of any known material or coating over the UV-VIS-NIR region of the spectrum" [41]. In 2015, Cone et al. characterized a new diffuse reflector based on fumed silica powder with improved reflectivity over the ultra-violet and visible spectrum [17]. This improved reflectivity has been used to increase sensitivity in Raman, Emission, and Absorption Spectroscopy [7, 16]. This dissertation will extensively investigate improvements in Absorption Spectroscopy through the use of fumed silica powder. However, the success of fumed silica integrating cavities in Raman and Emission Spectroscopy will be highlighted first.

Raman Spectroscopy

Raman spectroscopy measures the inelastic scattering of a photon from vibrational modes of a molecule. When incident light is Raman scattered, energy is transferred between a photon and a molecule. There are two cases of Raman scattering to discuss. First, consider a molecule in the ground state. Light from a monochromatic source illuminates a pure molecular sample. A small fraction of the incident photons transfer energy from the photon to the molecule when scattered from the sample. As a result, the molecule is excited to a higher vibrational state and the Raman scattered photon loses energy. These lower energy Raman photons have a lower frequency (longer wavelength) than the incident photons. The transfer of energy *from* the photon *to* the molecule is referred to as Stokes Raman Scattering.

Similarly, energy can be transferred *from* the molecule *to* the photon through Raman scattering. In this scenario, the molecule starts in an excited vibrational state and falls to a lower energy level when it transfers energy to an incident photon. The scattered photon has more energy than the incident photons and has a higher frequency (shorter wavelength) than the incident light. This is called Anti-Stokes Raman Scattering. Fig. I.3 highlights the difference between these Raman phenomena [75].

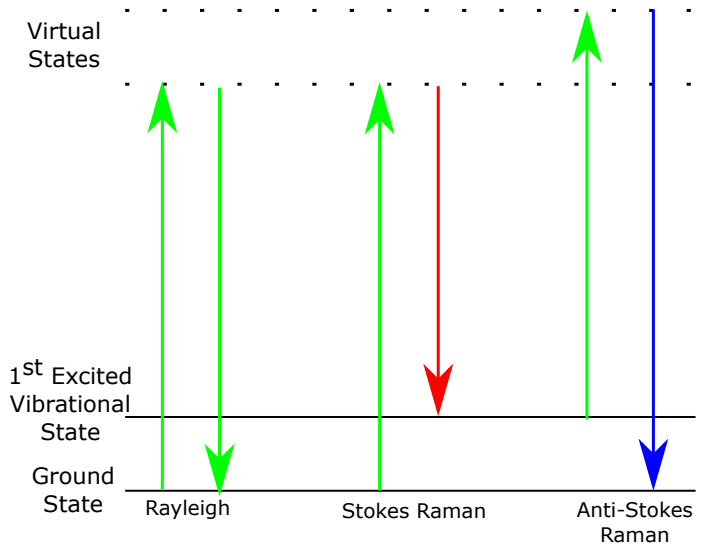

Figure I.3: An energy level diagram of Stokes and Anti-Stokes Raman Scattering

In both Stokes and Anti-Stokes Raman scattering, the difference between the energy of the excited vibrational state and the energy of the lower state is directly proportional to the Raman frequency shift. This follows directly from the first principles of conservation of energy. Therefore, Raman photons contain detailed information about the vibrational structure of an atom. However, spontaneous Raman is very weak [33]. Therefore, the detection of Raman scattered photons can be difficult especially under the background of Rayleigh scattered incident photons. While Rayleigh scattered light can be eliminated using a notch (or edge) filter, Raman photons may still be too weak for detection. Two recent innovations have improved the detection ability of Raman photons; (1) stimulated Raman and (2) integrating cavity enhancement. Stimulated Raman has a much larger signal than spontaneous Raman and is easily detected. However, stimulated Raman requires a high intensity incident laser which can be ill-suited for more delicate samples. Conversely, placing the sample in an integrating cavity increases the generation of Raman photons due to a longer sample path length. Light reflected from the cavity wall passes through

the sample multiple times generating new Raman photons with each pass. Furthermore, since light is already scattered diffusely from the cavity wall, additional Rayleigh scattering caused by the sample has no effect on the interaction. By placing a laser line filter in front of the detector, only the Raman photons will be detected. Fig. I.4 shows the Raman signal generated from a barium sulfate integrating cavity. The input laser light has been filtered using a 532 nm notch filter. The yellow light represents Raman scattered photons that have been generated using cavity enhancement.

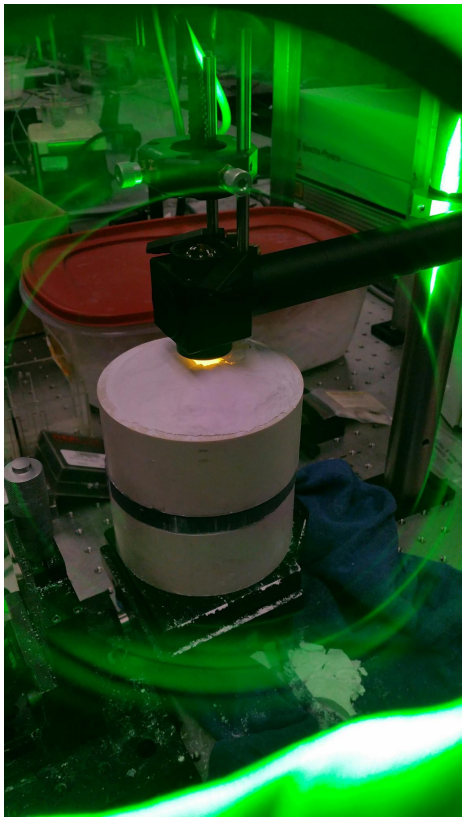

Figure I.4: Raman scattered photons from a Barium sulfate integrating cavity

Emission Spectroscopy

Emission Spectroscopy has been in existence since the discovery of the spectroscope by Joseph von Fraunhofer in 1814. Fraunhofer's spectroscope used homemade diffraction glass to spatially separate the individual wavelengths from a broadband spectrum. Fraunhofer used his spectroscope to characterize 574 fixed discrete lines of the solar spectrum which led to the discovery of helium. Fraunhofer had discovered that excited atoms emit discrete bands (or wavelengths). By separating and characterizing these emission bands, the atomic composition of a source can be determined [23].

Atomic emission occurs when an atom transitions from an excited state to a lower atomic energy level. When this transition occurs, a photon with an energy equal to the difference between the energy levels is produced to satisfy conservation of energy. Because of the limited number of energy transitions for a pure atomic sample, the emission spectrum for that sample will be filled with many narrow-band discrete lines. In contrast, the complex structure of molecules greatly increases the number of allowable transitions. Since many of these lines are closely spaced, the emission spectra of even simple molecules can appear continuous.

While fluorescent emission is much stronger than Raman, a similar integrating cavity scheme can be used for detection of trace compounds. Bixler et al. showed that by adding a fluorescent immunoassay to a water sample, trace amounts of urobilin (a bio-marker for human waste) can be detected from fluorescent emission [7]. When the sample was enhanced using a fumed silica integrating cavity, sub-picomolar concentrations of urobilin were detected. A picture of the enhanced fluorescence is shown in Fig. I.5.

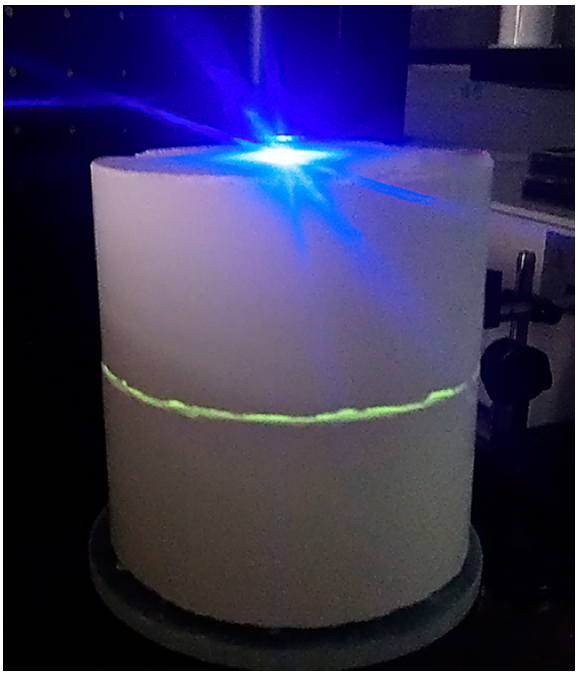

Figure I.5: Fluorescent emission from urobilinogen in a pure water sample. The cavity was excited with a 488 nm diode (blue light) through the top of the cavity. The green fluorescent emission can be seen along the seam of the two cavity halves. Reprinted with permission from [7].

Absorption Spectroscopy

Absorption Spectroscopy is the inverse of Emission Spectroscopy. While Emission Spectroscopy measures the transition of an electron in an atom (molecule) from an excited state to a lower state, Absorption Spectroscopy measures the transition of an electron from the ground state to an excited state. Absorption Spectroscopy involves first measuring the reference spectrum of a radiation source with a detector. The reference spectrum characterizes the emitted spectrum of the radiation as well as the radiation's response to experimental conditions. A sample cell is then placed between the source and the detector and the spectrum is remeasured. Radiation is "removed" from the source beam through absorption by the sample. The amount of light removed at each wavelength/frequency is

dependent on the optical characteristics of the sample. The absorption of the sample is calculated by subtracting the measured spectrum of the radiation source after interacting with the sample from the reference spectrum.

There are many different methods for measuring the absorption spectrum of an atom or molecule. Techniques are chosen based on characteristics such as the wavelength region of interest, the strength of the transitions in that region, and other inherent optical properties such as scattering. One such method involves using an integrating cavity to measure the absorption coefficient of a sample in that cavity. The absorption is measured by observing the decrease in the radiation density due to sample absorption [21]. Recent advancements in integrating cavity technology have enhanced the ability to measure the absorption of samples[17, 16]. The objective of this dissertation is to investigate the absorption spectrum of several weakly absorbing compounds using various methods centered around fumed silica integrating cavities.

This manuscript describes the use of the recently characterized diffuse reflector, fumed silica, to measure the absorption spectra for materials that suffer from severe scattering and/or weak absorption. Different integrating cavity measurement schemes allow for accurate characterization of the absorption coefficients for pure water, various biological cells, live tissue, synthetic tissue, and tissue that has been fixed using a fixing agent. These samples have been measured using two distinct techniques: (1) the Integrating Cavity Absorption Meter (ICAM) and (2) Integrating Cavity Ring-Down Spectroscopy (ICRDS).

The ICAM involves injecting a monochromatic continuous-wave source into a pair of concentric integrating cavities. In this scheme, the absorption coefficient of a sample is determined by comparing the cavity irradiance of an empty cavity with that of a sample filled cavity. This manuscript will present the ultraviolet absorption spectrum of pure water from 250-550 nm. The absorption spectrum of water has been well established from 400-550 nm but discrepancies remain for 250-400 nm. This absorption spectrum will be

discussed and compared with established literature values.

Conversely, ICRDS involves injecting a temporally short pulse into an integrating cavity and observing how the pulse decays in time. By comparing the pulse decay time in a cavity containing a sample with the pulse decay time of an empty cavity, the absorption can be determined. The absorption coefficient of Chinese Hamster Ovary (CHO-K1) cells, synthetic human skin tissue (pigmented to resemble Caucasian skin tissue), live tissue from a pig brain, and fixed pig brain tissue were measured using ICRDS. The absorption spectra of these samples from 420-700 nm are presented in this manuscript.

Chapter 2 describes the fumed silica diffuse reflector in detail and discusses how the powder is formed into a usable structure. In Chapter 3, the reader is introduced to the importance of the absorption spectrum of pure water as well as a brief history of the previous results. The various physical phenomena responsible for the different wavelength regions are also discussed. Chapter 4 describes the ICAM-II design that was used to measure the ultraviolet absorption spectrum of pure water. Chapter 5 details how an ICAM measurement is performed and describes the equations necessary to find a value for the absorption coefficient. Chapter 6 presents the complete absorption spectrum for pure water and compares the results with other attempts to measure this region. Chapter 7 details the possible sources of error in an ICAM measurement and the steps made to minimize the effects of this error. Chapter 8 introduces ICRDS and compares it with the well-known cavity ring-down spectroscopy (CRDS). Chapter 9 describes the experimental requirements for an ICRDS measurement. Chapter 10 shows the absorption spectrum of CHO-K1 cells measured using ICRDS. In Chapter 11, the difference between measuring a liquid sample and measuring a solid sample using ICRDS is highlighted. An alternate technique is also introduced to measuring skin samples, Inverse Adding Doubling (IAD), which has been used extensively to measure the optical properties of tissue for over 2 decades. Chapter 12 explores an alternative diffuse reflector to quartz powder that would be more robust and

better equipped to handle the rigors of in-field use. Finally, in Chapter 13, a brief summary of the results is provided.

CHAPTER II

DEVELOPMENT AND USE OF FUMED SILICA AS A DIFFUSE REFLECTOR

Due to the diminishing performance of Spectralon in the ultraviolet spectrum, fumed silica has been established as a highly effective ultraviolet diffuse reflector. This work was been well characterized by Cone et al [17]. Integrating cavities made from fumed silica (quartz powder) will be used extensively in this work so a brief review of the results from Cone et al. is necessary.

Theoretical Model for Fumed Silica Diffuse Reflector

A simple model to demonstrate the effectiveness of quartz powder as a diffuse reflector can be constructed by first considering the light reflection from a quartz glass plate as shown in Fig. II.1. At the front surface of the plate, a small fraction of light, ρ, is reflected due to an index mismatch between the air-quartz interface. The remaining light is transmitted to the back surface of the quartz glass. At the back surface, the majority of light is transmitted. However, a fraction, ρ, is reflected back towards the front surface. When that reflected light reaches the front surface, it is again reflected and transmitted similar to previous reflections. For simplicity, absorption and interference effects have been neglected. The reflectance, R, can be mathematically expressed by

$$R = \frac{2\rho}{1+\rho} \tag{II.1}$$

Note that the index of refraction of quartz is 1.486 while the index of refraction of air is 1.000 and the reflectivity at normal incidence is [49, 22]

$$\rho = (\frac{n_{quartz} - n_{air}}{n_{quartz} + n_{air}})^2. \tag{II.2}$$

As a result, approximately 4% of the light incident on any quartz-air interface is reflected. If the material were to have a higher index of refraction, then more light would be reflected at each boundary.

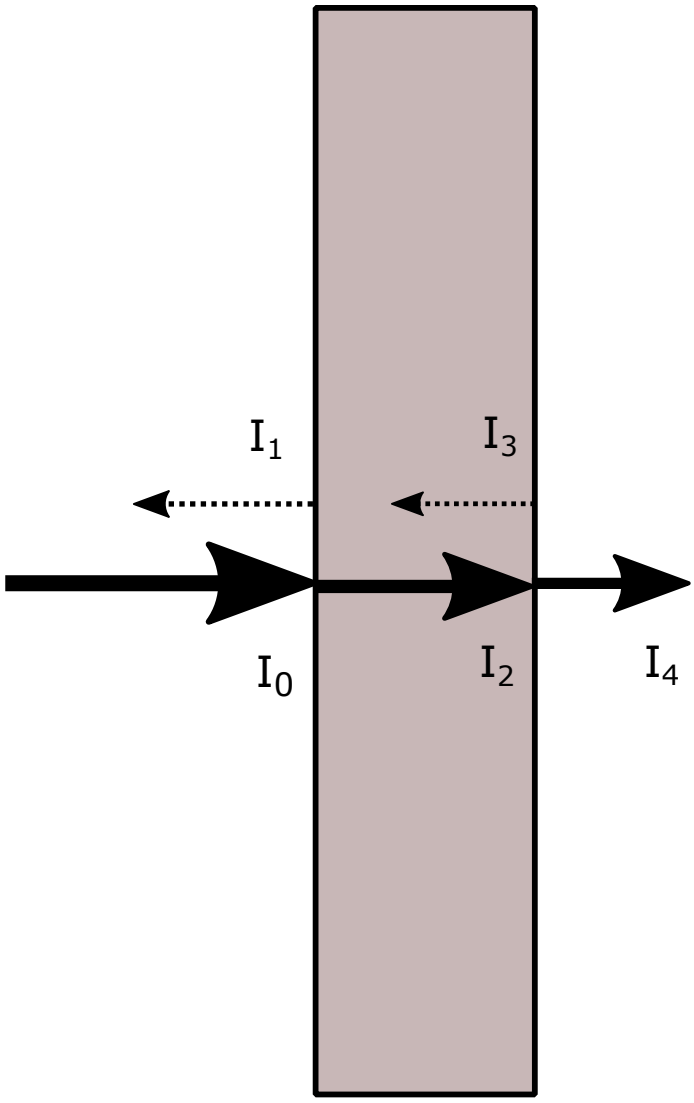

Figure II.1: A model of the reflection of optical radiation from a quartz surface

We next consider a set of N stacked quartz glass plates. Between each plate, an air gap exists. The reflectivity for normal incidence at any individual air-quartz interface is again denoted by ρ. Absorption and interference effects are also neglected. Let I_n be the intensity of light in the n^{th} position where I_0 is the initial intensity of the incident light and I_1 is the total reflected light from the entire stack of plates. A detailed representation of the position locations is shown in Fig. II.2.

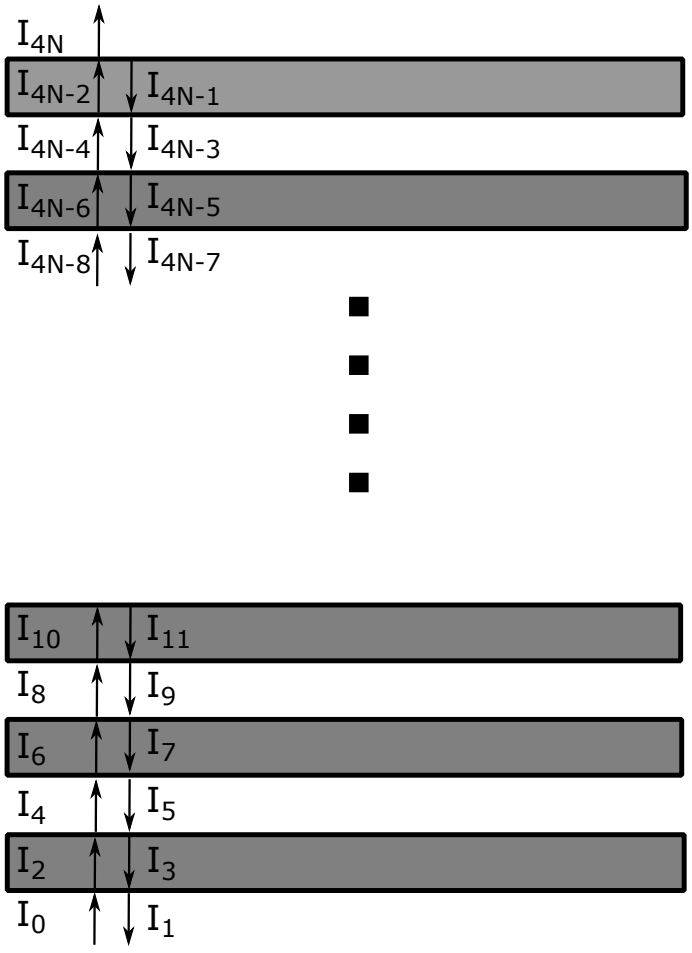

Figure II.2: A model of the total reflection from N-stacked quartz interfaces separated by air gaps

It is straightforward to show that the total reflected light, $R = \frac{I_1}{I_0}$, for N quartz plates is given by

$$R = \frac{I_1}{I_0} = \frac{2N\rho}{1 + (2N - 1)\rho} \tag{II.3}$$

This result was initially derived by Stokes in 1860 [73].

The result is especially interesting when N grows exceptionally large. If we assume a 4% reflection ($\rho = 0.04$), then the reflectivity of the quartz plate stack reaches 0.999 for approximately 12,000 plates. As a result, a highly reflective mirror can be created from a material that transmits most of the light incident on its surface. The neglection of absorption is especially important for this model. If each quartz plate absorbs just a small fraction of light, then light is lost with each pass through the quartz plate. Since a high reflectivity requires many passes through quartz in this model, a small absorption can greatly diminish the total light reflected from the stack. It is also important to note that the model is not unique to quartz. An alternate material can be substituted with the same result provided that the material transmits light without losses from absorption.

In practice, a reflector of 12,000 quartz plates is bulky and impractical for most applications. If each plate was 1 cm thick, the stack would be as tall as 1.3 football fields before even considering the necessary air gaps. However, a micron sized quartz powder (fumed silica) can provide a similar number of interfaces within a much more reasonable thickness. While this model is imperfect for describing the interaction within the powder, it is sufficient from the stand point of quartz/air interfaces for the purposes of this study.

The fumed silica powder is a hydrophilic Aerosil® powder by Evonik-Degussa Industries in Essen, Germany [34]. While many different powder lines have been explored, Aerosil EG50 was deemed most suitable as it produced the highest reflectivity when tested. The number 50 is used to denote the specific surface area of the particles ($50\frac{m^2}{g}$). While

the base particle size is typically between $20 - 40$ nm, the particles form aggregates which then agglomerate to form even larger particles [5]. As a result, the effective particle size can be several microns in size.

Uses for Integrating Cavity Experiments

The powder described above was used to create a highly reflective integrating cavity. In addition to showing that the fumed silica powder was highly reflective, Cone et al. measured the bidirectional reflectance distribution function (BRDF) and showed that the reflection from the surface of the powder was Lambertian as well. This made the powder suitable for a new generation of integrating cavities. The manufacturing procedure for these cavities varied depending on the size and application. For some cavities, the powder was pressed inside a quartz cylinder. These cavities were capable of being baked at high temperatures (1000 °C) since contamination due to out-gassing was eliminated. While the high temperature bake noticeably increased the cavity reflectivity, the physical mechanism for the increase is unclear. Currently, it is believed that the high temperature bake eliminates additional trapped moisture from within the sample. A definitive answer requires further investigation.

Because of the increased reflectivity that the high temperature bake affords, packing powder into a quartz cylinder is the best option for manufacturing an integrating cavity. However, high purity fused silica (solid quartz) pieces are expensive. Furthermore, the cost increases rapidly for larger diameter cylinders. Large cavities (sample volume ≈ 1 L), can cost $10,000 for the glassware alone. Quartz is also extremely fragile which limits its field uses and makes it better suited for laboratory experiments.

Alternatives such as plastic and metal have been used in place of quartz to provide durability and reduce the cost of larger instruments. However, plastics will begin to de-

compose at 140°C and will melt at 160°C. On the other hand, metals have a much higher melting point than plastics ($>$ 1300°C) but will out-gas at high temperatures. Out-gassing can cause optically absorbing contaminants to become absorbed and embedded in the powder cavity wall. Therefore, neither powder packed in metal nor powder packed in plastic can be baked at high temperatures. As a result, two separate packing procedures have been adopted: one where the powder is packed in a quartz cylinder and one where the powder is packed in a non-quartz cylinder. The quartz cylinder packing procedure will be used to manufacture cavities for ICRDS measurements while the non-quartz cylinder procedure will be used to manufacture the ICAM-II.

All-Quartz (Empty) Integrating Cavity

This section discusses the manufacturing of a fumed silica integrating cavity packed in a quartz cylinder. A simple flow chart is shown in Fig. II.3 as an overview and for reference.

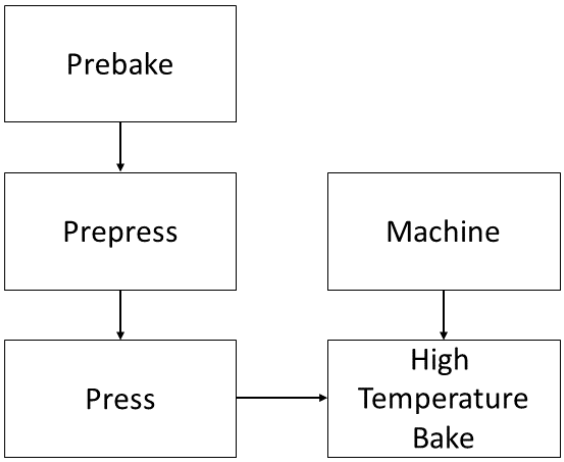

Figure II.3: A flow chart for the manufacturing procedure for a cavity packed in a fused silica cylinder

Powder Preparation for Use in an Integrating Cavity

The powder is shipped from Evonik Degussa in a 15 kg plastic bag. The powder is scooped out of the plastic bag using a 250 mL Pyrex beaker and placed into two 1 L quartz beakers. Latex gloves are used when handling powder to avoid contaminating the powder with oils from the skin. A 3M^{TM} half face piece 7500 series respirator fitted with a model 2091, P100 particulate filter is used to reduce the risk of health complications from inhalation of the powder. Because the powder is hydrophilic and absorbs moisture in the atmosphere, the 1 L quartz beaker is placed in a 1.5 cu. ft Fischer Scientific Isotemp Vacuum Oven that is connected to a liquid nitrogen sorption pump. The vacuum oven can reach a maximum temperature of $\approx 280°C$ at a pressure of ≈ 1 Torr. A bead of vacuum grease is applied along the silicon gasket of the oven door to prevent atmospheric leakage into the oven. The oven door is closed and the stainless steel sorption pump is cooled in a liquid nitrogen bath. The sorption pump is filled with a sieve material. Once the liquid nitrogen bath stops boiling while in contact with the pump, the pump valve is opened to the oven interior. The temperature gradient between the oven and the sorption pump chamber causes the air to flow from the oven to the sorption pump chamber. The air condenses inside the stainless steel pump chamber and the sieve material traps the molecules from returning back to the oven. This creates a vacuum in the oven. Once the oven reaches a resting pressure, the sorption pump valve is closed. The oven temperature is then set to the desired bake temperature. The powder is usually baked to $\approx 250°C$. This temperature is well past the boiling point of water (100°C) and is sufficient to vaporize much of the water in the powder.

After extended use, the effectiveness of the sieve material diminishes due to trapped molecules. When this happens, the oven will not reach its lowest vacuum pressure. The

sieve material can be regenerated by first opening a small vent stopper on the top of the stainless steel canister. A resistive heating sleeve is placed around the outside of the stainless steel container for heating. The material can be quickly regenerated by baking the sleeve for $\approx$ 1-2 hours. For full regeneration, baking for 24 hours is required. After baking for the desired time, the heating sleeve is unplugged and the vent is sealed using the rubber stopper. After baking the sieve material multiple times, the sieve material may lose its overall effectiveness and need to be replaced.

For the best results, the sleeve is baked while the oven reaches its set point temperature. Once the oven reaches its temperature, any moisture that was vaporized by the increase in temperature is eliminated through a second pull of the vacuum. The oven is then purged with $\approx \frac{1}{2}$ atmospheres (atm) of ultra-high purity (UHP) Argon. Argon was chosen because it is an inexpensive, inert noble gas. The oven is turned off and the powder is allowed to cool in an Argon environment. Once the oven reaches room temperature ($\approx$ 6 -12 hours), the oven is completely filled with Argon until the pressure inside the oven is equal to atmospheric pressure. At that point, the oven door can be opened and the powder can be removed for use. This process is referred to as a prebake.

Once the prebake has been completed, the quartz beaker is removed and prepared for the prepress procedure. Prepressing involves using a hydraulic press to pack the powder into a semi-solid disc. First, a large quartz cylinder is placed on a flat circle of aluminum foil. The quartz cylinder is typically 4.50 inches in diameter and 2.5 inches long with a nominal thickness of 0.25 inches. The aluminum foil circle is cut such that the diameter of the circle is approximately 2 inches larger than the outer diameter of the quartz cylinder. Electrical tape is then wrapped around the outside of the quartz cylinder with the adhesive side facing away from the center of the cylinder. After several revolutions of the tape, the tape forms a temporary adhesive coating around the outer surface of the cylinder. The tape is continuously wound around the cylinder until the bottom is reached. The aluminum foil

circle is folded up gently so that a tight, thin layer of aluminum covers the bottom of the cylinder. The folded edges of the aluminum foil are pressed against the tape adhesive so that the foil adheres to the side of the cylinder. The cylinder is placed on top of a one inch thick piece of 1 ft x 2 ft rectangular polycarbonate. The polycarbonate rests on a piece of stainless steel with the same dimensions. The stainless steel and polycarbonate are used as support while the powder is pressed.

A pressing tool was fashioned out of a fused silica disc that was 4.50 inches in diameter. The quartz disc has a nominal thickness of 0.25 inches. This thickness was chosen because it was the thickest standard size commercially available from Technical Glass Products. A 0.75 inch thick piece of brass was epoxied to the top surface of the quartz disc using silicon epoxy. This disk provided support during the pressing process and prevented the press from directly contacting the quartz disc. To ensure that the epoxy formed a strong bond with the brass, the bottom of the brass disc was "faced-off", or smoothed, in the lathe. A gently pressure was applied while the epoxy cured. After 1-2 hours, the brass plate and quartz disk will be lightly bonded. However, a full cure of 24 hours is recommended to ensure that a strong bond is created. A 4 inch long, 2.25 inch inner diameter (ID) piece of PVC was centered on the brass disc and epoxied. The PVC is used as a handle to easily maneuver the piece in and out of the cylinder during the pressing process. Once the epoxy is completely hardened, the piece is prepared for prepressing.

During prepressing, the prebaked powder is slowly scooped into the quartz cylinder. The pressing piece is slid inside of the quartz cylinder and rested on top of the quartz powder. The hydraulic press is lowered inside the PVC handle until it makes contact with the top of the brass surface. Pressure is applied using a 1.50 inch piston until the pressure gauge reads 1000 pounds per square inch (psi). To find the resulting pressure on the powder, we first consider the relation

$$P = \frac{F}{A} \tag{II.4}$$

where P is the pressure, F is the force applied and A is the area to which the force is applied. Note that the gauge pressure denotes the pressure applied by the piston. The force applied from the press is spread over the total area of the quartz disk. Setting the force from the piston equal to the force on the disk, the pressure applied to the powder is determined from

$$P_{powder} = \frac{P_{gauge} \cdot A_{piston}}{A_{pp}} \tag{II.5}$$

where P_{powder} is the pressure on the powder, P_{gauge} is the pressure on the gauge, A_{piston} is the area of the piston head, and A_{pp} is the area of the pressing piece. Assuming that both the piston and the pressing piece are cylindrical, this expression simplifies to

$$P_{powder} = \frac{P_{gauge} \cdot r_{piston}^2}{r_{pp}^2} \tag{II.6}$$

where r_x denotes the radii of the respective cylinders. For a 4.50 diameter pressing piece, the pressure applied to the powder for a gauge reading of 1000 psi is $\approx$ 110 psi. Previous work by Musser demonstrated that optical transmission was minimized for pressures from 30 to 1000 psi. Very high pressures can generate optical contact within the quartz powder and reduce the reflectivity of the material due to a diminished number of air-quartz interfaces.

The prepressing procedure is repeated until the quartz cylinder is roughly 80% filled. A sharp razor blade is used to slice the electrical tape on the outer surface of the cylinder. Pressure is applied to the top of the cylinder so that the tape can be removed from the sides of the cylinder without disrupting the aluminum foil on the bottom. The aluminum foil

is simply removed and discarded. The semi-solid disc formed inside the quartz cylinder is broken into pieces and placed in a beaker for storage. This disc is then masticated and stirred until a coarse powder is created. This process is repeated with a new piece of aluminum foil until all of the prebaked powder has been prepressed.

Prepressing is advantageous in that it minimizes stored static charge from the powder. Static can cause the powder to cling to materials such as aluminum foil resulting in a poor finish to the top surface of the integrating cavities. Furthermore, when the powder was pressed at 100 psi and masticated, the resulting coarse powder consisted of irregularly shaped interlocking agglomerate particles that were formed from the original particles. Since the integrating cavities of the ICAM-II had to be hand-pressed to avoid damaging the fused silica components, the prepacking created tighter interlocking interfaces than is possible by hand-pressing. Therefore, many of the tightly-packed interlocked pieces from the hydraulic press remained which allowed for a higher density of powder.

The importance of the prepack varies depending on the type of cavity being manufactured. If a cavity is being manufactured for ICRDS, the cavity will likely be repressed into a final form. As a result, the importance of maintaining the tightly-locking interfaces is diminished. Here, the prepack is performed to minimize static discharge and maximize reflectivity. If a glass/quartz cell is required in the middle of the cavity, the powder cannot be repacked using the hydraulic press. In this case, the cavity is repacked using hand pressure only to prevent the quartz pieces from breaking. In this case, the prepack is a critical step to maximizing the cavity reflectivity. The high density from the tightly packed pieces give a much denser wall than is achievable by simple hand pressing. A more detailed discussion of the packing procedures for an integrating cavity with a quartz cell will be described in the section on the manufacturing procedures for the ICAM-II in Chapter 4. For now, we will focus on the manufacturing process of an empty fumed silica integrating cavity.

An empty fumed silica integrating cavity typically consisted of two machined fumed silica halves that are stacked on top of one another. The two halves are packed following a similar process to the prepack procedure. However, this time the aluminum foil was carefully placed to avoid any wrinkling or creases. During the final packing process, the top surface finish of the cavity halves is dependent upon the smoothness of the aluminum foil. Furthermore, each quartz cylinder must be completely filled. To help with filling the top portion of the cavity, a small 0.5 inch long, quartz ring with the same diameter and thickness of the quartz cylinder is added to the top of the cylinder. The ring is secured by wrapping the tape (with the adhesive side pointing out again) around both the ring and cylinder. This serves as a temporary extension for the cylinder. The cylinder is packed using the same prepacking procedure. Once the powder is packed tightly to the seam of the cylinder and the extension ring, the ring is removed by slicing the tape with a razor blade. Once the tape is removed, the packed cylinder is flipped (with aluminum foil still intact) so the aluminum foil is facing up. The cylinder is placed on a solid thin quartz disc that has the same diameter as the outer diameter of the cylinder. The aluminum foil is then peeled away from the quartz powder carefully. Because the static build-up was removed during the prepack, the aluminum foil can be removed without destroying the finish from the top of the cavity. The process is repeated for the second cylinder.

The powder is baked at a high temperature for 6-8 hours. Since the cooling process takes 12 hours and the pottery kiln is not vacuum sealed, UHP Argon is slowly released into the kiln to provide an inert environment. Argon was again chosen because of its properties as a noble gas. Once the oven has completely cooled, the fumed silica cylinders can be removed from the oven.

The cylinders are machined, one at a time, with a mill. Typically, a 2.50 inch diameter, 1.25 inch deep cavity is drilled into each half using a 2 flute, 0.75 inch end mill bit. Once the two quartz halves are machined, a cavity can be created by stacking the two halves on

top of one another. A picture of the two quartz halves is shown in Fig. II.4.

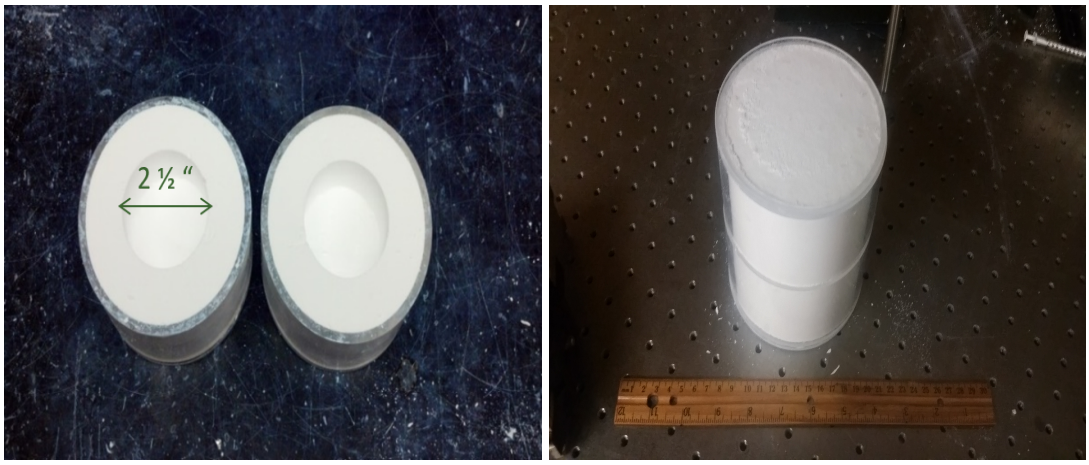

Figure II.4: (Left) A picture of the two machine quartz powder cavity halves. (Right) A picture of the quartz powder cavity halves stacked on top of one another to create a complete integrating cavity.

Cavity with Non-quartz Components

If the container is made from plastic or metal, then the high temperature bake cannot be performed as outlined in the above description. Instead, the pieces from the prepressed powder are loaded into a large quartz beaker and placed into the high temperature kiln. This powder is baked to 1000°C for 6-8 hours and allowed to cool under an Argon environment. Once the powder is cooled, it can be removed. Using a quartz pestle, the pressed quartz pieces is stirred and masticated until a coarse powder consistency is reached. This powder can then be pressed into a vessel made from any material.

Comparison with Spectralon

The diffuse reflecting properties of Spectralon products makes Spectralon suitable for a number of applications in aerospace & defense, image sensors, telecommunications, and lighting. In addition to the many applications of Spectralon, its use as a diffuse reflecting surface for commercial integrating cavities is well established. Spectralon is most effective in the visible with diminishing performance in both the UV and the IR. A summary of the reflectance values for Spectralon is shown in Table II.1.

Table II.1: Reflectance of Spectralon [41]

Wavelength Range (nm)	**Spectral Reflectance**
250	92.5%
300	92.5%
350	$97.5 - 99.5\%$
500-700	$98.5 - 99.5\%$
750-1600	$97.5 - 99.5\%$
1650-2500	92.5%

For wavelengths between 0.7-20 μm, Labsphere provides an alternative product called Infragold. However, even in this range, Spectralon quotes a typical reflectance of $> 94\%$ for wavelengths above 1 μm. Spectralon's diminished performance for ultraviolet wavelengths is especially problematic since no alternative diffuse reflector exists for this range. In addition, Spectralon is susceptible to solarization under long-term exposure of both high and low levels of UV radiation which further decreases its performance. Solarized Spectralon can be rejuvenated by flushing the Spectralon piece with ultrapure water. The Spectralon is then baked at $75^{\circ}C$ for 12 hours at a vacuum less than 1 Torr.

The need for an alternative to Spectralon for ultraviolet measurements lead to the discovery of the fumed silica diffuse reflector. While fumed silica was expected to outperform Spectralon for ultraviolet wavelengths, it exceeded expectations with an improved reflectance in the visible spectrum as well. Table II.2 compares the reflectivities of Spectralon with the reflectivities of fumed silica at two common wavelengths, 266 nm and 532 nm.

Table II.2: Comparison of the Reflectivities of Fumed Silica [17] and Spectralon [41]

	λ=532 nm	λ=266 nm
Fumed Silica	99.92%	99.69%
Spectralon	99.8%	96%

The seemingly slight increase from 99.8% to 99.92% has a significant effect. The reflectivity, ρ, is the fraction of light reflected, but 1-ρ is the measure of light energy lost at each reflection. Since $1 - 0.9985 = .0015$ and $1 - 0.9992 = 0.0008$, the light is lost two times slower for a cavity with a reflectivity of 0.9992 than for a cavity with reflectivity of 0.9985. Hence, for the same cavity, the effective path length in a cavity with $\rho = 0.9992$ would be 2 times greater than in one with $\rho = 0.9985$. If you compare the reflectivity of Spectralon with the reflectivity of fumed silica at a wavelength of 266 nm, the effective path length of a fumed silica cavity is approximately 12 times greater than the effective path length of a Spectralon cavity.

CHAPTER III

INTRODUCTION TO THE INTEGRATING CAVITY ABSORPTION METER AND USES FOR THE MEASUREMENT OF THE OPTICAL ABSORPTION COEFFICIENT OF WATER

Volume light absorption is an inherent optical property of pure water. Together, with scattering and the optical characteristics of other dissolved/suspended materials, it gives large bodies of water their apparent color. For example, the main reason a large body of pure water appears blue/violet is because (i) the absorption of blue light is low and thus, more blue light is available for scattering out of the water [58, 45] and (ii) Rayleigh scattering is much more effective at scattering shorter than longer wavelengths out of the water.

Much as in the terrestrial food web, energy from the sun strongly influences the aquatic food web. Organisms, such as phytoplankton, convert radiation from the sun into energy through photosynthesis [14]. Because of the low optical absorption of water in the blue, the many pigments in phytoplankton (e.g. chlorophyll) evolved so as to strongly absorb blue-green light, leading to an ideal habitat for phytoplankton [15, 81].

While the visible and infrared absorption spectrum of pure liquid water has been relatively well established (> 400 nm) [60, 56, 70, 19], agreement on the absorption spectrum of water in the ultraviolet, as well as in portions of the blue, has yet to be achieved [56, 61, 24]. The ultraviolet spectrum of water is impacted by many factors such as organic content and dissolved oxygen which are independent of the intrinsic optical properties of

Part of the data reported in this chapter is reprinted with permission from "Ultraviolet (250-550 nm) absorption spectrum of pure water" by John D. Mason, Michael T. Cone, and Edward S. Fry, 2016 *Applied Optics*, Vol. 55, Issue 25, pp. 7163-7172.

pure water. The most commonly accepted studies of the UV properties of pure water are from Quickenden and Irvin (1980), Ghormley and Hochanadel (1971) and Kröckel and Schmidt (2014) [61, 28, 40] which focus on the spectral region 180-320 nm. In each of these studies, the attenuation (scattering and absorption) was measured. The absorption was then calculated by subtracting the molecular scattering (Rayleigh scattering) from the measured attenuation. In particular, the studies by Kröckel and Schmidt and by Quickenden and Irvin both used the same differential attenuation experimental design. While the measured attenuation was identical in both studies, the scattering contributions used by Kröckel and Schmidt varied from a factor of 2.2 lower at 190 nm to 2.6 lower at 320 nm than the scattering contributions used by Quickenden and Irvin. Therefore, the resulting absorption coefficients are quite different for the two studies [61, 40].

The above example demonstrates the need for a scattering independent measurement. Since Rayleigh scattering is proportional to λ^{-4}, scattered light rapidly increases for shorter wavelengths. In the marque book by Jonasz and Fournier (2007), *Light Scattering by Particles in Water: Theoretical and Experimental Foundations*, the authors state that "the results are particularly sensitive to [intrinsic scattering corrections]... where the absorption of water is at a minimum". This scattering correction is especially problematic in the UV where scattering grows increasingly large. Jonaz and Fournier continue by stating that "the minimum absorption of water could be considerably smaller [than the literature values at 420 nm], and the level of sensitivity and accuracy required to carry out an accurate absorption experiment...is still daunting today. The most promising approach so far appears to be the integrating cavity absorption meter [(ICAM)] in combination with improved water purification systems" [36]. The present study combines a state-of-the-art water purification system capable of producing semiconductor grade water with the improved sensitivity and scattering independence of a new version of the ICAM. The ICAM instrumentation concept previously used provided reliable water absorption data for visible wavelengths.

The new ICAM was designed to provide a reliable UV absorption spectrum down to 250 nm [25, 56].

In 1992, Fry et al. developed the ICAM to measure the absorption coefficient of weakly absorbing materials independent of scattering [25]. As a result of the multiple passes through the sample due to the diffuse reflections from the walls of the ICAM cavity, the ICAM dramatically increases the optical pathlength through a weakly-absorbing sample. This increased pathlength through the sample significantly improves the measurement. Pope and Fry used an ICAM made from the diffuse reflecting material Spectralon to characterize the absorption structure of water from $380-700$ nm [42, 56]. The visible spectrum of water was independently verified by Sogandares and Fry using photothermal deflection spectroscopy [70]. The data from Pope and Fry showed a minimum absorption of 0.0044 m^{-1} at 418 nm. While the high reflectivity of Spectralon creates a long pathlength in the visible (approximately 10 m), Spectralon's reflectivity diminishes for shorter wavelengths (UV) resulting in a decrease of the instrument sensitivity for these wavelengths [25].

Before discussing the results of the ICAM-II, this chapter will briefly summarize the existing literature on the absorption spectrum of water. A compilation of the water absorption spectrum from previous studies is shown in Fig. III.1. The optical absorption coefficient of water molecules is discussed in terms of four different regions: the Debye Relaxation Region, the molecular vibration region, the transparent region, and the electronic absorption region. The physical mechanism for each absorption region will be described in detail.

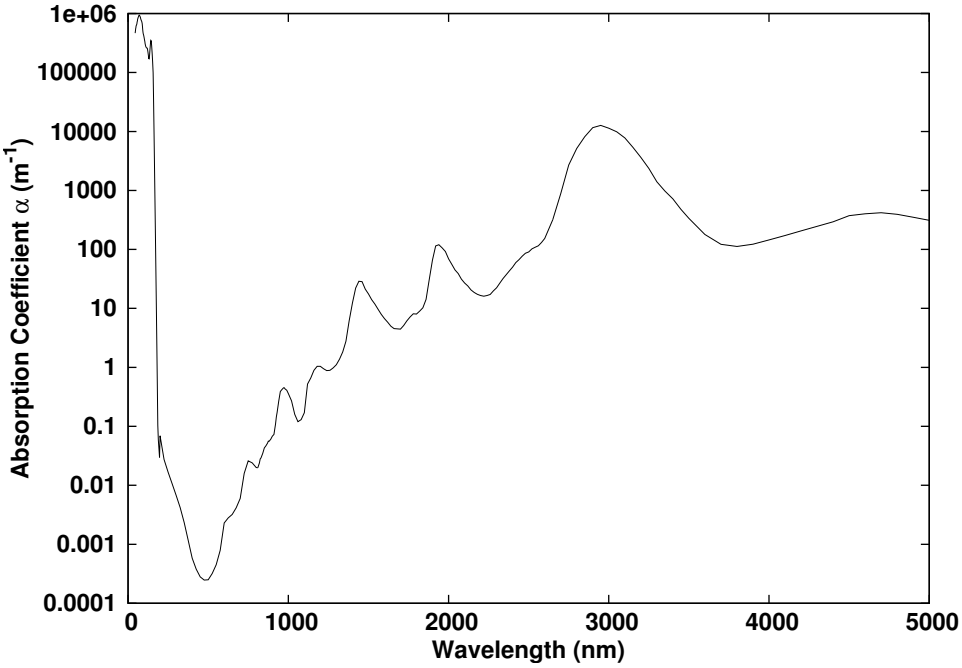

Figure III.1: The literature absorption spectrum of pure water [36]

Basic Principles of Water

Water consists of one oxygen atom and two hydrogen atoms. The two hydrogen atoms are attached at approximately 105° and are separated by a distance of 0.0957 nm. Fig. III.2 shows the Lewis Dot structure of a water molecule. The hydrogen atoms are bonded to the oxygen atom by a single bond. Water, however, is slightly electronegative meaning that the oxygen atom tends to attract electrons towards itself. As a result, the electron shared in the O-H bond spends significantly more time around the oxygen atom than the hydrogen atom. This causes the oxygen atom to be slightly negatively charged (δ^-) while the hydrogen atom has a slightly positive charge (δ^+). The contrasting charges on the oxygen and hydrogen atom make water a polar molecule. Because water is polar, water molecules tend to adhere to one another due to electrostatic forces. This is referred to as van der Waals bonding. To a reasonable approximation, the energy structure of a water

molecule can be described as a dimer molecule pair.

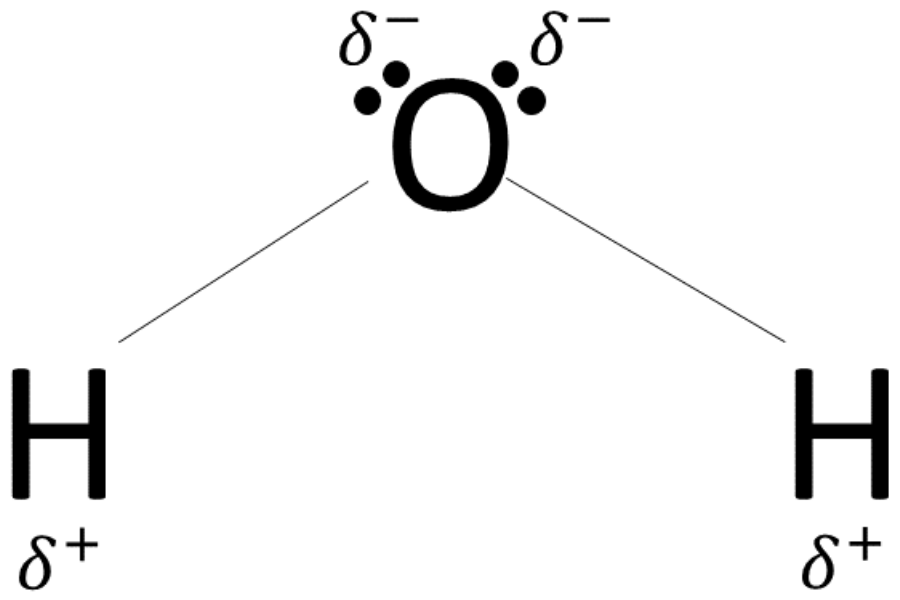

Figure III.2: A Lewis Dot Structure of a water molecule

The potential of a water molecule is represented by a standard coulomb potential with a repulsive core and an attractive outer region. This potential is modeled by a Lennard-Jones 6-12 potential where the repulsive core is modeled by an inverse 12 power potential and the attractive regions are modeled by an inverse 6 power potential. This potential is given by

$$V_d = 4 * \epsilon[(\frac{\chi}{r})^{12} - (\frac{\chi}{r})^6)] \tag{III.1}$$

where $\chi = 0.31655$ nm and $\epsilon = 543.5$ cm^{-1}. The Lennard-Jones 6-12 potential is plotted in Fig. III.3. This potential also accounts for the effect of Van der Waals forces [36].

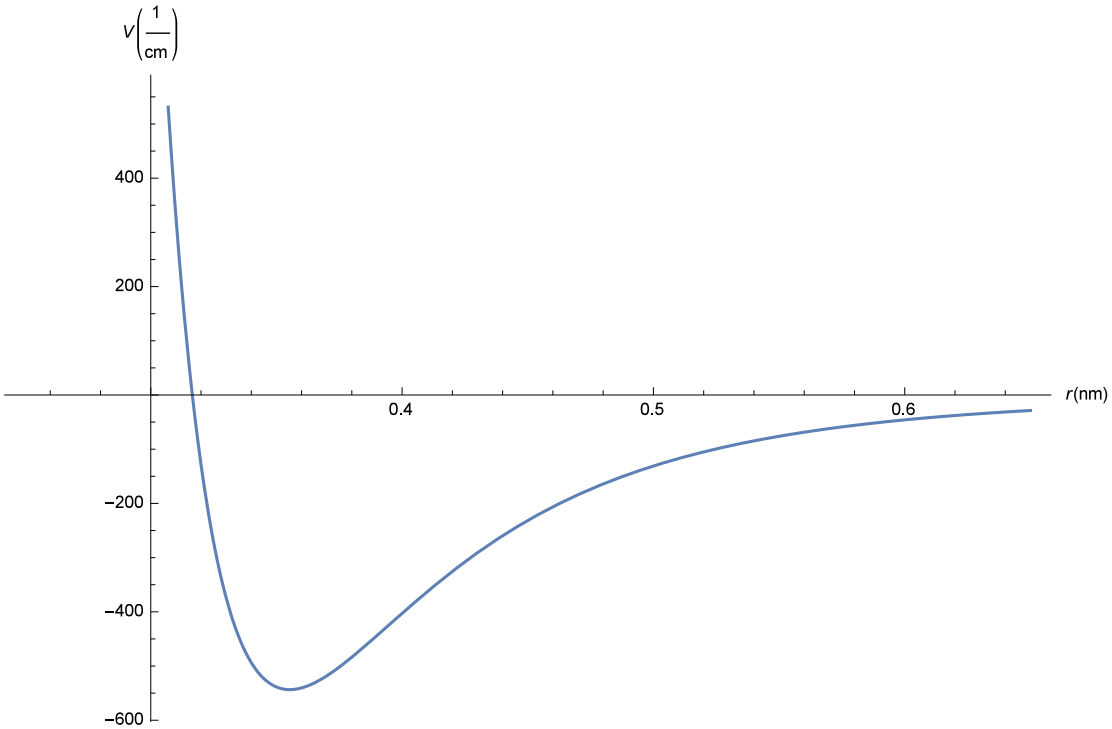

Figure III.3: The Lennard-Jones 6-12 potential for a pair of water molecules

The Debye Relaxation Region

Debye relaxation occurs when molecules with a permanent electric dipole partially align along an alternating electric field. The molecular alignment polarizes the sample. At the same time, the rotation of the molecules counteracts the alignment to the electric field and returns the molecules to a random orientation. The molecular rotation acts as a damping force to the sample polarization. Since water is a nonlinear molecule with the hydrogen atoms grouped to one side of the oxygen molecule, the electron density is larger around the oxygen atom than the hydrogen atoms. The unbalanced electron distribution gives rise to a permanent dipole moment of the molecule. The Debye Relaxation phenomena plays a significant effect in the determination of the optical constants of water, specifically for long wavelengths (microwaves) [2].

The Molecular Vibration Region

The molecular vibration region is largely categorized by the absorption of infrared wavelengths but overtones from vibrational-rotational transitions can be seen at shorter wavelengths in the visible as well. This region is broken down into two sub-regimes: the molecular band region ($1 - 10\mu$m) and the intermolecular band region ($10 - 100\mu$m). The infrared spectrum of water is governed by nine degrees of freedom of the triatomic water molecule. The three translation degrees and three rotation degrees have little impact on the absorption coefficient of pure water. However, the three vibrational degrees of freedom are significant when considering the infrared absorption spectrum of water. The three vibrational modes of a water molecule are shown in Fig. III.4. The mode denoted by ν_1 signifies the symmetric stretch. This motion occurs when the two hydrogen atoms move towards (away from) the oxygen atom as the oxygen atom moves towards (away from) the center of mass of the two hydrogen atoms. The fundamental frequency of ν_1 occurs at 3657 cm^{-1} (2.75 μm). Similarly, ν_3 signifies the asymmetric stretch mode of water. The ν_3 mode consists of the two hydrogen atoms oscillating out of phase with one another (one hydrogen atom moves towards the oxygen atom while the other moves away). The oxygen atom moves along the x-axis towards the closest hydrogen atom. The fundamental frequency for ν_3 is found at 3756 cm^{-1} (2.66 μm). The final resonance mode is the molecular bend denoted by ν_2. For ν_1 and ν_3, the bond angle remains fixed at 105°. During the ν_2 vibration, the hydrogen atoms move towards and away from the oxygen atom while the oxygen atom moves towards and away from the center of mass of the two hydrogen atoms. The fundamental frequency of ν_2 is found at 1645 cm^{-1} (6.27 μm) [9].

Notice that the fundamental frequencies of the anti-symmetric and symmetric modes are slightly offset from one another. Kjaergaard et al. showed that the frequency of the asymmetric stretch mode is a factor of 10 larger than that of the symmetric mode [38]. This

relationship holds true for equivalent overtones of each mode. However, by the third overtone, the asymmetric and symmetric stretch are indistinguishable in most spectroscopic surveys. For this reason, most discussions surrounding the vibrational motion of water group the symmetric and asymmetric stretch modes into a single O-H stretch mode.

The scissor mode is roughly an order of magnitude less than the O-H stretch mode. A combination of the fundamental scissor mode and the O-H stretch mode is easily observable since it occurs between the overtones of the O-H stretch. These features are considerably smaller than pure stretch modes but can be characterized with relative ease.

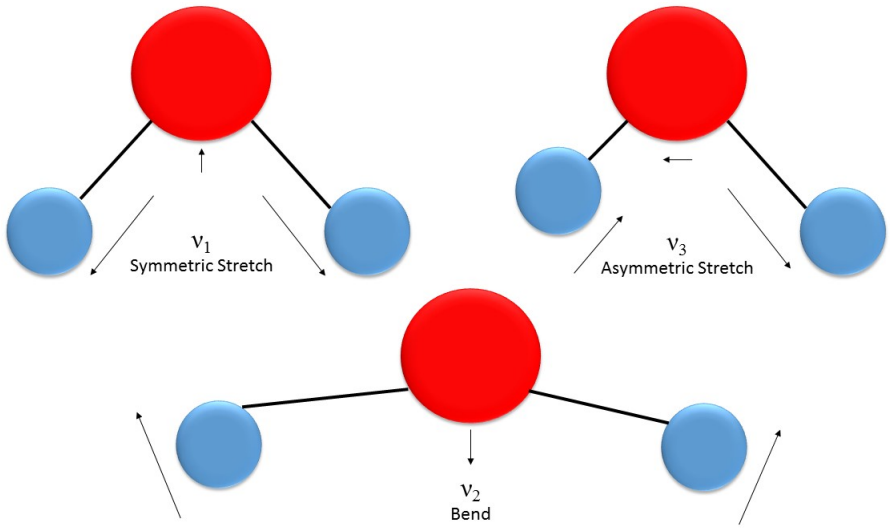

Figure III.4: Vibrational modes of a water molecule

Overtones from the O-H stretch bond (combination of symmetric and asymmetric) contribute various peaks throughout the spectrum. Tam and Patel demonstrated that the location of the n^{th} harmonic stretch can be found from [55]

$$\nu_n = n(3620 - 63n)\text{cm}^{-1}. \tag{III.2}$$

By extension, the combination modes are found by

$$(\nu_n + \nu_{scissor}) = n(3620 - 63n) + 1645\text{cm}^{-1}. \tag{III.3}$$

While combination modes with higher harmonics of the ν_2 scissor mode can exist, they are indistinguishably small for most studies. As a result, only the fundamental scissor mode is considered. The wavelengths of the 10 harmonics of the O-H stretch (and the combined scissor fundamental are shown in Table III.1.

Table III.1: The Wavelengths of the Vibrational Modes of a Water Molecule

Vibrational Mode (ν_1/ν_3)	Theoretical Wavelength (λ(nm))
(0,1)	6079
(1,0)	2811
(5,0)	605
(5,1)	550
(6,0)	514
(6,1)	474
(7,0)	449
(7,1)	418
(8,0)	401
(8,1)	376
(9,0)	364
(9,1)	343
(10,0)	334
(10,1)	317

The infrared absorption spectrum of water was first measured by Kou et. al. from 0.65 μm to 2.5 μm [39]. Kou et. al. used a differential attenuation technique with sample cells ranging from 100 μm to 20 cm. The sample cells were inserted into a Fourier-transform

spectrometer (resolution 16 cm^{-1}) and the attenuation was measured. Since the intrinsic scattering in this region is small compared to the absorption (recall that Rayleigh scattering diminishes with $1/\lambda^4$), the attenuation can be assumed to be caused entirely by absorption within negligible error.

The Transparent Region

The transparent region refers to part of the spectrum where the absorption coefficient is at a minimum. In this region, light seems to pass through water unperturbed. The absorption in the transparent region is several orders of magnitude smaller than absorption in other parts of the spectrum. The transparent region begins in the near ultraviolet and extends into the red. Absorption in this region is characterized by the tails of the molecular vibration region and the tail of the electronic transition absorption regions. The absolute minimum of the absorption of pure water is found at the transition from one absorption phenomena to the either (i.e. the point where the electronic transition tail meets the tail from the molecular vibration spectrum). The structure of the absorption spectrum for long wavelengths in this region is characterized by high overtones of the vibrational motion of water molecules. Conversely, the structure of the short wavelength end of this region is characterized by the featureless exponential decay of the first electronic molecular transition.

This region is particularly important for large samples of water. The effect is most prominently seen in the differential absorption. We consider a uniform white light illumination on a 5 m sample of pure liquid water. If we neglect effects from scattering, then approximately 83 % of the blue light will be transmitted while roughly 33 % of red light is transmitted. This results in the light transmitted through the water as having a blue tint. This absorption is especially significant for the characterization of ocean waters.

As mentioned in the introduction to this chapter, the visible spectrum of the transparent region was measured using the original ICAM developed by Pope and Fry in 1997 [56]. Pope and Fry realized that the approximation used by Kou et. al. (that intrinsic scattering is small compared to the absorption) no longer holds for the transparent region. In addition to the diminished absorption, Rayleigh scattering increases by λ^{-4} for shorter wavelengths. As a result, measurements in the transparent region are particularly sensitive to intrinsic scattering corrections. The ICAM provides an elegant solution to this problem as it provides a measurement with no required scattering correction. However, the diminished performance of Spectralon in the blue and UV limited the study. Since no scattering independent alternative exists to measure the absorption in the blue/UV region, a large discrepancy exists between the data sets that currently characterize this region.

The Electronic Absorption Region

Electronic transitions of H_2O molecules occur at ultraviolet wavelengths. The most prominent absorption peaks are found at 151.2 nm, 126.5 nm, and 91.8 nm [36]. The tail from the electronic absorption spectrum has a significant bearing on the global minimum of water absorption and is the source of much of the debate of the absorption spectrum of pure water. The predominant focus of this study centers around the first electronic transition (151.2 nm) so discussion will be limited to this region.

The first electronic transition involves the excitation of an electron from the ground state (X^1A_1) to the first excited state ($^1B_1$). For any electronic molecular transition, the rearrangement of electrons effectively occurs instantaneously. As a result, the atomic nuclei are fixed relative to one another. This greatly impacts the absorption spectrum of a molecule as intermolecular separation impacts the excitation energy. This is referred to as the Franck-Condon principle. The energy of the X^1A_1 state is given via the Lennard-

Jones 6-12 potential, Fig III.3. The upper state, $^1B_1$, is an unstable state that immediately dissociates.

The most commonly accepted study between 195 nm and 320 nm was performed by Quickenden and Irvin in 1980 [62]. Much like the Kou et. al. study, Quickenden and Irvin used a differential attenuation method. Unlike, the Kou et. al. study, however, Quickenden and Irvin attempted to correct for the intrinsic scattering by subtracting the Rayleigh scattering contribution from the attenuation coefficient.

The ICAM-II resolves the UV absorption structure from the tail of the electronic absorption spectrum. The next chapter will discuss the ICAM-II in detail.

CHAPTER IV

ICAM-II EXPERIMENTAL DESIGN

General Overview

The ICAM-II was used to resolve the absorption spectrum from 250-550 nm. A generic ICAM consists of two concentric diffuse reflecting integrating cavities. An overview of the ICAM-II experimental design is shown in Fig. IV.1.

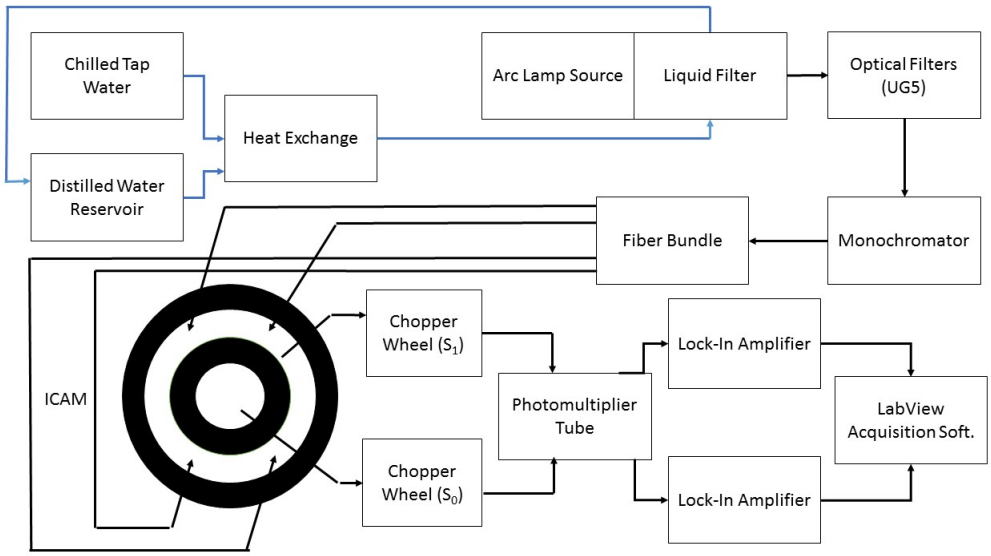

Figure IV.1: A generalized flow-chart of the ICAM experimental setup

Part of the data reported in this chapter is reprinted with permission from "Ultraviolet (250-550 nm) absorption spectrum of pure water" by John D. Mason, Michael T. Cone, and Edward S. Fry, 2016 *Applied Optics*, Vol. 55, Issue 25, pp. 7163-7172. © 2016 Optical Society of America

Theoretical Background

The theory behind the integrating cavity absorption meter has been studied extensively [25]. We will review the rigorous theoretical background behind the integrating cavity absorption meter. Consider the scalar $L(\mathbf{r}, \hat{\mathbf{\Omega}})$ which represents the radiance in the direction of the unit vector $\hat{\Omega}$ in the radial direction $\mathbf{r}$. The vector irradiance, $\mathbf{F}$, is defined as

$$\mathbf{F} = \int_{\mathbf{\Omega}} \mathbf{L}(\mathbf{r}, \hat{\mathbf{\Omega}}) \hat{\mathbf{\Omega}} \mathrm{d}\mathbf{\Omega} \tag{IV.1}$$

Furthermore, the radiant energy density, U, is defined as:

$$U = \frac{n}{c} \int_{\Omega} L \mathrm{d}\Omega \tag{IV.2}$$

where Ω represents the solid angle, c is the speed of light in a vacuum and n is the index of refraction for a homogeneous sample. Using the radiative transfer equation [12], it can be shown that

$$-\nabla \cdot F = \frac{\alpha c}{n} U = \alpha \int_{\Omega} L \mathrm{d}\Omega \tag{IV.3}$$

where α is the absorption coefficient. This relation is assumed valid at every point within the medium, regardless of any scattering effects. By integrating over the whole volume of the sample, V, it follows from the divergence theorem that

$$\int_{V} \nabla \cdot F \mathrm{d}V = \int_{S} (\mathbf{F} \cdot \hat{\mathbf{n}}) \mathrm{d}\mathbf{S} = \frac{\alpha \mathbf{c}}{\mathbf{n}} \int_{\mathbf{V}} \mathbf{U} \mathrm{d}\mathbf{V} \tag{IV.4}$$

Since the integral over the volume for the vector irradiance is the total irradiance and hence the net radiant power, we can express the power P that is absorbed as

$$P = \frac{\alpha c}{n} \int_V U \mathrm{d}V. \tag{IV.5}$$

If we assume that the energy density U is homogeneous (a reasonable assumption for an integrating cavity) then the result in Eq. IV.5 becomes

$$P = \frac{\alpha c}{n} UV$$

[21].

(IV.6)

We next consider the normal component of the irradiance $\mathbf{F}$ at the inside surface of a sample. This is just the outwardly directed irradiance of the sample, namely, F_0 which is defined as

$$\hat{F} = \hat{\mathbf{n}} \cdot \int_\Omega L(\mathbf{r}, \hat{\Omega}) \hat{\Omega} \mathrm{d}\Omega \tag{IV.7}$$

which for an isotropic, homogeneous sample, simplifies to

$$F_0 = \pi L \tag{IV.8}$$

since L is constant. Furthermore, the energy density given in Eq. IV.2 reduces to

$$U = \frac{4\pi n}{c} L \tag{IV.9}$$

where we can then combine Eq. IV.8 and IV.9 to find the energy density U in terms of the outward irradiance F_0 as

$$U = \frac{4n}{c} F_0. \tag{IV.10}$$

Combining this result with result of Eq. IV.6, the total power, P is expressed as the outward irradiance, F_0 as

$$P = 4\alpha F_0. \tag{IV.11}$$

Using conservation of energy, we know that in the presence of an absorber, the power entering a sample must be equal to the power leaving the sample plus the power absorbed by the sample:

$$P_{in} = P_{out} + P_{abs} \tag{IV.12}$$

We define F_1 as the irradiance on the outer cavity wall and F_0 as the irradiance on the inner cavity wall. The power of light entering the cavity is proportional to the irradiance measured in the outer cavity while the power of light leaving the cavity through the diffuse reflecting walls and ports is proportional to F_0. We can rewrite Eq. IV.12 as

$$K_1 F_1 = K_0 F_0 + 4\alpha V F_0. \tag{IV.13}$$

F_1 and F_0 are sampled using the two quartz rods from the inner and outer cavity. Since F_1 and F_0 are proportional to the signal measured by the quartz rods, we conclude that

$$C_1 S_1 = C_0 S_0 + 4\alpha V S_0 \tag{IV.14}$$

or

$$C_1 S_1 = (C_0 + 4\alpha V) S_0 \tag{IV.15}$$

The above equation can be simplified into a ratio of the signals of the inner and outer

cavity such that

$$\frac{S_1}{S_0} = \frac{C_0}{C_1} + \frac{4\alpha V}{C_1} \tag{IV.16}$$

Defining $S = \frac{S_1}{S_0}$ and $C_0' = \frac{C_0}{C_1}$,

$$S = C_0' + \frac{4\alpha V}{C_1} \tag{IV.17}$$

By taking the partial derivative of Eq. IV.17 with respect to volume at a constant absorption,

$$\left(\frac{\partial S}{\partial V}\right)_\alpha = \frac{4}{C_1}\alpha \tag{IV.18}$$

Similarly, rearranging Eq. IV.17 in terms of alpha yields

$$\alpha = \frac{C_1 S}{4V} - \frac{C_1 C_0'}{4V}. \tag{IV.19}$$

The partial derivative of Eq. IV.19 can be taken with respect to the signal to yield

$$\left(\frac{\partial \alpha}{\partial S}\right)_V = \frac{C_1}{4V}. \tag{IV.20}$$

Solving Eq. IV.20 for C_1,

$$C_1 = 4V\left(\frac{\partial \alpha}{\partial S}\right)_V. \tag{IV.21}$$

Combining Eq. IV.18 with Eq. IV.21,

$$\left(\frac{\partial S}{\partial V}\right)_\alpha = \left(V\frac{\partial \alpha}{\partial V}\right)_V^{-1}\alpha \tag{IV.22}$$

Solving for α,

$$\alpha = \left(\frac{\partial S}{\partial V}\right)_{\alpha} \left(V \frac{\partial \alpha}{\partial S}\right)_{V} \tag{IV.23}$$

where V is the total volume of the ICAM-II. Eq. IV.23 will be used to measure the absorption coefficient of pure water.

Instrumentation

Arc Lamp

To provide broadband illumination, a 150-W ozone free xenon arc lamp was used. The arc lamp consists of a Oriel Model 66005 housing using an Oriel 6255 xenon bulb [63, 64]. The bulb is powered using an Oriel Model 68700 Power Supply with power capabilities up to 100 W [67]. A voltage of 85 V (8.5 A) was applied to the bulb. The emission spectrum from the arc lamp is shown in Fig. IV.2. A 3 inch steel Oriel Model 6214 liquid filter (filled with water) was attached to the output of the arc lamp housing to remove infrared radiation from the source [66]. The liquid filter water was cooled using a Neslab water-cooled heat exchanger to remove effects from temperature fluctuation in the filter. A three inch fused silica focusing lens was used to focus the remaining light on to the aperture of the monochromator.

Light Shielding

A 68.58 cm x 60.96 cm x 38.10 cm box was constructed to enclose the arc lamp-monochromator system. The box serves to eliminate ambient light from entering the monochromator as well as to block stray light from the arc lamp that does not enter the monochromator from entering the ICAM-II. The box consists of three walls of 2.22 cm

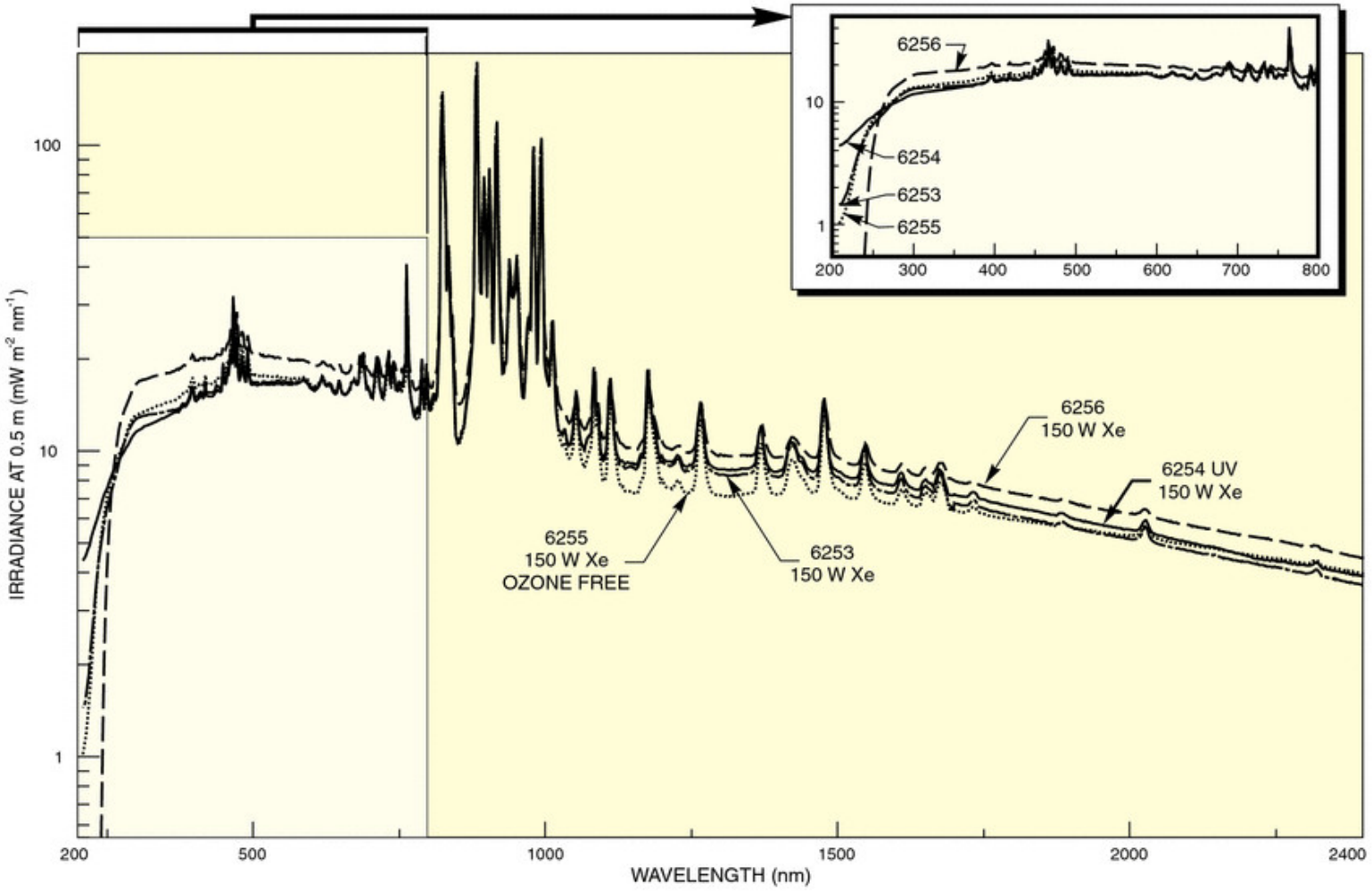

Figure IV.2: The output of a Model 6255 150 W ozone-free xenon arc lamp light bulb.

thick plywood. The front face of the monochromator serves as the fourth wall with the monochromator facing into the box. The wood face opposite of the monochromator front face contains an inverted arch with a diameter of 88.9 mm. The output lens assembly of the arc lamp is placed into the box through the arch and facing towards the monochromator. This ensures that no light is emitted outside of the enclosure. A fourth flat sheet of plywood with the same dimensions of the box is placed on top of the box. The inside of the box is painted black to absorb stray radiation.

Shutter

A 45 mm diameter COPAL DC495 plunger shutter was mounted to the aperture of the monochromator. The shutter was powered by connecting a 2 volt Hewlett-Packard Model 6214A power supply to a solid state relay. The relay was connected to a table top 24 volt AC adapter which in turn powered the shutter. The shutter can be closed to block all light (source and ambient) from entering the monochromator. By closing the shutter, effects from the PMT dark current and ambient light were characterized. The shutter defaults to the off position when voltage is removed.

Monochromator

Final wavelength selection was achieved using a CVI Digikrom 240 monochromator. The Digikrom 240 is a Czerny-Turner scanning monochromator with a focal length of 240mm [65]. The effective aperture ratio is f/3.9. The focusing lens was chosen such that it matches the aperture ratio. The monochromator was fitted with UV-grade fused silica optics and contained a reversible two-grating mount. The gratings had peak transmissions of 500 nm and 330 nm. The reciprocal linear dispersion was 3.2 nm/mm with a 1200 grooves/mm grating. As a result, the spectral resolution was 0.06 nm with 20 micron

wide slits. Tuning of the monochromator was controlled by a computer through a GPIB interface.

Fiber Bundle

A custom fiber array of eight 600 μm silica-core, silica-clad optical fibers are arranged linearly in front of the exit of the monochromator to collect light and deliver it to the ICAM. The linear arrangement is embedded in an aluminum block with a hollow slit milled down the side of the block. The fibers were laid flat in the groove such that the cladding of each fiber laid directly on the aluminum. The clamp piece was screwed on top of the aluminum to hold the fibers in place. The exposed end of the fibers protruded past the end of the aluminum block to collect light from the monochromator. The fibers are aligned on top of one another such that the fiber array is parallel to the monochromator slit. These fiber ends are wrapped with electrical tape to provide additional support.

ICAM Apparatus

The ICAM-II design consists of two concentric fumed silica integrating cavities centered around a 1.538 L quartz glass sample cell. Light is injected into the outer cavity and diffuses through the inner cavity wall to the sample region. The quartz cell has an inlet and outlet port located at the top and bottom of the assembly. Cross sections of the ICAM-II are shown in Figs. IV.3 and IV.4.

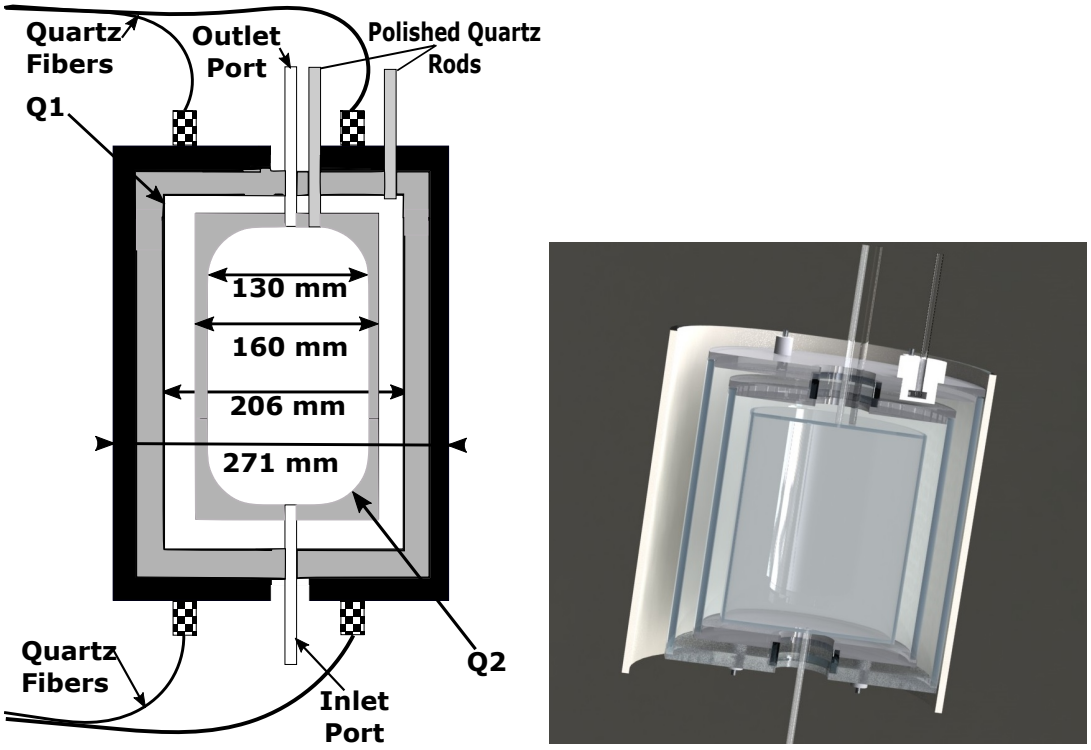

Figure IV.3: (Left) A three dimensional schematic of the vertical cross section of the ICAM-II (Right) A two dimensional drawing of the vertical cross section of the ICAM-II

The outer integrating cavity was constructed by placing a 20.1 cm diameter fused silica tube, Q1, (h = 26.0 cm) centered inside a piece of 25.4 cm diameter Schedule 40 PVC Pipe (h = 33 cm). A special jig was used to ensure that Q1 is centered (x,y, and z) inside the PVC. The area between the PVC and Q1 was packed rigorously with the previously prepared powder (see Chapter 3) using several hand tools. The reflectivity of the outer cavity wall is important as it prevents a loss of light from the instrument by diffusion through the wall. A second fused silica cylinder, Q2, with diameter 17.6 cm (h = 15.85 cm) was centered inside of Q1. The region between Q1 and Q2 was left empty to serve as a reference cavity and optical injection site. A 1.538 L cylindrical quartz sample cell with two quartz stems was centered inside of Q2. The area between Q2 and the quartz

sample cell was lightly filled with the fumed silica powder to form the outer wall of the inner cavity and the inner wall of the outer cavity. If this region is packed too tightly, the reflectivity of the wall would be too high for a measurable amount of light to diffuse through the cavity wall into the sample region.

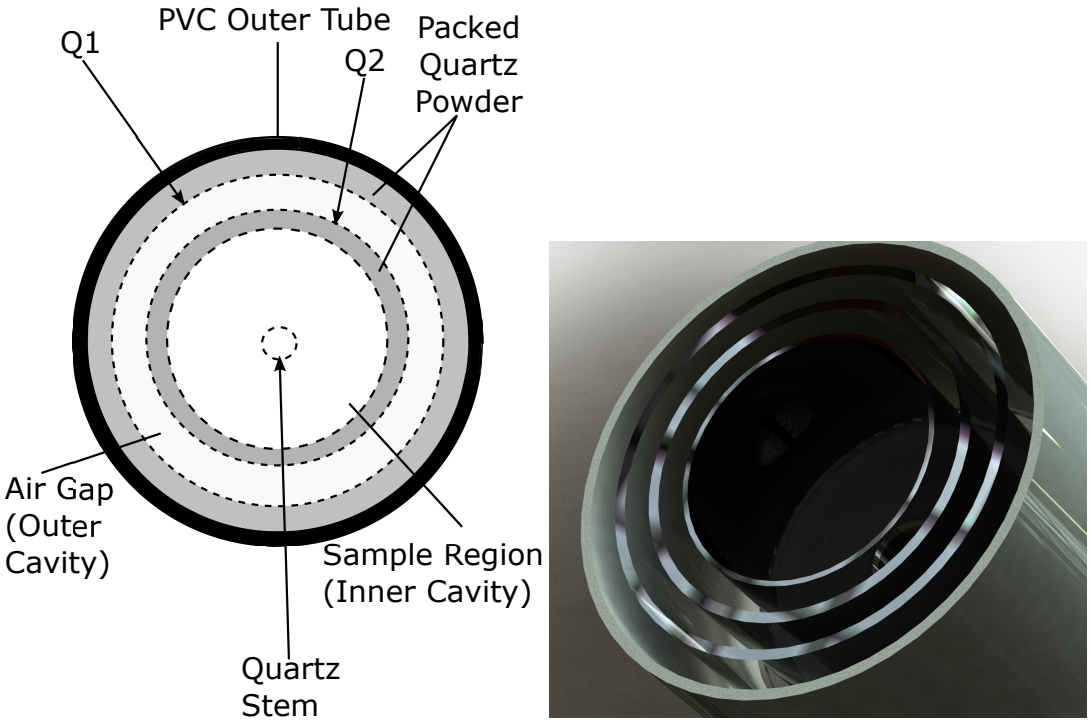

Figure IV.4: (Left) A three dimensional schematic of the horizontal cross section of the ICAM-II (Right) A two dimensional drawing of the horizontal cross section of the ICAM-II

An alternate solution involves reducing the thickness of the inner cavity wall. The sample region surrounded by quartz powder comprises the inner cavity. Light exiting the monochromator was injected into the reference (outer) cavity through the eight quartz fibers. Eight small sections of hypodermic tubing encased in Spectralon are used to pass the quartz fibers through the top and bottom of the outer cavity wall and into the reference

cavity. Four of the quartz fibers are equally spaced at 90° intervals around the top cap and four around the bottom cap. The choice of eight fibers is arbitrary to provide sufficient illumination to the entire outer cavity. However, the diffuse reflectivity of the quartz powder is so high, that a uniform illumination should be achievable with any number of fibers. The irradiances from the inner cavity wall (S_0) and from the outer cavity wall (S_1) were sampled through two optically-polished 6mm and 5mm diameter quartz rods. A larger quartz rod was chosen for the inner cavity to increase the signal from the weaker intensity light.

Light Chopper

In order to distinguish the inner cavity signal from the outer cavity signal, a set of chopper wheels were used to modulate the signal at a specified frequency. Light from each quartz rod is passed through one of the two chopper blades. A Signal Recovery model 651-1 Light Chopper with range from 100 Hz to 3200 Hz in its outer sector and 10 Hz to 320 Hz in its inner sector was used to modulate the signal from the inner cavity. The Light Chopper was controlled by a model 650 Light Chopper Controller. The chopper frequency was set to 1.552 kHz. The outer cavity was modulated using a Signal Recovery model 197 Precision Light Chopper with a total frequency range from 15 Hz to 3000 Hz. The model 197 is controlled internally and is set to 1.207 kHz. The frequencies were chosen to ensure that integer multiples were avoided.

Photomultiplier Tube Assembly

The detection photomultiplier tube (PMT) is a 51 mm diameter, end window 9813QA photomultiplier with a blue-green sensitive bi-alkali photocathode. The Q designation denotes a fused silica detection window as opposed to borosilicate glass window. As a result,

the PMT spectral range is extended into the ultraviolet from 290 nm to 160 nm. The PMT is suited for low light level detection and maintains a high gain, a good signal enhancement ratio, and a high pulsed linearity. The PMT is surrounded by an anodized aluminum metallic shielding which is connected to the ground of the PMT voltage divider. Both the inner cavity and outer cavity modulated signals , S_0 and S_1, are detected simultaneously by this single photomultiplier tube.

A custom PMT mount was built to assist in the collection of optical radiation by the PMT. The housing is constructed from two connected aluminum cylinders of different sizes. The smaller tube is threaded at the end and the PMT voltage divider is mounted at that end. This smaller tube is approximately the same length as the PMT so that the PMT window is exposed at the open end of the tube. The larger cylinder is attached to this open end. This larger cylinder serves as the outer shell of an integrating cavity. A fumed silica integrating cavity is molded inside the cylinder such that the window to the PMT is open to the integrating cavity. Two other input holes (5 mm and 6 mm) are made in the integrating cavity to receive signals from both the inner and outer cavities of the ICAM. Two aluminum ferrule tubes are fed through the holes such that two inches of tubing stick out below the large aluminum cylinder. Two quartz rods are optically polished using Krell Technology optical polishing pads. These rods are slid into the aluminum ferrule tubing such that the polished rod ends are flush with the end of the tubing. The rods are secured by draping two pieces of one μm diameter tungsten wire across the end of the aluminum tubing in the shape of an X. The wire is secured to the sides of the aluminum tubing using quick cure 5 minute epoxy from Gorilla glue. A schematic of the detection scheme is shown in Fig. IV.5 where CW represents the chopper wheels, QR represents the quartz rods, FS IC is the fumed silica integrating cavity, S_1 is the outer cavity signal and S_0 is the inner cavity signal.

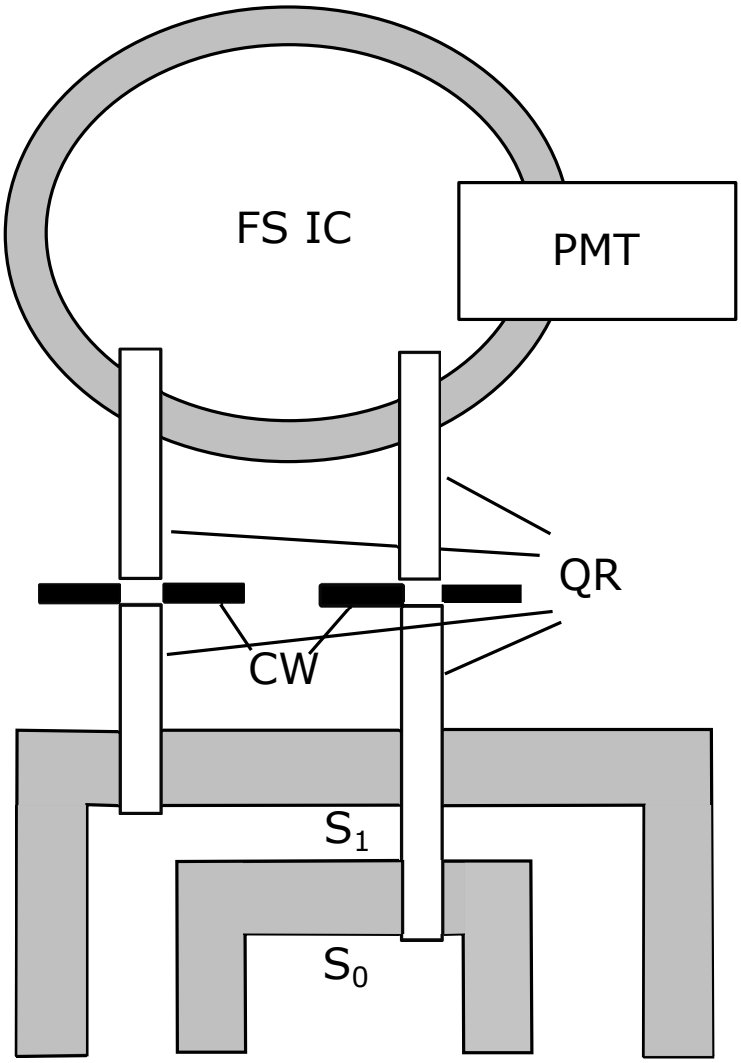

Figure IV.5: The ICAM-II detection scheme

The PMT is powered using a Stanford Research Systems Model PS325 2500V-25 W high voltage power supply. The voltage output is stable to better than 0.002% of full scale with a set accuracy of $0.01\% - 0.05\%$ of full scale. The high voltage power supply has a variable output from $25 - 2500$ volts. For this experiment, the PMT high voltage was selected between the ranges of $1100 - 1400$ volts. The large variability of voltages is due both to variations in the arc lamp output and to the ICAM sensitivity over the measured

wavelength range. A 20 MΩ resistor is added to the output of the PMT for impedance matching.

Lock-In Amplifier

Two Stanford Research Systems Model SR830 DSP Lock-In Amplifiers (LIA) were used to acquire the modulated signals from the inner and outer cavity. The signal from the PMT and a reference signal from each chopper were fed into both LIAs. The Lock-In Amplifiers were set with a time constant of 100 ms and a sensitivity of 500 mV. The dynamic reserve was optimized for low noise. The LIAs were simultaneously phase-locked using an automatic phase-lock loop. This was done to ensure that the time constants are synchronized.

LabView Acquisition Program

Data acquisition was automated using a combination of several connected National Instruments LabView Visual Interface (VI) programs. The monochromator slit width, grating, and wavelength selection are controlled using three separate VIs. A fourth VI was used to acquire signal from the two LIAs. The signal from each LIA was averaged over a specified number of measurements. A ratio of the average signal from each LIA was taken to comprise the final ICAM-II signal. A final VI was used to take make measurements over a desired wavelength range at a desired interval. This VI takes a measurement at each wavelength, starting with the shortest, while tuning the monochromator to the specified values. The wavelength is tuned according to a specified step size.

Manufacturing of the Fumed Silica ICAM

The ICAM-II is carefully packed to ensure that symmetry is maintained about the x,y, and z planes. To assist with positioning during packing, a polytetrafluoroethylene (PTFE

or Teflon) base piece was created. A rendering of the base piece is shown in Fig. IV.6. The piece is designed to elevate each component to the appropriate position.

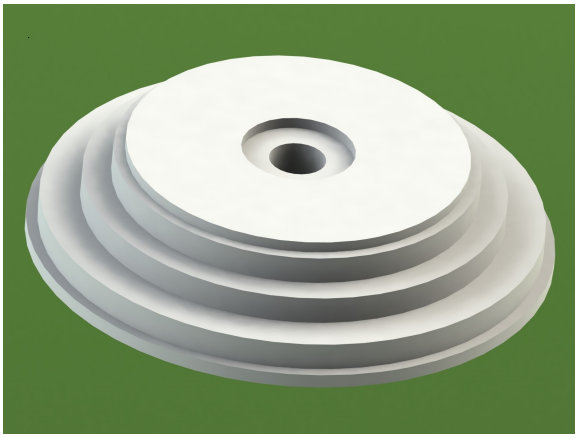

Figure IV.6: The base piece used in the manufacturing process of the ICAM

A clear plastic ring was placed in the center of the base piece. This piece is designed to support the sample cell during packing. If the sample cell becomes tilted, the wall thickness will be non-uniform which can result in inconsistent illumination of the inner cavity. A glass ring was placed around the plug to provide additional support for the inner cell. This prevented the inlet and outlet stems from breaking.

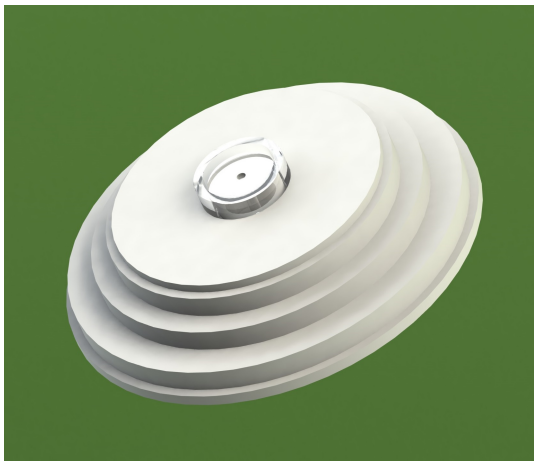

Figure IV.7: The configuration of the polyethylene plug that supports the stem of the ICAM during the packing procedure

The quartz sample cell was placed into the small hole drilled through the center of the plastic plug. The tapered end of the quartz sample cell rested on top of the plastic plug. The bottom surface of the sample cell rested on the small quartz cylinder. This configuration is shown in Figs. IV.7 and IV.8.

Figure IV.8: Schematic of the alignment configuration used to hold the sample cell during packing

A quartz cylinder (Q1) was placed around the top step of the jig and rests on the top of the second step. The region between the quartz sample cell and Q1 is packed lightly with powder. As mentioned in the previous section, the quartz powder was packed lightly to ensure that enough light diffused through the inner cavity wall to fully illuminate the sample region. A 5 mm space was left between the top of the powder and the top of Q1. A quartz disk with a 7.5 cm hole in the middle was placed on top of Q1 to seal the inner cavity wall. The center hole allows the sample cell stem to protrude through the bottom of the ICAM-II. A schematic of the packing procedure for the inner cavity is shown in Fig. IV.9.

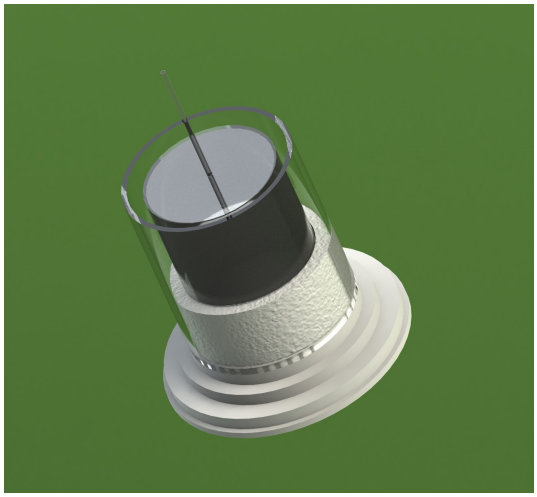

Figure IV.9: Schematic for the packing procedure of the inner cavity

A second fused silica cylinder (Q2) was placed around the third rung of the jib. The region between Q1 and Q2 was left empty to serve as the reference (outer) cavity. A quartz disk was placed on top of Q2 to prevent the reference cavity from being filled with powder during the packing of the outer cavity wall. This disk also had a 7.5 cm hole in the center of the disk. Four additional 2 mm holes were placed at 90° intervals around the center

of the disk. The holes were located directly over the reference cavity. A narrow piece of hypodermic needle encased in Spectralon was placed over each hole. The hypodermic tubing protruded through the quartz disk providing access to the reference cavity.

A piece of schedule 40 PVC was placed around the outside of Q2 and secured to the bottom rung of the base piece using four evenly-spaced screws. The region between the PVC and Q2 was densely packed with powder to comprise the outer cavity wall. An emphasis is placed on maximizing the density of particles in this region to increase the reflectivity of the outer cavity wall. Once the powder was packed to the top of Q2, an additional 2 cm piece of PVC was attached to the top of the outer PVC shell to allow for dense packing of the powder near the top of the instrument. During the packing of the bottom of the ICAM-II, the Spectralon pieces were secured so that the hypodermic tubing remained exposed to the reference cavity. Once a sufficient layer of powder surrounded the Spectralon pieces, the powder was pressed more rigorously to increase the packing density.

Once the ICAM-II was packed to the top with powder, an end cap was placed to secure the powder and close one end of the instrument. The end cap had four holes that provide access to the other end of the hypodermic tubing. This tubing was used to couple the fibers into the ICAM-II. Once the top was secured with four screws, the ICAM-II was flipped so that the base piece was on top of the instrument. The base piece was unscrewed from the PVC and removed.

With the base piece removed, the remainder of the ICAM-II could be packed with powder. The remainder of the inner cavity wall was first packed. Before the inner wall is completely packed, the 6 mm quartz detection rod was placed with one optically polished end flush with the top surface of the sample cell. A circular jig supported the detection rod while the rest of the instrument was packed. Once the inner wall was packed, the remainder of the outer wall was filled with powder. Four new hypodermic tubes encased in

Spectralon were arranged around the top disk that completely sealed the reference cavity. An additional Spectralon plug was passed through the disk. This Spectralon plug had a 5 mm hole bored through the center to provide access for the 5 mm reference cavity detection rod. Powder was packed around the Spectralon pieces to provide support during the final packing stages. The PVC extension was added to the top of the outer PVC shell to allow for dense packing of the remainder of the outer region. Once the cavity was filled completely, a top plastic disk was screwed to the top of the PVC to close the instrument.

Water Purification

Discussion of Water Purity

Water is used universally, in every lab, across all disciplines. The definition of pure water varies widely depending on the requirements of the experiment. Standards for water quality are outlined by several organizations including the American Society for Testing and Materials (ASTM), the International Organization for Standardization (ISO), the United States Pharmacopoeia (USP), and the Clinical and Laboratory Standards Institute (CLSI). Water quality is classified by its resistivity, pH at 25°C, the total organic carbon (TOC) as well as a few other factors which vary depending on the organization. The research in this study is concerned with optically pure water. The definition of optically pure water is dependent on the the wavelength range of the investigation. For example, many organic contaminants have large absorption cross sections in the fingerprint region (6.66 - 20 μm). Therefore, a study over that region would need to be more concerned with organic contamination than a study over the visible region (400 nm - 700 nm). This study was concerned with optically pure water in the ultraviolet spectrum. Unfortunately, many common water contaminants absorb ultraviolet radiation. Furthermore, ultrapure water is referred to as “hungry” water for its tendency to leach contaminants from its environment.

Water is classified into three distinct grades: Type 1, Type 2, and Type 3. Type 1 water refers to water with a resistivity greater than 18 MΩ· cm. The maximum resistivity of water is 18.2 MΩ· cm at 25°C. The total organic content of type 1 water is less than 10 parts per billion (ppb). Type 1 water is used for high performance liquid chromatography (HPLC), immunocytochemistry, mammalian cell culture, and plant tissue culture. Type 1 water is commonly referred to as reagent grade water. Type 2 water has a resistivity greater than 1 MΩ· cm and a TOC less than 50 ppb. It is used to feed clinical analyzers, electrochemistry, sample dilution, media preparation, and radioimmunoassay. Type 2 water is referred to as analytical grade and is used as the feed water for type 1 water. Type 3 water denotes water with a resistivity greater than 0.05 MΩ· cm and a TOC less than 200 ppb. This water is used in modern household appliances such as dishwashers and washing machines. It is also used in basic laboratory practices such as autoclaving.

As the technology for water purification has improved, additional designations for water purity have been applied. A type 1+ designation denotes water with the maximum resistivity of 18.2 MΩ· cm and a TOC of less than 5 ppb. This grade of water was used in trace metal detection. Because of the difficulties of ultraviolet measurements discussed in the above paragraph, type 1+ was necessary for these measurement of the absorption coefficient of pure water.

Production of Ultrapure Water

Ultrapure water is produced using two EMD Millipore commercial purification systems connected in series: the RiOs/ Elix System and the Milli-Q System. Tap water is first purified using the RiOs/Elix system. A block diagram of this system is shown in Fig. IV.10.

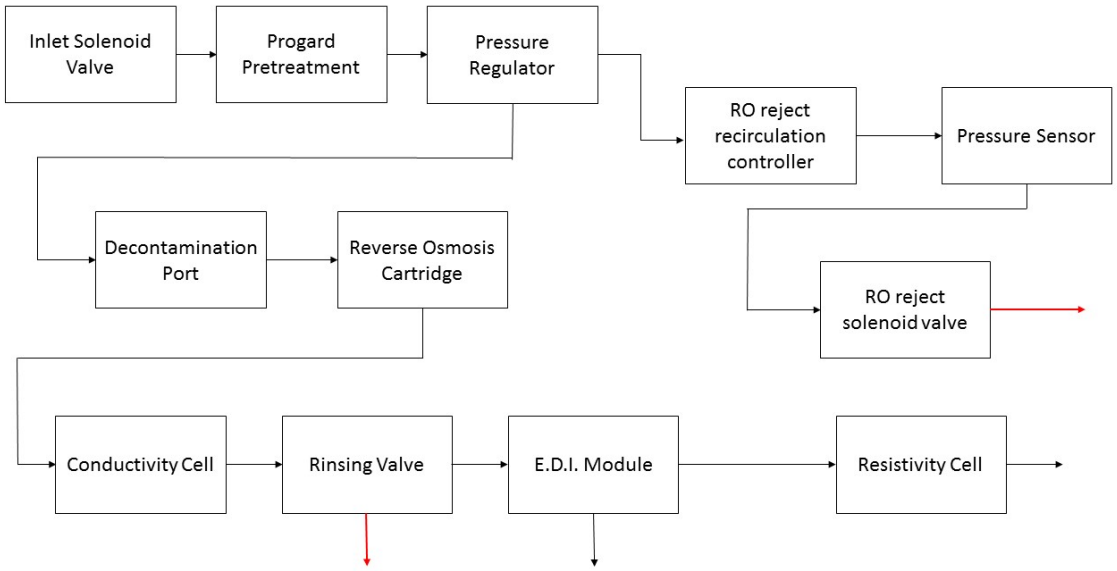

Figure IV.10: A flow schematic of the RiOs/Elix purification system

Tap water is passed through a solenoid valve and coupled into a Progard pretreatment pack. The Progard pack acts as a charcoal filter and removes particles and free chlorine from the water. In geographical regions with hard water, it may also reduce the risk of mineral scaling. Mineral scaling refers to the accumulation of hard deposits of lime, calcium and other minerals. To further reduce the risk of mineral scaling, a wire mesh screen was in front of the solenoid valve. The wire mesh screen blocks larger minerals from entering the Elix system. The water is pressurized and fed into a decontamination port with a conductivity cell. The conductivity cell monitors the quality of the water entering the system. The water is then fed into a reverse osmosis (RO) cartridge. Water and other molecules with lower molecular weights are allowed to pass through the small pores in the membrane. Larger molecules as well as water that does not pass through the membrane are discarded (or recirculated) through the RO reject line. The water quality is again mon-

itored in a conductivity cell to ensure that the RO filter is working properly. Finally, the water is passed through an electrodeionisation (E.D.I.) module. This stage further removes organic compounds and minerals. A final resistivity number is recorded to monitor output water quality. The resistivity of the output water from the Elix system is approximately 15 MΩ· cm. Purified water is stored in a sealed 60 L nalgene container. The nalgene has an air filter attached to the top to remove contamination from the atmosphere. It is important to note that ultrapure water cannot be stored because it will pull material from its containing vessel. This causes damage to the vessel over time and diminishes the quality of the water.

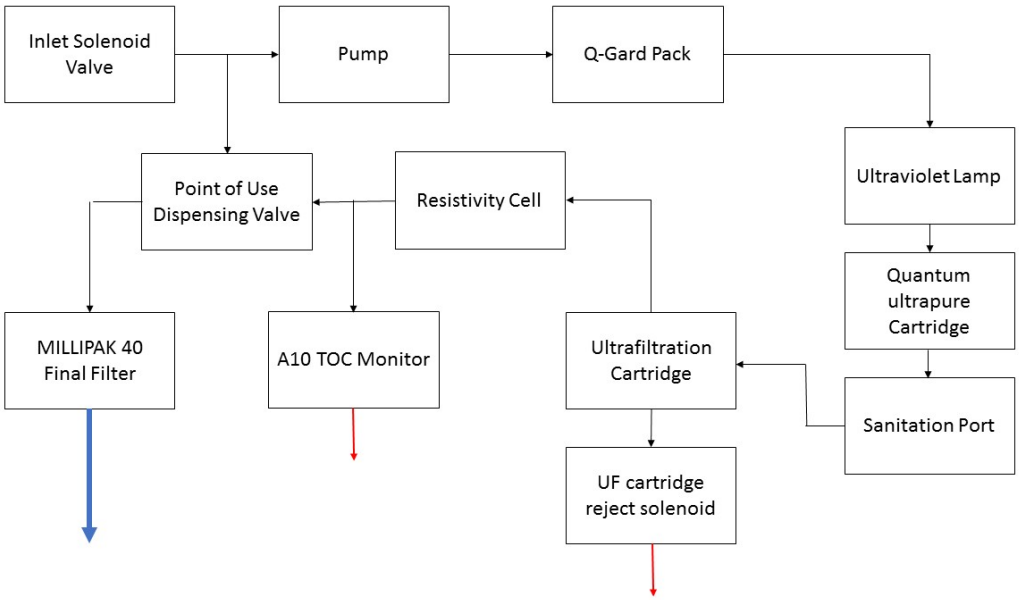

Figure IV.11: A flow schematic of the Milli-Q purification system

When ultrapure water is needed, the point of use trigger is pressed on the Milli-Q system. A block diagram of this system is shown in Fig. IV.11. The solenoid valve located

below the nalgene container is opened and water enters the Milli-Q system for final purification. The pretreated water is initially pumped through a Q-Gard purification cartridge. Water is then exposed to a UV light with emission wavelengths at 185 and 254 nm. These wavelengths oxidize organic compounds and kill bacteria. The water is then passed to the Quantum ultrapure cartridge which removes trace ions and the oxidation by-products produced from the UV irradiation. From there, the water is sent to an Ultrafiltration (UF) cartridge. The UF cartridge blocks any contaminant with a molecular weight greater than 5000 Daltons from passing through the filter. The contaminants captured by the UF filter are periodically drained through a tube connected to the city drain. The remaining water is passed through a final resistivity cell to report the final resistivity of the product water. When the system is performing to factory specifications, the final resistivity of the water is 18.2 M$\Omega\cdot$ cm. Before being expelled from the system, the product water is sent to an A10 TOC monitor which determines trace levels of organic material. Using the feed water at Texas A&M University, the water purification system is capable of reliably producing high quality water with an organic content between 3-5 ppb. If the organic content is significantly larger than 5 ppb, the filters in either the RiOs or the Milli-Q system may need to be replaced.

Product water is expelled through a 3-way manual valve. The valve is connected to a final 0.22 μm polishing filter which removes any contaminant greater than 0.22 μm from the final product. The filter also serves to prevent contamination of the system through the point of use trigger. The product from the point of use trigger qualifies as Type 1+ purity water and is suitable for absorption coefficient measurements.

Water Delivery System

Since ultrapure water leaches material from anything that it contacts, the system for

delivery to the ICAM and storage for water leaving the EMD Millipore commercial device was made from fused silica [52]. A schematic of the delivery system is shown in Fig. IV.12. Fused silica was selected for its low leaching characteristics while in contact with water. High purity water was stored in a 6 cm diameter, 1.5 meter long quartz reservoir that was tapered at the top and bottom to a 5 mm ID stem. Water was delivered to the reservoir via low-leaching Tygon tubing with a quartz valve attachment. The Tygon tubing was purged of stagnant water by running the high purity water through the tubing for approximately two minutes. This water was immediately discarded. After purging the line, the valve attachment was connected to a quartz tee using a bare quartz ball and socket joint located at the bottom taper of the reservoir. One end of the tee is connected to the reservoir while the other is connected directly to the sample cell of the ICAM-II via a 5 mm ID quartz tube. Once the reservoir was filled, the valve was closed to isolate the water in the reservoir from the Tygon tubing.

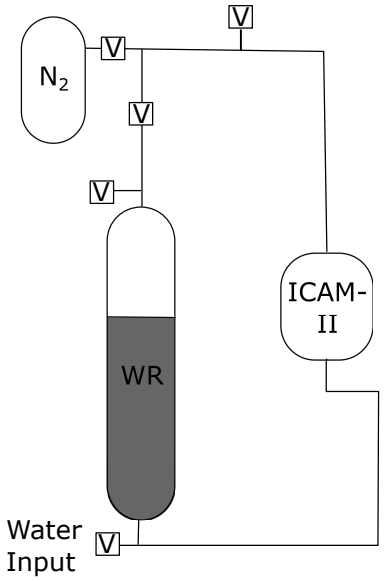

Figure IV.12: A schematic of the quartz delivery system designed to maintain the purity of the water through a complete measurement

Dissolved Oxygen

It has been well documented that Quickenden and Irvin had gone through painstaking efforts to remove dissolved oxygen from their water sample which has been shown to absorb strongly in the UV [61] . In 2014, Kröckel and Schmidt were able to reproduce the attenuation results from the Quickenden and Irvin study. Kröckel and Schmidt used a similar water system to the one used in this study. They noted that an additional cleaning step using a double quartz distillation under a pure nitrogen atmosphere did not impact the study [40]. A possible explanation for why the cleaning step has no impact is that the UV-oxidation lamp converts dissolved oxygen into ozone. That ozone oxidizes trace elements in the water that are removed through the ultrafiltration filter. Consequently, the amount of dissolved oxygen in the final sample would be reduced [50].

To verify that this observation by Kröckel and Schmidt was consistent with our Milli-Q system, separate samples were measured after being bubbled under two different high purity gas environments for 40 minutes separately, UHP Nitrogen and UHP Argon. Butler et al. showed that additional bubbling after 40 minutes had no tangible effect on the dissolved oxygen content [10]. This additional purification step also had no discernible impact on our absorption spectrum.

CHAPTER V

EXPERIMENTAL MEASUREMENTS OF THE ABSORPTION COEFFICIENT OF PURE WATER

Determination of the ICAM-II Volume Response for Water (∂S / ∂V)

The reservoir described in the section describing the water delivery system was filled with approximately 2 L of water. The top taper of this reservoir was connected to a UHP nitrogen line. The nitrogen line contained a release valve to reduce air pressure above the water in the reservoir. Conversely, the pressure above the water was increased by filling the region with nitrogen from a UHP nitrogen canister. Raising the pressure above the water "pushes" the water through the delivery tube and into the sample region of the ICAM-II. By raising and lowering the pressure above the water in the vessel, the water level inside of the ICAM-II was precisely controlled. The volume of water in the ICAM was monitored by measuring the height of the water in the quartz reservoir relative to the height of the initial filling.

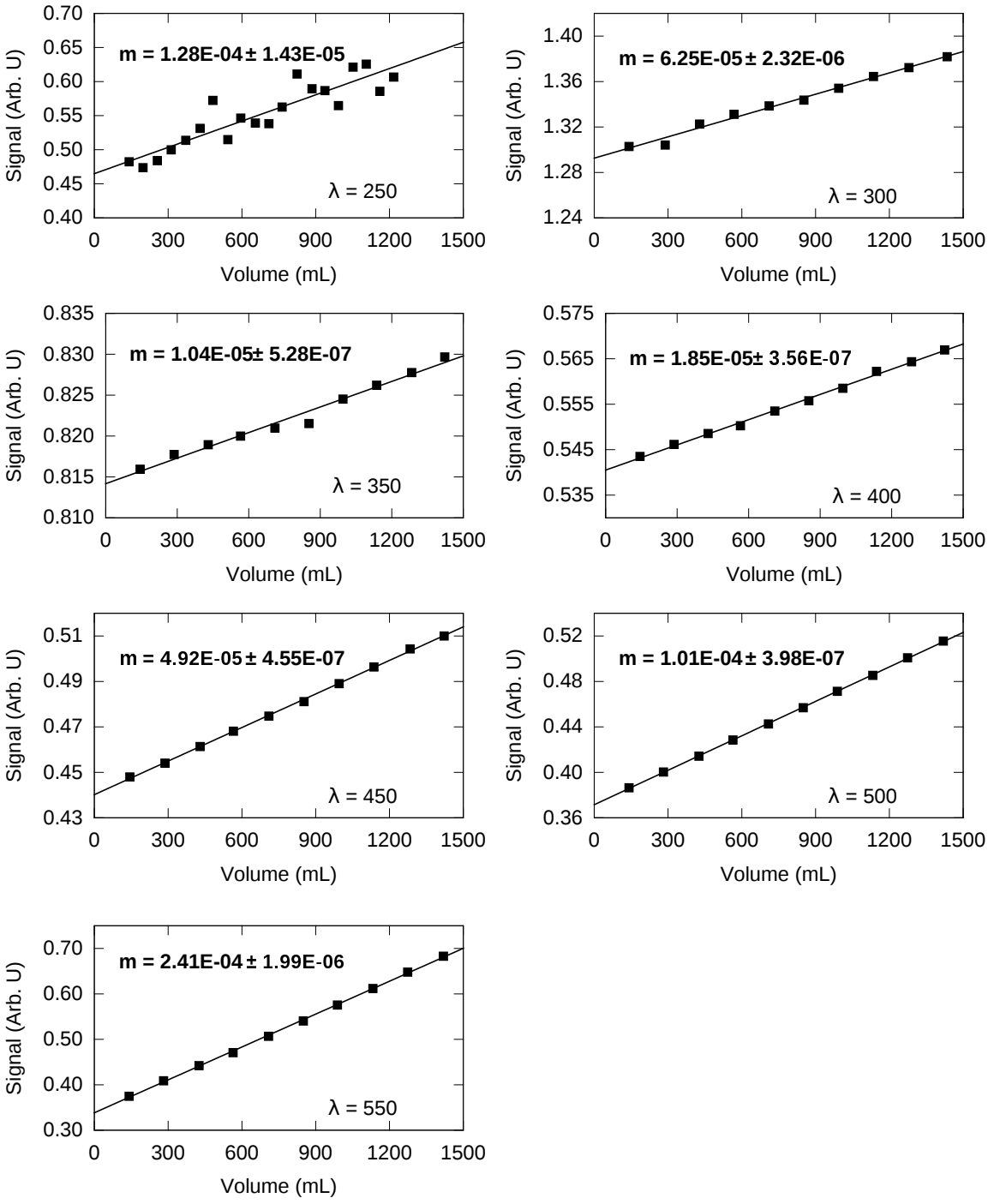

Figure V.1: A sample of the measurement of the ICAM-II signal as a function of volume. A least-squares fit is applied to each wavelength to obtain the slope.

To measure the volume response, water was first filled to the base of the ICAM-II. The volume of water in the sample cell was increased in increments of approximately 150 mL for each measurement. At each increment, S was measured 100 times and averaged at each wavelength over the desired range. $S(V)$ was determined by measuring S for at least 10 different volumes. A least squares fit was performed at each wavelength to find $\partial S \backslash \partial V$. Several of these fits are shown in Fig. V.1. Note, as evident in Fig. V.1, $\partial S \backslash \partial V$ is proportional to the absorption coefficient, α, divided by the wavelength dependent factor, C_1 (i.e. Eq. IV.18).

The slope of the volume response for pure water is shown in Fig. V.2. A step size of 10 nm was chosen for wavelengths below 300 nm to allow for a larger monochromator slit width (2000 μm). This facilitates illumination in the ICAM-II in a wavelength region where the lamp output is less.

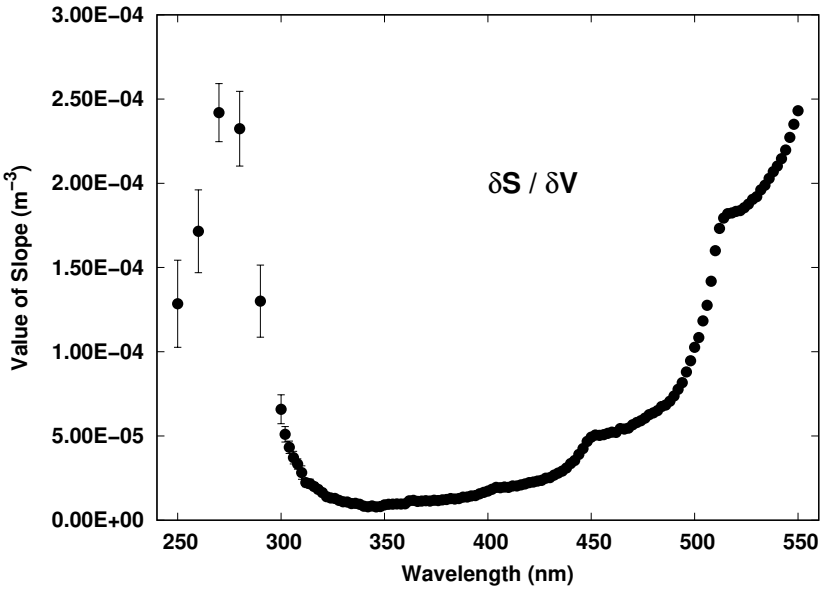

Figure V.2: Measurement of the slopes of the ICAM-II volume response for water as a function of wavelength

It is important to note that the experimental procedure used in this study varies slightly from the original Pope and Fry study. They first made a measurement with the sample region completely filled. An empty cavity measurement was subtracted from the full cavity measurement. The instrument was finally calibrated by measuring the ICAM response to incrementally increasing volumes of pure water (the same procedure as outlined above) and measuring the ICAM signal as a function of increasing absorption for several reference samples (see the following section). In the Pope and Fry method, the subtracted signal (full minus empty) serves as the basis for the water absorption measurement. In contrast, the ICAM-II does not involve a signal detector at the point where the cavity is half filled. Consequently, it just uses the instrument response to a changing volume as the raw uncalibrated data. This subtle change in methodology significantly simplifies the analysis.

Determination of ICAM-II Absorption Response ($\partial\alpha$ / ∂S)

The determination of $\frac{\partial\alpha}{\partial S}$ was accomplished by measuring the cavity response to reference samples with accurately known absorption coefficients. Irgalan Black was chosen because of (1) its lack of fluorescent response in the UV, (2) its large UV absorption cross section, and (3) its previous success in ICAM experiments [56]. The lack of fluorescent response of the dye was verified by irradiating a concentrated sample of dye with the fourth harmonic of an Nd:YAG (266 nm) and measuring the sample radiance with a spectrometer.

For the calibration, a master dye solution was prepared by dissolving $\approx 1\frac{mg}{L}$ of Irgalan Black in pure water. The master dye was then filtered through a series of Gelman SUPOR filters using a vacuum filtration system with the smallest filter being 0.2μm. The absorbance of the master dye was measured using a 1 cm Starna cell in two separate spectrophotometer systems- an Agilent Cary 6000i (accuracy of 0.0003 absorbance units) and

an Agilent 8453 UV-VIS.

A spectrophotometer uses a broadband light source and measures the intensity of light transmitted through a sample at each wavelength. Basically, it measures the attenuation of light passing through a sample. The attenuation of the beam is determined by Beers' Law, namely,

$$I = I_0 e^{-\gamma x} \tag{V.1}$$

where I is the intensity of light after it passes through the sample, I_0 is the initial intensity of the beam, x is the distance that light travels through the sample, and γ is the the attenuation coefficient. Attenuation is the loss of light through a sample due to both scattering and absorption. The attenuation coefficient is defined as $\gamma = \mu + \alpha$ and has units of inverse length. μ and α are the scattering and absorption coefficients, respectively. If the absorption coefficient is sufficiently large compared to to the scattering coefficient or $\alpha >> \mu$ then $\gamma = \alpha$. As a result, Beer's Law becomes

$$I = I_0 e^{-\alpha x}. \tag{V.2}$$

We rewrite this as

$$\frac{I}{I_0} = e^{-\alpha x}. \tag{V.3}$$

We note that in this case where the absorption is sufficiently large, the spectrophotometer measures the absorbance of a sample, not the absorption coefficient. The absorbance is defined by

$$A = \log(\frac{I_0}{I}). \tag{V.4}$$

Thus, the absorbance is related to the absorption coefficient by

$$A = \log(e^{\alpha x}) = \alpha x \log(e) = \frac{\alpha x}{2.303} \tag{V.5}$$

or solving for α

$$\alpha = \frac{2.303 \cdot A}{x}. \tag{V.6}$$

The absorbance values of the master dye varied $< 1\%$ between the two spectrophotometer systems. A plot of the resultant absorption coefficient as a function of wavelength is shown in Fig. V.3.

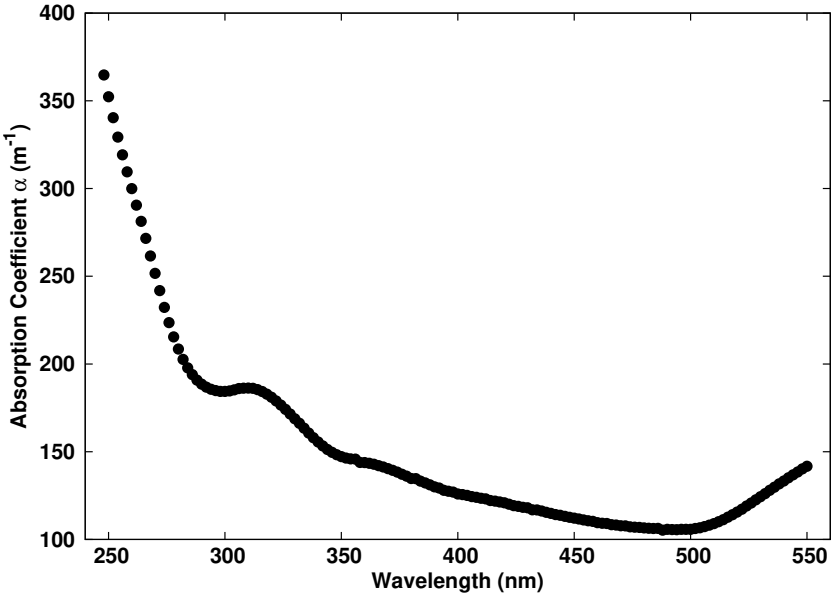

Figure V.3: The absorption spectrum of Irgalan Black measured by an Agilent spectrophotometer

The master dye was first diluted by a factor of 20 using a 200 mL volumetric flask (uncertainty 0.1%) and a 10 mL graduated pipette (uncertainty 0.2%). The 20X dilution

sample was further diluted using a 2L volumetric flask and a 2 ml graduated pipette (uncertainty 0.1%) to produce 10 reference samples containing different concentrations of dye ranging from 40,000X-4000X. The highest dilution factor (40,000X) was chosen such that the measured dye had an absorption coefficient with the same order of magnitude as the minimum absorption coefficient of water.

The diluted dye samples were loaded into the ICAM-II one by one (from 40,000X to 4,000X) and measured. S was measured 40 times at each wavelength and averaged. Note, the signal measured was a combination of the dye and the pure water solvent. However, it is assumed that the volume of water, and hence the contribution of the water absorption to the signal, for each diluted dye was constant. Therefore, $\frac{\partial \alpha}{\partial S}$ measured the ICAM-II signal change from contributions from the dye only and the contribution from the pure water was neglected.

$\frac{\partial \alpha}{\partial S}$ was calculated by first plotting the values of the absorption coefficient, α_{dye}, measured from the spectrophotometer as a function of the signal, S. A least-squares fit was performed for each wavelength. The slope at each wavelength corresponds to $\frac{\partial \alpha}{\partial S}$ for that wavelength. Examples of the fitted slopes are shown in Fig. V.4.

These slopes from the dye measurements provided the ICAM-II absorption response, as shown in Fig. V.5. The instrument was thoroughly rinsed with 18.2 M$\Omega\cdot$ cm water after each measurement.

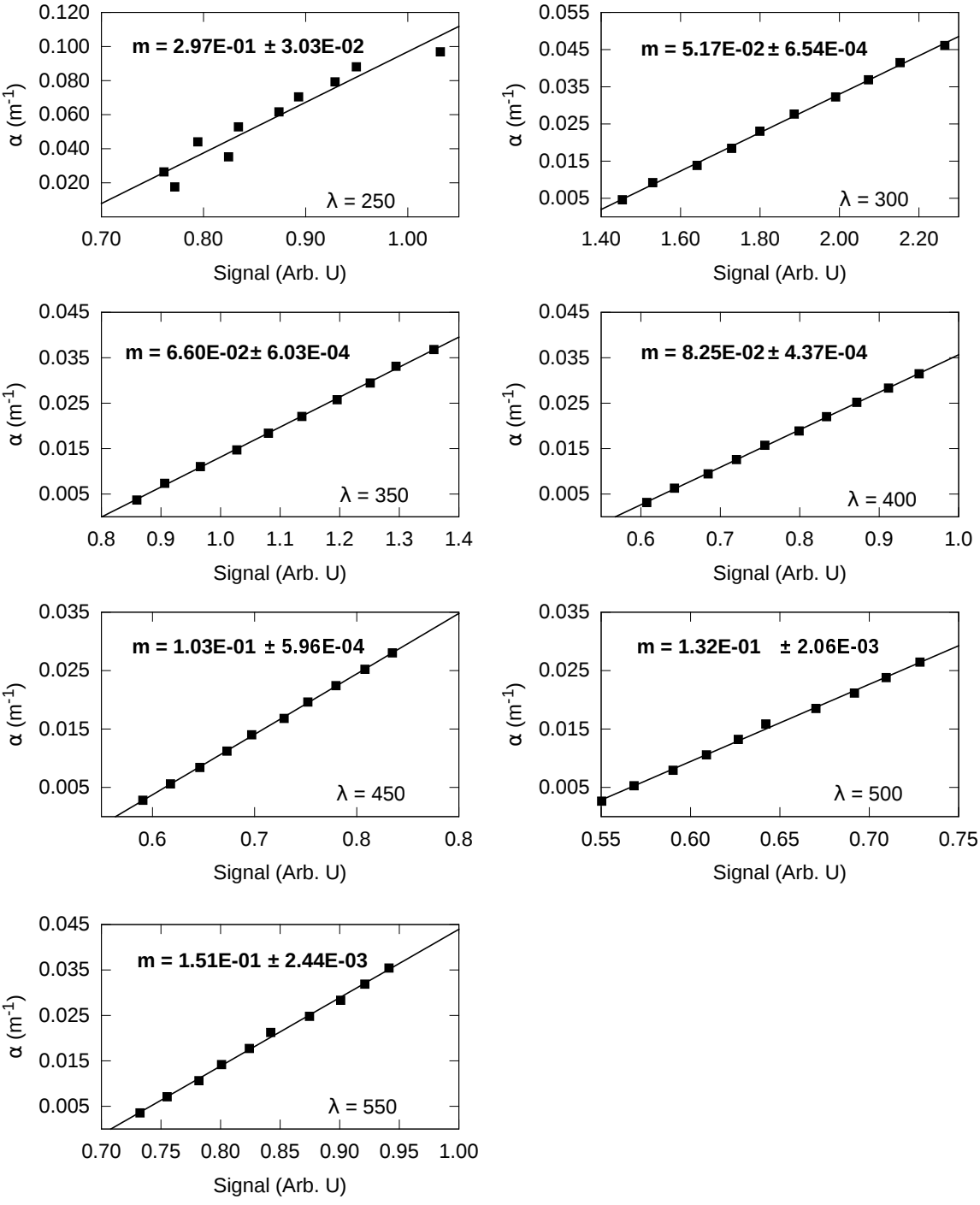

Figure V.4: Measurements of the absorption coefficient of Irgalan Black as a function of the ICAM-II signal at five of the wavelengths. A least-squares fit was applied at every wavelength.

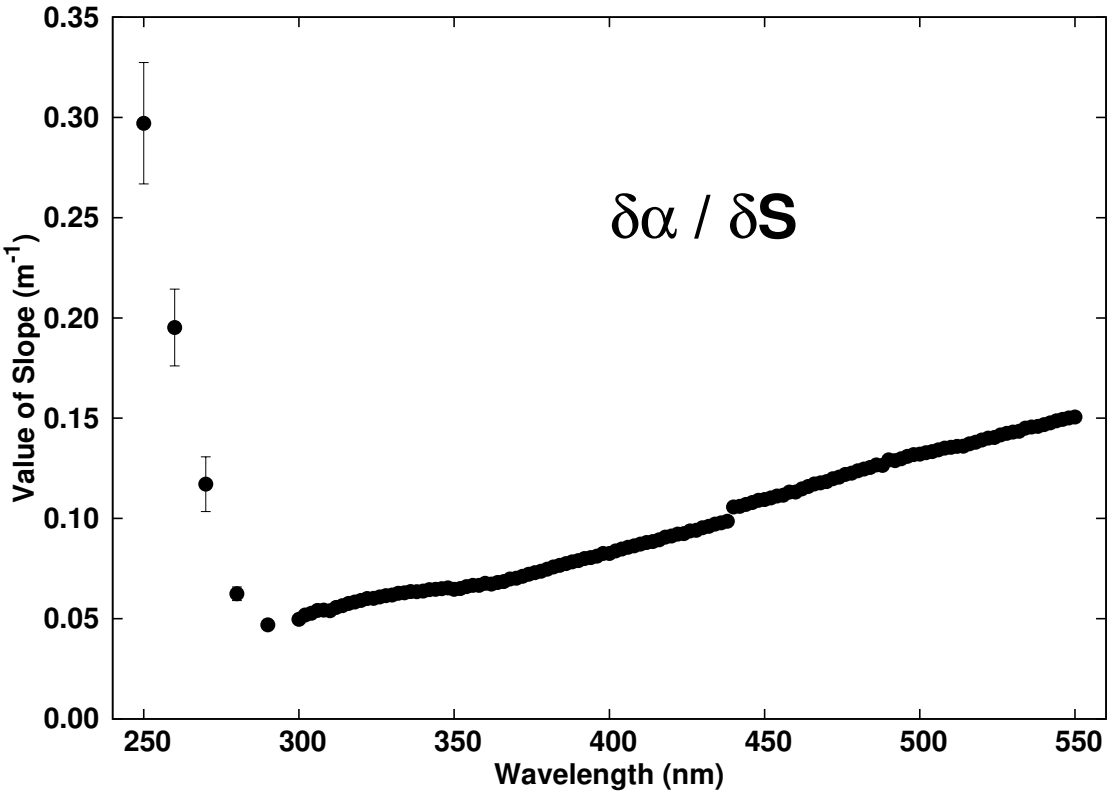

Figure V.5: Measurements of the slopes of the ICAM-II absorption response as a function of wavelength

CHAPTER VI

RESULTS AND DISCUSSION

Optical Absorption Coefficient of Water from 250 nm-460 nm

The absorption spectrum from 250-550 nm was determined for pure water via Eq. IV.23, *i.e.* by multiplying the slopes of the ICAM-II spectral response function (Fig. V.5) with the slopes of the volumetric function (Fig. V.2) and the volume of the sample cell (1538 mL). The results can be seen in Fig. VI.1. Numerical values for the measured absorption coefficients are shown in Table VI.1. Data for 310-550 nm were taken at wavelength intervals of 2 nm to reflect the nominal bandwidth of the monochromator (1.8 nm at a slit width of 600 μm). Since the absorption spectrum of pure water is assumed to be smooth, a three point moving average was applied to the points in this region to help reduce measurement noise. For 250-310 nm, the monochromator slits were widened to allow for better illumination of the ICAM-II. The wavelength intervals were therefore increased to reflect an increase in the nominal bandwidth (6 nm at a slit width of 2000 μm). Since the tail of the first electronic transition centered around 147 nm is predicted to be featureless, no information is lost with the decrease in resolution in the 250-310 nm spectral region [36].

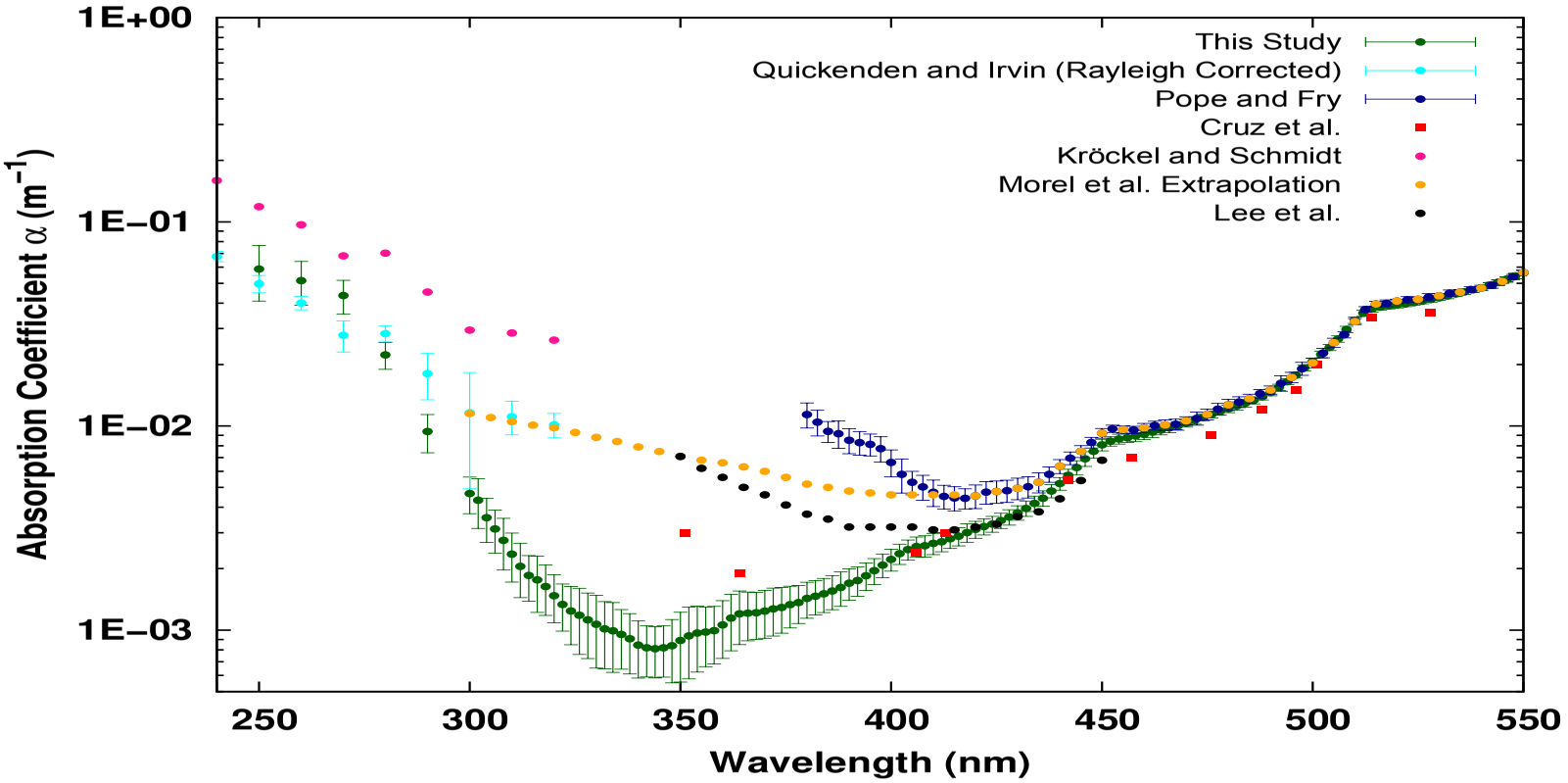

Figure VI.1: The absorption coefficient, α, of pure water measured in this study along with the results from several other high quality studies: Pope and Fry [56], the Rayleigh scattering corrected Quickenden and Irvin values [61], Cruz et al. [19], Lee et al. [46], Morel et al. Extrapolation [51], and Kröckel and Schmidt [40].

Table VI.1: Absorption Coefficients, α_w (m^{-1}), and Error, σ (m^{-1}), for Pure Water as a Function of Wavelength, λ

λ (nm)	α_w (*10^3)	σ (*10^3)	λ (nm)	α_w (*10^3)	σ (*10^3)
250	58.71	17.79	356	0.98	0.32
260	51.50	12.44	358	0.99	0.31
270	43.57	8.19	360	1.06	0.33
280	22.30	3.34	362	1.15	0.35
290	9.39	2.00	364	1.20	0.35
300	4.67	0.96	366	1.21	0.32
302	4.33	1.18	368	1.22	0.32
304	3.56	0.87	370	1.24	0.33
306	3.13	0.75	372	1.27	0.34
308	2.75	0.78	374	1.29	0.33
310	2.36	0.64	376	1.33	0.31
312	2.05	0.61	378	1.37	0.29
314	1.85	0.47	380	1.43	0.29
316	1.76	0.54	382	1.47	0.28
318	1.63	0.45	384	1.51	0.29
320	1.47	0.39	386	1.55	0.29
322	1.33	0.35	388	1.62	0.31
324	1.24	0.39	390	1.70	0.30
326	1.18	0.42	392	1.75	0.29
328	1.12	0.40	394	1.85	0.28
330	1.07	0.42	396	1.96	0.28
332	1.01	0.37	398	2.08	0.28
334	0.99	0.37	400	2.22	0.27
336	0.95	0.31	402	2.37	0.27
338	0.91	0.30	404	2.48	0.28
340	0.85	0.26	406	2.57	0.29
342	0.82	0.23	408	2.59	0.31
344	0.81	0.23	410	2.66	0.32
346	0.82	0.23	412	2.71	0.29
348	0.84	0.29	414	2.80	0.29
350	0.89	0.33	416	2.88	0.30
352	0.94	0.36	418	3.00	0.31
354	0.97	0.34	420	3.12	0.30

Table VI.1: Continued

λ (nm)	α_w (*10^3)	σ (*10^3)	λ (nm)	α_w (*10^3)	σ (*10^3)
422	3.21	0.29	488	13.91	0.49
424	3.31	0.29	490	14.60	0.54
426	3.44	0.31	492	15.45	0.55
428	3.58	0.31	494	16.48	0.54
430	3.76	0.34	496	17.74	0.58
432	3.95	0.36	498	19.26	0.68
434	4.17	0.38	500	20.73	0.74
436	4.42	0.36	502	22.42	0.85
438	4.80	0.38	504	24.24	0.84
440	5.22	0.40	506	26.68	0.96
442	5.74	0.50	508	29.71	1.06
444	6.26	0.57	510	33.00	1.22
446	6.90	0.55	512	35.69	1.23
448	7.51	0.52	514	37.38	1.23
450	8.08	0.44	516	38.21	1.31
452	8.42	0.48	518	38.78	1.29
454	8.63	0.45	520	39.17	1.29
456	8.77	0.56	522	39.62	1.17
458	8.93	0.52	524	40.17	1.25
460	9.09	0.52	526	40.88	1.18
462	9.33	0.57	528	41.62	1.20
464	9.55	0.51	530	42.42	1.17
466	9.79	0.51	532	43.30	1.25
468	9.99	0.46	534	44.36	1.29
470	10.30	0.42	536	45.41	1.40
472	10.65	0.45	538	46.45	1.36
474	11.00	0.42	540	47.54	1.42
476	11.38	0.44	542	48.82	1.41
478	11.77	0.46	544	50.40	1.50
480	12.14	0.52	546	52.24	1.50
482	12.54	0.60	548	54.25	1.63
484	12.94	0.55	550	56.29	1.84
486	13.36	0.53			

The results in this study shift the wavelength for the minimum absorption of pure water from 418 nm to 344 nm. Many scientists in the large detector field have already been

operating under the assumption that the true minimum of water was found at a wavelength near 350 nm [1]. On the long wavelength side of this minimum, the absorption spectrum, which derives its structure from the vibrational structure of water, behaves exponentially (not accounting for harmonic structure) with a decay constant consistent with other high quality studies. On the short wavelength side of the minimum, the absorption spectrum (which is dictated by the tail of the first electronic transition) also behaves exponentially.

In previous versions of the ICAM, the volume response and the absorption response were measured by fitting data sets with ≈ 20 increments in volume and in dye dilutions; this study focused on measuring at a smaller number of increments but with higher accuracy and precision. A single increment for the volume response in the Pope and Fry study used 10-20 averages at given volume while this study used 100 averages at each increment to further suppress background fluctuations and more reliably detect small contributions [56]. In addition, due to the low irradiance of the cavity at 250 nm, 20 volume increments were measured with 100 averages to help address further noise concerns. As a result, the slopes fitted from the volume response in this study had significantly less error for small absorption coefficient values.

Due to the effectiveness of using a large number of averages during the volume response measurements, a similar approach was taken with the absorption response measurements. Error bars for the final absorption coefficient values of water were calculated using a combination of the standard deviation from several measurements as well as the slope uncertainty from each of the fitted slopes.

The absorption coefficient of pure water is greatly influenced by three distinct factors for wavelengths $<$400 nm. First, ultraviolet absorption measurements are particularly sensitive to organic contamination. Nucleic acids have a strong absorption peak centered around 260 nm with a tail that continues far into the longer wavelengths of the ultraviolet [76]. As a result, a sample with a small number of organics can overestimate the ab-

sorption coefficient of that sample particularly when the sample absorption is weak. The organic content of the water in this study is consistent with the exceptional water quality of the most recent studies (3-5 ppb). Second, Heidt and Johnson (1951) have shown that dissolved oxygen can increase the measured absorption. Quickenden and Irvin introduced many exhaustive steps to remove dissolved oxygen [31]. However, Kröckel and Schmidt demonstrated that many state-of-the-art, commercially-available water systems are capable of producing water with comparable levels of dissolved oxygen to Quickenden and Irvin. While reproducing the attenuation results of Quickenden and Irvin, Kröckel and Schmidt noted that "an additional cleaning step with a double distill under nitrogen atmosphere did not change the lab analysis nor the UV spectra of our water" [40]. This is consistent with the results of this study which observed that additional bubbling of N_2 and Ar through the Milli-Q water had no impact on the absorption spectrum. Furthermore, since the minimum absorption in this study is much lower than any other well-regarded study, the hypothesis that dissolved oxygen impacts this study is likely implausible as it would cause the absorption to be larger, not smaller, than the previous studies. Finally, several studies have demonstrated a redshift in the ultraviolet absorption spectrum due to temperature [68]. While a detailed temperature investigation is outside the scope of this study, we note that the water was measured at a temperature of 23 ± 0.5°C.

The results in this study agree with the Rayleigh-corrected values of the Quickenden and Irvin [61] and the Kröckel and Schmidt [40] studies from 250-300 nm (within error bars). However, for λ >300 nm, the data from the many high quality studies diverges from the data obtained using ICAM-II. As highlighted in the introduction to this study, these studies measured the attenuation of a pure water sample, not the absorption. The absorption was obtained after applying a scattering correction based on calculations from the best scattering parameters. This problem is sufficiently highlighted when comparing the Quickenden and Irvin study with the Kröckel and Schmidt study. While both studies

measured the same attenuation, the studies disagreed on the absorption because of the choice of scattering correction. Furthermore, if the scattering is much larger than the absorption, subtle absorption features can be obfuscated by the overwhelming scattering losses. These problems are eliminated with a scattering independent measurement like the ICAM-II.

Similarly, the final results are in excellent agreement with Pope and Fry for wavelengths > 440 nm [56]. Fig. VI.2 shows the present results for pure water absorption with the locations of several harmonics from the O-H stretch. Resonances from the seventh and eighth harmonics of the O-H stretch that are consistent with previous efforts are still visible [55]. In fact, these data demonstrate the first known observation of the ninth harmonic of the O-H stretch. This appears as a small feature at 364 nm which was predicted by Tam and Patel in the equation

$$\nu_n = n(3620 - 63n)\text{cm}^{-1} \tag{VI.1}$$

where n denotes harmonic order. However, the results from the Pope and Fry study suggest that the absorption of water begins to increase below 420 nm. Recall that the original ICAM was made with Spectralon which, in addition to having a lower reflectivity, will absorb UV radiation and even degrade under long term exposure [42]. This increased absorption of Spectralon can cause an overestimation of the absorption coefficient. Since fumed silica does not begin to significantly absorb until $\lambda < 250$ nm, the ICAM-II is better suited to measure samples between 250-400 nm.

We finally compare the recent results in this study with the results of Cruz et al. The Cruz et al results were met with some skepticism for two reasons: i) they lacked an additional step to remove dissolved oxygen from the water produced by the Milli-Q system and ii) they differed from the well-established studies. Since this study uses the same Milli-Q

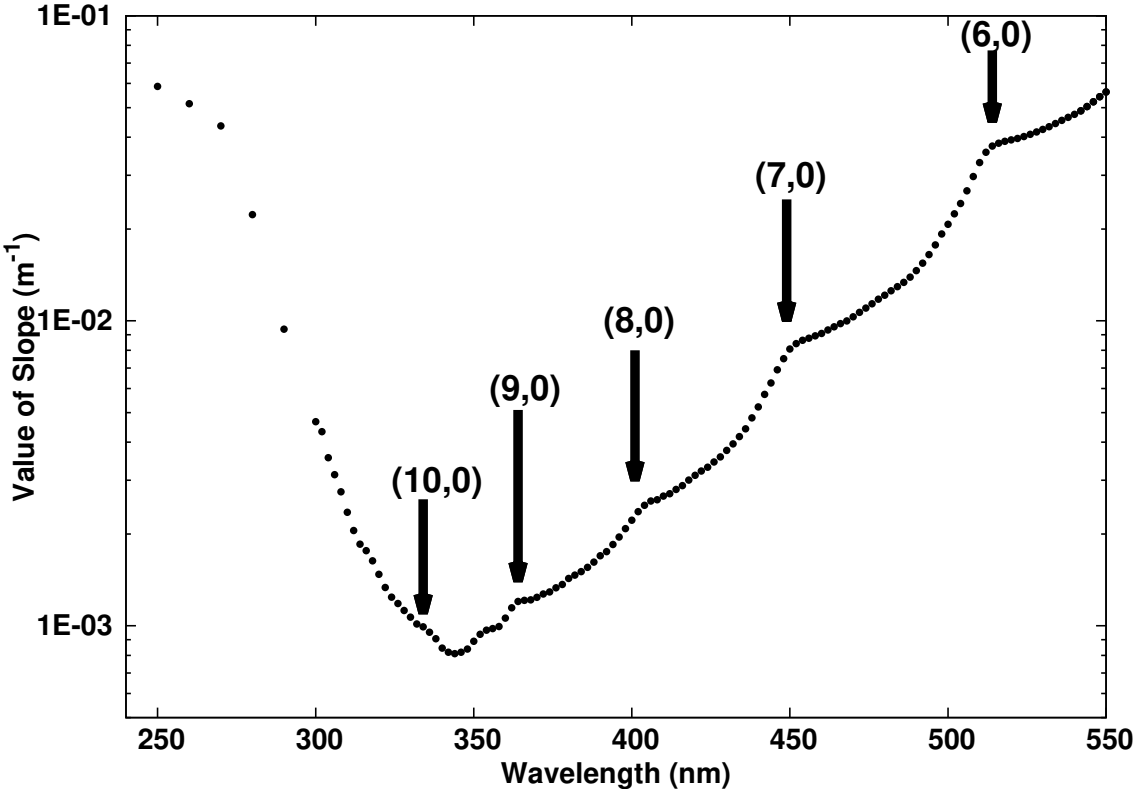

Figure VI.2: Present results for pure water. (n,0) denotes the nth harmonic of the pure O-H stretch (no scissor mode combination). A large arrow is used to show the predicted locations of those harmonics.

purification system as Cruz et al., the dissolved oxygen discussion in this manuscript applies to their study as well. The results in this study agree remarkably well with Cruz et al. down to 364 nm within error bars. The difference the two studies at 350 nm may be the result of an unaccounted loss due to scattering effects [19].

Detailed Comparison of the Obtained Values with Results from Pope, Sogandares, and Zheng

In the above results section, some hypotheses were made to explain the differences between the data presented in the Pope and Fry study and the data presented in this study.

Because the data from Pope and Fry has been well cited and corroborated by other groups, a detailed explanation for the discrepancies is useful. In addition to the ICAM used by Pope and Fry, a third ICAM (ICAM-I) has been used to measure the absorption from $300 - 550$ nm. This ICAM replaces the inner cavity wall of the Pope and Fry ICAM with quartz powder. The remainder of ICAM-I is unchanged from the original instrument with a Spectralon outer wall. While two dissertations (Lu and Wang) have been written about the ICAM-I, no results were published due to data discrepancies with existing data and theory [48, 78]. Initial work for this dissertation research was done with the ICAM-I but replication of the results from Lu and Wang were never achieved. This might have been due to contamination in the glass cell from contact with various acids. The discussion in this section explains how the overall sensitivity of each instrument impacts the final measured results in the different studies.

The absorption response curve in Chapter 5 is equivalent to the sensitivity function for the ICAM or ICAM-II. If $\frac{\partial \alpha}{\partial S}$ is small, the cavity sensitivity is high. Likewise, if $\frac{\partial \alpha}{\partial S}$ is large, the cavity sensitivity is low. For example, Fig.V.5 shows that the ICAM-II is most sensitive at 295 nm. For $\lambda < 295$ nm, the sensitivity rapidly decreases. This is shown by the large increase in the absorption response curve. When measuring the absorption coefficient of pure water, the diminished sensitivity at 295 nm is mitigated by the fact that the absorption coefficient of water is rapidly increasing.

In comparison, Fig. VI.3 shows the absorption response for the original ICAM. The original ICAM has slowly diminishing sensitivity for wavelengths between 410-500 nm. For $\lambda < 410$, the sensitivity of the original ICAM drops rapidly, much like the ICAM-II behavior for $\lambda <$295 nm. However, at 410 nm, the absorption coefficient is approximately a factor of 10 lower than the absorption at 295 nm. Therefore, the values obtained by the original ICAM are more susceptible to errors from decreased sensitivity than the values obtained with the ICAM-II.

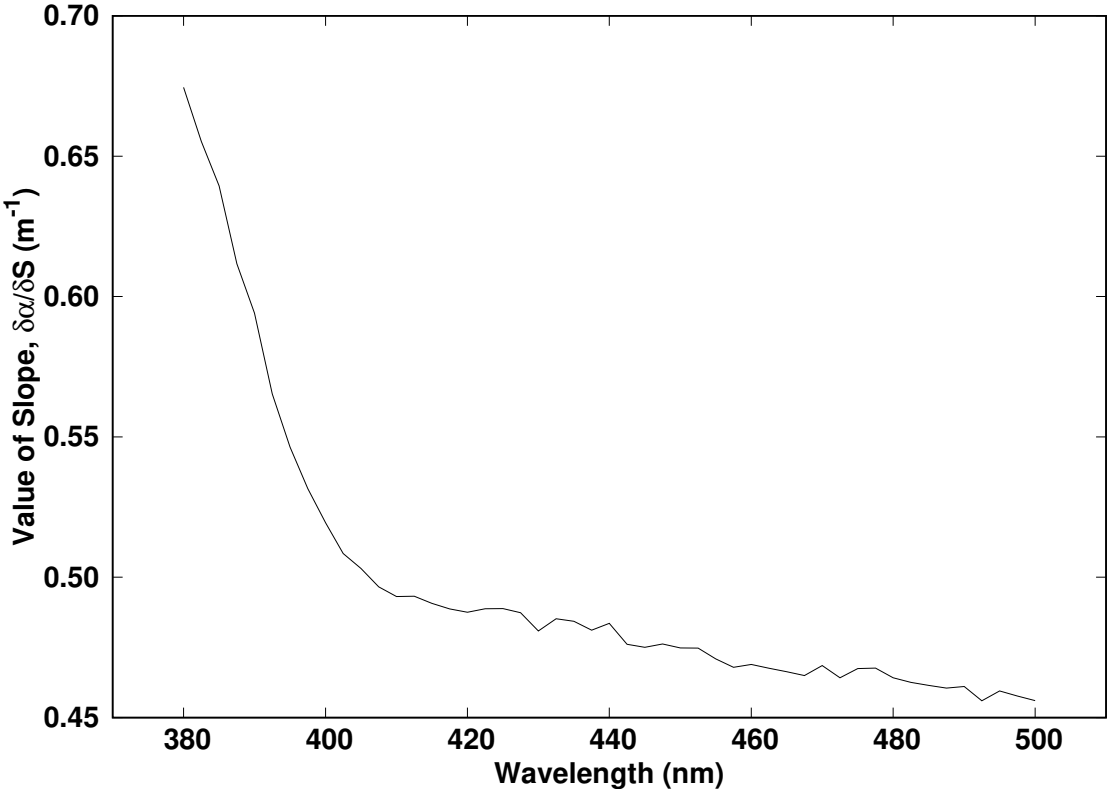

Figure VI.3: The sensitivity function of the original ICAM used in the Pope and Fry experiments. Large slope values indicate low sensitivity [56].

We note that even if the ICAM does not have the sensitivity to measure the desired sample, the sensitivity function for an ICAM can always be found by carefully choosing the more concentrated dilutions of calibrating dye. For example, if the absorption of a weakly interacting sample is too small to be resolved by the ICAM at a given wavelength, the ICAM signal would reach some terminal value. After applying the normalization calibration from the dye, the resulting multiplication factor would cause the ICAM to significantly misevaluate the absorption coefficient of the sample. To avoid this potential complication a dilution where the absorption coefficient is less than or equal to the minimum absorption of the sample can be chosen to calibrate the instrument. In this case, any sensitivity issues

will appear as a deviation from the linear behavior of the absorption response calibration at any given wavelength. However, this solution requires that the wavelength of the sample absorption minimum and the approximate value of that minimum be known before applying the calibration. If the true absorption minimum is lower than the hypothesized value, it may be impossible to resolve whether the instrument has adequate sensitivity.

Recall that in addition to the volume response and absorption response measurements, the Pope and Fry (as well as Lu and Wang) study measured the signal from both an empty and a full cavity. In the original version of the ICAM, the difference between the empty and full cavity was first measured. Due to a change in the index of refraction in the sample region, the light lost through the top and bottom stem as well as the coupling of light into the detection fiber is changed. This results in the signal in the inner cavity being lower than the inner cavity signal of the empty cavity regardless of the absorption properties. In other words, even if the sample has no absorption, the signal in the inner cavity will still be smaller than the inner cavity signal for an empty cavity. This difference in signal is referred to as a net offset and is wavelength dependent. For the Pope and Fry study, this offset was characterized by performing the volume response measurement and fitting the resulting values as a function of wavelength to a 4-parameter function. The fitting parameters were then used to define an offset calibration constant, namely, C_0'. After the absorption independent offset was characterized, the instrument sensitivity was then assessed by measuring the absorption response discussed earlier to find the normalization constant, C_1. Therefore, using Eq.IV.17 (where S is the difference between the full and empty cavity), Pope and Fry were able to find the absorption coefficient for a given sample.

$$\alpha = \frac{C_1}{4V}(S - C_0') \tag{VI.2}$$

We will consider the two cases where insufficient ICAM sensitivity could have pro-

duced the errors in the ICAM absorption coefficient measurement of pure water by Pope and Fry.

In the first case, we consider the situation where the ICAM cannot resolve the difference between the empty and full cavity for a given wavelength region. In this scenario, the ICAM will still measure a difference between the empty and full cavity due to the absorption independent offset. Fig VI.4 compares the signal from an empty cavity (average of 10 repetitions) with the signal from a water-filled cavity (repetition of 10 averages) measured using ICAM-I. The signal from the empty cavity and the signal from the full cavity in Fig. VI.4 are indistinguishable for 350 $\lambda <$ 390 nm due to both (i) a decrease in the sensitivity of the instrument and (ii) a decrease in the absorption of pure water in this region.

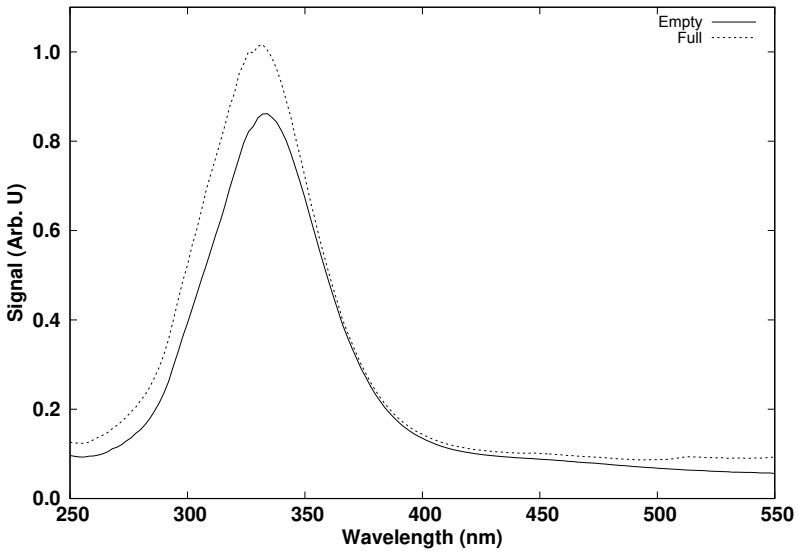

Figure VI.4: Signal for an average of 10 repetitions for the empty and water-filled ICAM-I

The signals from the empty and full were subtracted. The difference between the signals as a function of wavelength is shown in Fig. VI.5.

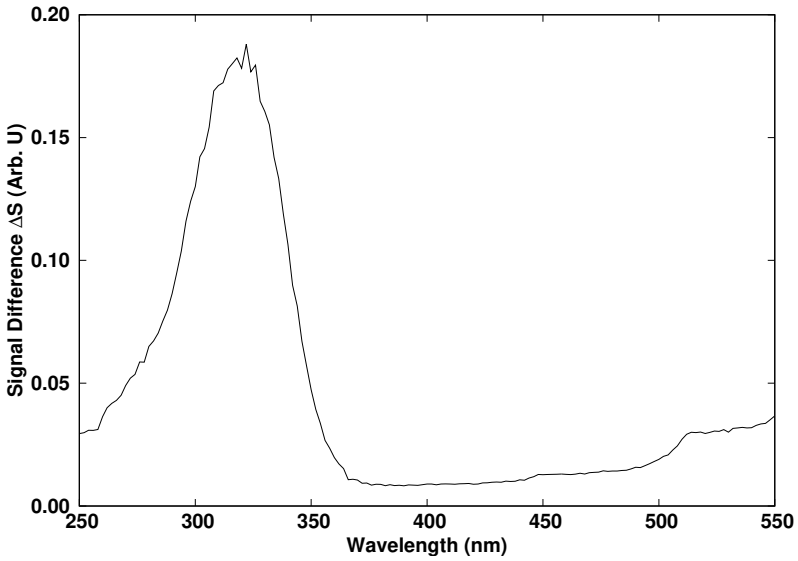

Figure VI.5: Difference between the measured spectra for the empty and full cavity for ICAM-I

Initially, it appears that a distinct difference between the empty and full spectra is obtained in Fig. VI.5. However, this difference is likely due to the offset and not the absorption of the sample. As a result, the difference between the signals of the empty and full cavity converges to a value that is approximately equal to the net offset. For the Pope and Fry experiment, the offset between 380 nm and 600 nm was measured to be approximately 0.01. More concisely, this implies that

$$\Delta S_{REAL} < \Delta S_{MEAS} \tag{VI.3}$$

where ΔS_{REAL} is the real difference between the empty and full cavity due to sample absorption and ΔS_{MEAS} measured is the measured difference between the empty and full cavity. Furthermore, since absorption from a full cavity has little impact on the ICAM signal, the absorption from the volume increments used to calibrate offset is would indistinguishable from noise. Hence, the linear fits for these measurements would be poor. As

a consequence, the 4-parameter fit used to characterize the offset would be inaccurate particularly for low absorption coefficient values. However, since the dye calibration could still be measured accurately, the low sensitivity of the instrument would yield a large value for the normalization constant, C_1. The multiplication of C_1 would give a larger value for the absorption coefficient then the true value since

$$\alpha = \frac{C_1}{4V}(S_{MEAS} - C_0'). \tag{VI.4}$$

In the second case, consider an ICAM where the difference between the empty and full cavity is able to be resolved by the ICAM, but incremental changes from increasing the sample volume are indistinguishable from noise. As in case 1, if the increase cannot be resolved, the measurement of the slope for the signal as a function of volume will be unreliable. If the offset value is on the same order of magnitude as the difference between the empty and full cavity, small errors in the offset value can have significant impact on the final absorption value. Once the large values of the dye calibration are multiplied by the offset-calibrated difference spectra, the error is multiplied. It is important to note that since the offset constant is defined as

$$C_0' = k_1 + k_2\lambda \tag{VI.5}$$

the offset correction subtracts a constant that is linear as a function of wavelength from the subtracted signal. If the difference between the empty and full cavity is smooth and shows absorption features of the sample, the final absorption coefficient measurement for the ICAM will also be smooth and show the appropriate absorption structure of the sample. However, because of the multiplication factor from the dye calibration, the absolute values of the absorption spectrum could be off by a significant amount. Therefore, it cannot concluded that just because an ICAM study shows the appropriate resonance structure,

that the numerical values of the absorption coefficients are guaranteed to be correct.

We conclude that the measurements performed by Pope and Fry (as well as Lu and Wang) are hindered by a lack of instrument sensitivity. The absorption spectrum of pure water in this study diverge at the minimum value for the Pope and Fry study, where instrument sensitivity becomes increasingly important (Fig. VI.3). This is especially apparent when examining the offset function in the original Pope and Fry paper. The statistical fluctuations produced from the offset calibration are very large and, for shorter wavelengths, are on the order of the offset itself. For small absorption values, these fluctuations can have a significant effect on the overall results. In contrast, the volume response obtained in this study is free from the large statistical fluctuations that plagued the data in the Pope and Fry study. Furthermore, we notice that minimum value for the absorption coefficient of pure water obtained in the Pope and Fry study corresponds to the point where the sensitivity of the ICAM begins to greatly decrease. As a result, the values for C_1 begin to rise rapidly at 417.5 nm.

A subtle, but important, distinction between this study and the Pope and Fry study must be highlighted. In both the offset calibration and the ICAM response calibration, the measured slope values are fitted as a function of wavelength to provide a fit function for that calibration. As a result, the calibration for any given wavelength is loosely dependent on the measurements from all other wavelengths. This does not appear significant for the response calibration but can have large implications for the offset calibration. While a three-point average is applied to final absorption coefficient values to reduce noise in this study, each measurement in the present study completely independent from any measurement made at a different wavelength; in other words, the results in this study are equivalent to running an independent measurement for each wavelength.

Impact of Pure Water Contact with Plastic on the Optical Absorption of a Water Sample

The aggressiveness of ultrapure water has been well-established in this work as well as many others. We have previously described how ultrapure water pulls material from its surrounding environment. We further argued that because of the low-leaching properties of quartz when in contact with water, all delivery and containing vessels that will be in contact with the measured UHP water needed to be made from quartz glass. To assess the importance of this quartz, a 30 cm section of quartz tubing between the reservoir and the ICAM-II was replaced with a one foot long piece low leaching Tygon tubing. Ultrapure water was in contact with the Tygon tubing during the duration of the measurement of the sample's absorption coefficient. The Tygon tubing was then replaced with a smaller piece of one inch plastic shrink tubing. The absorption of a pure water sample was also measured with the shrink tubing in place. The results, compared with the absorption coefficient of pure water are shown in Fig. VI.6 with the absorption spectrum for pure water.

Notice that the absorption coefficient for the water is much larger for the sample that had been in contact with the Tygon tubing than the absorption coefficient for pure water in the ultraviolet. This is because Tygon is a plastic which is made of long chains of hydrocarbon polymers. The polymer chains found in plastics have a large UV absorption cross section that increases rapidly from 350 nm to 266 nm. In our sample, the material leached from the Tygon tubing deposits UV absorbing polymers into the pure water sample. Therefore, the absorption coefficient of the sample was increased particularly in the region where the optical absorption of water is small.

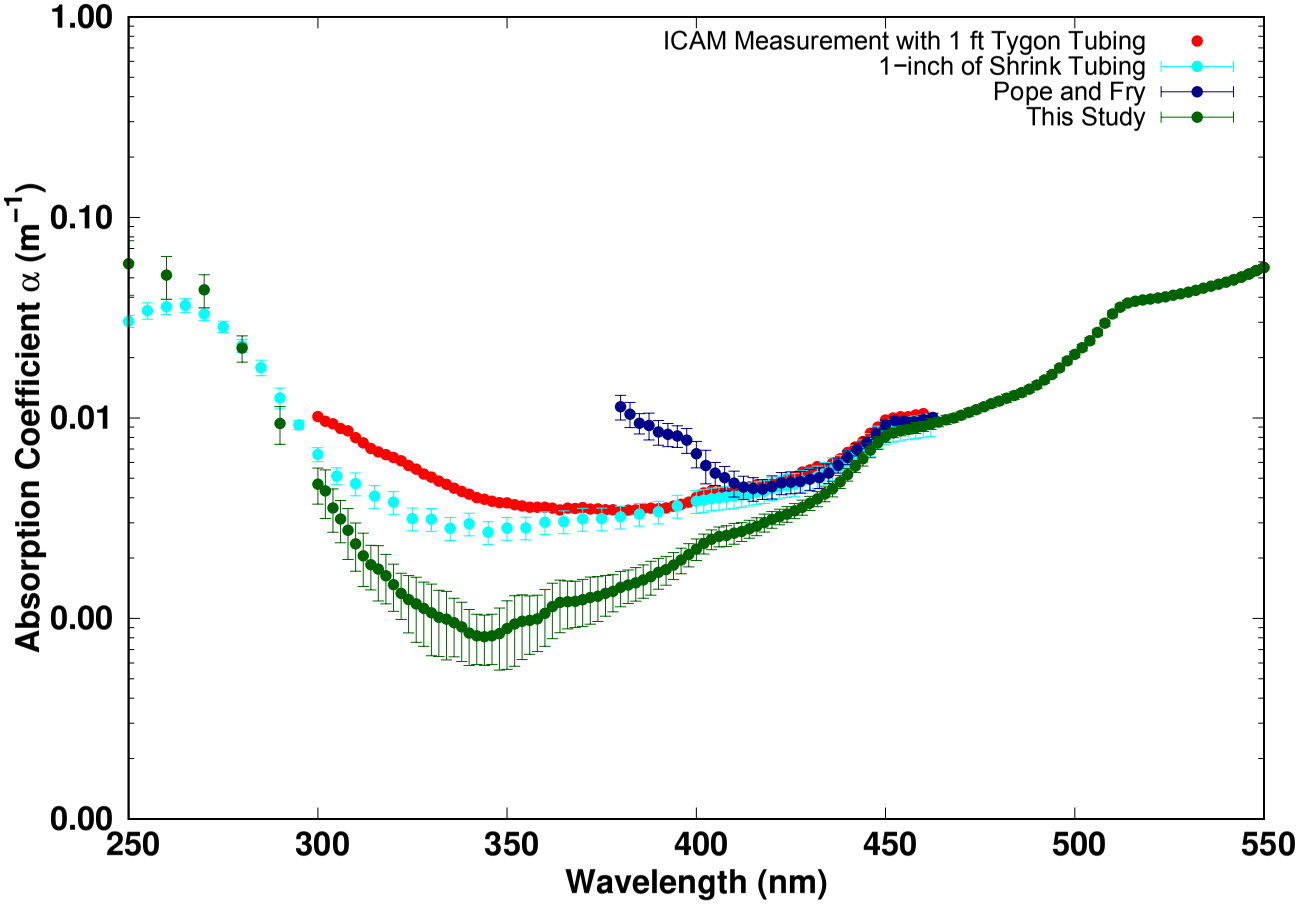

Figure VI.6: The absorption coefficient of water taken with a one foot long piece of Tygon tubing and a one inch piece of shrink tubing replacing a section of the quartz delivery tubing

CHAPTER VII

SOURCES OF ERROR AND ERROR ANALYSIS

In this chapter, we will discuss the sources of error that contribute to the error bars in an ICAM measurement. Because the ICAM is designed for precision absorption measurements, the measurement error is small but important. Sources of error the ICAM include: (1) variability in the sample of interest and (2) jitter from the phase lock loop of the lock-in amplifier and (3) dilution errors from the calibrating dye. We will discuss each of these sources briefly and assess their impact on the pure water absorption spectrum.

Variability in the Sample of Interest

Because the ICAM-II is designed to measure the absorption coefficient of weakly-absorbing samples, the instrument is very susceptible to small impurity variations from sample to sample. While the water purity in this study is comparable to the high-purity water samples in other studies, the water in these studies still contain trace organic compounds (3-5 ppb) as well as trace levels of dissolved gas (particularly O_2) [40]. The effect of the measurement fluctuations as a result of the slight differences in the purity of water was minimized by averaging the values over five different samples. The impact of the variation of sample purity on the measurement is assessed by examining the standard deviation of the samples. The expression for the standard deviation is given by

$$\sigma = \sqrt{\frac{\Sigma(x-\mu)^2}{N}} \tag{VII.1}$$

The standard deviation of the five samples can be as large as 20% when the absorption values are at a minimum (near 344 nm). However, the raw value of the standard deviation

at each wavelength varies little. Since it is unlikely that any additional compounds would have a uniform absorption spectrum (particularly in the ultraviolet), the large standard deviations, particularly for small values, are not expected to be caused by variations in the sample purity.

Jitter from the Phase Lock Loop

When making measurements with a lock-in amplifier, a reference frequency is required. The reference frequency is passed to the lock-in amplifier and the lock-in detects a signal at that frequency. Lock-in amplifiers create their own internal reference signal using a phase-locked-loop locked to the reference signal. However, jitter and phase-modulated noise can introduce small fluctuations in the measured intensity on the lock-in amplifier. Furthermore, the reference signal is generated by continuously measuring the chopper blade frequency using a built-in laser gating system. While the frequency of the chopper wheels are stable, they do exhibit a slight 'wobble' causing the rotational frequency to vary by $\pm$ 1 Hz. (Recall that the Chopper wheel frequencies are approximately 1.2 and 1.5 kHz.) This jitter causes slight variations in the measured intensity at each lock-in amplifier.

To eliminate this source of error, each data point is the average of 100 measurements taken at a rep rate of 1 Hz. Jitter fluctuations are further eliminated with each additional point used to fit the slope. This error is accounted for when combining the fitting error with the standard deviation from the multiple samples. The fitting error for a linear slope is found using the expression

$$SE = \sqrt{\frac{1}{N-2}\frac{\sigma_Y}{\sigma_X}} \tag{VII.2}$$

where N is the number of fitted data points and σ_Y and σ_X are the sum of squares devia-

tions of the data points from the corresponding fit point.

Dilution Errors from the Calibrating Dye

In addition to the above errors, slight imperfections in the dilutions can contribute small sources of error to the final results. Due to uncertainties in the volumes of the pipette and the volumetric flask, the experimental dilution factor may be slightly greater than/ or less than the intended value. This can introduce small errors into calibration measurement.

The dilution errors are mitigated by measuring several different dilution samples. By performing a linear fit of these dilutions as a function of their absorption coefficients, the error can be reduced by $\sqrt{N}$. Here, N is the number of measured points. The absorption coefficient of the diluted sample is obtained by measuring the absorption spectrum of the master dye with a spectrophotometer and dividing by the expected dilution factor. The dilution error is obtained through the slope fitting error of the dye dilutions.

CHAPTER VIII

INTRODUCTION TO CAVITY RING-DOWN AND INTEGRATING CAVITY RING-DOWN SPECTROSCOPY

The previous sections demonstrated the use of integrating cavities to measure an intensity drop due to the absorption of a sample. In this section, integrating cavities will be used to measure the absorption of a sample in the temporal domain. This measurement is called Integrating Cavity Ring-Down Spectroscopy and will be discussed in great detail in the coming chapters.

Cavity-Ring Down Spectroscopy

To understand the theory behind ICRDS, first consider traditional Cavity Ring Down Spectroscopy (CRDS). CRDS was first developed by O'Keefe and Deacon in 1988. CRDS involves injecting a temporally short pulse into a highly reflective (reflectivity, $\rho \approx 99.9\%$) two mirror cavity as seen in Fig. VIII.1. At each reflection from the mirror, a percentage of light energy, determined by the mirror reflectivity, is lost through the surface of the mirror. With each successive reflection from the cavity mirrors, more light energy is lost. As a result, the intensity of light inside the cavity exponentially decays or "rings-down" as a function of time according to some characteristic decay constant, namely,

$$I(t) = I_0 e^{\frac{-t}{\tau}} \tag{VIII.1}$$

where I_0 is the initial input intensity and τ is the characteristic decay constant.

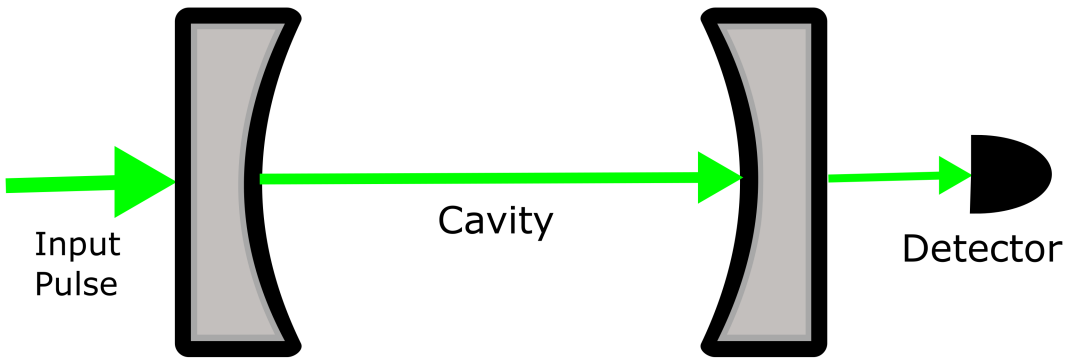

Figure VIII.1: A sample cavity for a cavity ring-down measurement

In an empty cavity, the decay constant is a function of the speed of light in the cavity, c, as well as the cavity length, l such that

$$\tau_{EC} = \frac{l}{c}\left(\frac{1}{1-\rho}\right), \tag{VIII.2}$$

where ρ is the mirror reflectivities.

If a sample is placed in between the two cavity mirrors (see Fig. VIII.2), the characteristic decay constant will decrease. In addition to the losses at each mirror, light energy is lost through both absorption and scattering from the sample. Accounting for the additional attenuation losses, Eq. VIII.2 becomes

$$\tau_S = \frac{l}{c_s}(\frac{1}{1-\rho+X+\alpha l}) \tag{VIII.3}$$

where c_s is the speed of light in the sample, X is the losses due to scattering, and α is the absorption coefficient of the sample. Assuming $\rho \approx 1$ and solving for the absorption coefficient, it follows that

$$\alpha = \frac{n}{\tau c} - \frac{X}{l}. \tag{VIII.4}$$

Notice that when $X << \alpha l$, cavity ring down spectroscopy provides an excellent method for measuring the absorption coefficient of the sample. In this case, the scattering contribution is neglected and the absorption coefficient becomes

$$\alpha = \frac{n}{\tau_S c}. \tag{VIII.5}$$

If the contribution from scattering becomes too large compared to the absorption coefficient, an alternative method must be used to directly measure the absorption coefficient of the sample. Under these conditions, ICRDS provides an alternative method that is independent of scattering effects.

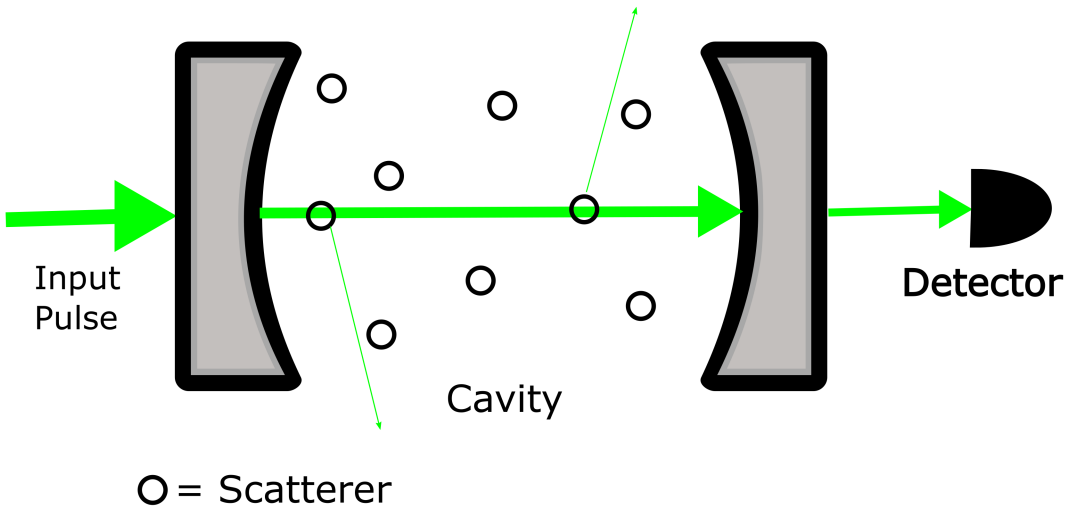

Figure VIII.2: A schematic of the impact of scattering on a cavity-ring down measurement

Integrating Cavity Ring Down Spectroscopy (ICRDS)

Integrating Cavity Ring Down Spectroscopy (ICRDS) is a spectroscopy method that exploits the isotropic field of an integrating cavity spectroscopy with the sensitivity of CRDS to provide a method of accurately measuring the absorption coefficient of a turbid sample. [21, 53, 82]. Like CRDS, ICRDS involves injecting a temporally short (6-8 ns) laser pulse into a highly reflecting ($\rho \approx 0.9985$) cavity. However, instead of using a two mirror cavity, a diffuse reflecting integrating cavity is used. For years, the highest commercially available diffuse reflecting material available was Spectralon ($\rho \approx 0993$); it did not have a high enough reflectivity to perform measurements using ICRDS. The increase in reflectivity provided by our development of fumed silica ($\rho \approx 0.9992$) increased the sam-

ple path length. Fumed silica increases the interaction with the sample due to an increase in effective path length [17, 7].

We first consider a pulse in an empty integrating cavity with a perfect Lambertian behavior. When the pulse reaches the first wall, the pulse will travel a distance into the wall. Because the wall is made from irregularly sized particles, the light will diffuse through the wall, scattering in all directions. When the light re-emerges from the wall, the reflected light propagates in all directions with a Lambertian distribution (cos θ). Light energy equivalent to $1 - \rho$ is lost at the first reflection. At each subsequent reflection from the cavity wall, light is diffused in a similar manner to the first reflection and $1 - \rho$ of the light energy is lost. After many reflections, the injected pulse into an empty integrating cavity will decay or "ring down" much like cavity ring down.

To better understand the differences between ICRDS and CRDS, consider Fig. VIII.1. The linear cavity used in CRDS guarantees that light always travels the same path length through the sample. Notice that for a cavity of length l, the detector will measure a signal from the light transmitted through the mirror at every round trip of the cavity, $2l$, or at a time interval of $2nl/c$. Note that n is the index of refraction of the medium inside the cavity. For a Gaussian input pulse, the detector will observe evenly spaced Gaussian pulses (with the spacing a function of the cavity length) with exponentially decreasing intensities. An exponential fit is applied across the top of the Gaussian peaks to find the characteristic decay constant. A sample CRDS curve is shown in Fig. VIII.3.

Comparatively, since the diffuse reflecting walls of the integrating cavity distribute the light isotropically and homogeneously in the cavity, the cavity ring-down signature becomes a constant exponential function convoluted with the initial input pulse.

$$\tau = -\frac{1}{\ln \rho}\left(\frac{\bar{d}}{c} + \delta t\right), \tag{VIII.6}$$

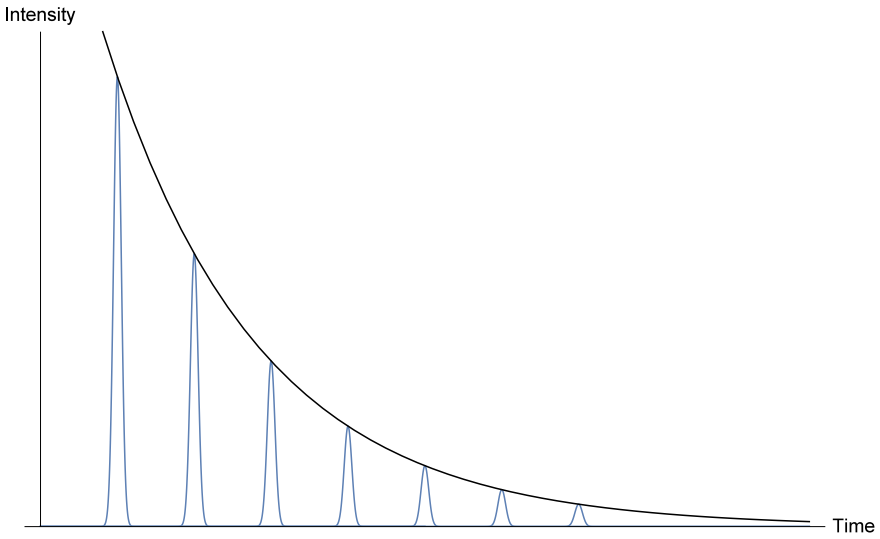

Figure VIII.3: A detection curve for a CRDS measurement

where τ is the decay constant, ρ is the cavity wall reflectivity, $\bar{d}$ is the average distance light travels between reflections from the wall, c is the speed of light, and δt is the time the light spends in the wall. The average distance between reflections from the wall of an arbitrarily shaped integrating cavity has been described by Fry et. al. [26]. For a cylinder of diameter D and height H, it is

$$\bar{d} = \frac{2DH}{2H + D}. \tag{VIII.7}$$

If an absorbing sample fills the cavity, an injected pulse will decay faster due to the additional loss from absorption. The pulse decays as

$$\tau = -\frac{1}{\ln \rho + \alpha \bar{d}} \left(\frac{\bar{d}}{c} + \delta t \right), \tag{VIII.8}$$

where α_s is the absorption coefficient of the sample. Because cells need a habitable environment to maintain viability, the measurement of the absorption coefficient of living cells must be performed with the cells dissolved in the buffer solution. Filling a cavity com-

pletely with a cell buffer is mixture is feasible, but generally will result in a very dilute mixture with a long load time. Furthermore, cell viability is only reliable for approximately 30-45 minutes after sample preparation so measurements must be taken quickly and accurately. As a result, cell measurements are often performed in a cavity that is only partially filled because of the ease of loading and unloading the sample. With a partially filled cavity, Eq. VIII.8 becomes

$$\tau_s = \frac{1}{(-\ln\rho + (\alpha_{PBS} + \alpha_c)\bar{d}_s)}\left(\frac{\bar{d}}{c} + \frac{\bar{d}_s}{c_s} + \delta t\right) \tag{VIII.9}$$

where α_{PBS} is the absorption coefficient of the buffer, α_c is the absorption coefficient of the cells, $\bar{d}$ is the average distance that light travels in the unfilled region of the cavity between reflections from the cavity wall, $\bar{d}_s$ is the average distance that light travels in the sample region of the cavity between reflections from the cavity wall, c is the speed of light in the in the empty cavity and c_s is the speed of light in the sample. The decay constant for an identical volume of a solution consisting of only buffer fluid is described by

$$\tau_B = \frac{1}{(-\ln\rho + \alpha_B\bar{d}_s)}\left(\frac{\bar{d}}{c} + \frac{\bar{d}_s}{c_s} + \delta t\right) \tag{VIII.10}$$

Subtracting the inverses of Eq. VIII.9 and VIII.10, the result becomes

$$\tau_s^{-1} - \tau_B^{-1} = \frac{\alpha_s\bar{d}_s}{(\frac{\bar{d}}{c} + \frac{\bar{d}_s}{c_s} + \delta t)} \tag{VIII.11}$$

Similarly, the decay constant of a dye solution with a known absorption coefficient (again with the same volume) is measured according to

$$\tau_{dye} = \frac{1}{-\ln\rho + \alpha_{dye}\bar{d}_s}(\frac{\bar{d}}{c} + \frac{\bar{d}_s}{c_s} + \delta t) \tag{VIII.12}$$

By measuring two separate and distinct dilutions of the a master dye solution and

subtracting their inverses, the result becomes

$$\tau_{D1}^{-1} - \tau_{D2}^{-1} = \frac{(\alpha_{D1} - \alpha_{D2})\bar{d}_s}{(\frac{\bar{d}}{c} + \frac{\bar{d}_s}{c_s} + \delta t)} \tag{VIII.13}$$

where $D1$ and $D2$ represent the different dye dilutions. By dividing Eq. VIII.11 by Eq. VIII.13, the expression becomes

$$\alpha_c = \frac{\tau_s^{-1} - \tau_B^{-1}}{\tau_{D1}^{-1} - \tau_{D2}^{-1}}(\alpha_{D1} - \alpha_{D2}) \tag{VIII.14}$$

Therefore, the absorption coefficient for the dissolved cells can be found by obtaining the values for the absorption coefficient of the master dye. If the absorption coefficient of the master dye is sufficiently large, then its absorption can be measured with a commercial spectrophotometer. The absorption coefficient for the two dilutions are obtained by dividing the master dye absorption coefficient by the dilution factors.

CHAPTER IX

MEASUREMENT OF THE ABSORPTION COEFFICIENT OF LIQUID SAMPLES

An artistic representation of an ICRDS experiment is shown in Fig. IX.1. In this section, we will discuss the requirements for an integrating cavity measurement of a liquid sample. To summarize, an Nd:YAG-pumped optical parametric oscillator (OPO) emits a tunable laser pulse into one end of a fiber optic cable. Before the pulse is coupled into the fiber, a pair of filter wheels are used to help control wavelength and intensity properties of the beam. The opposite end of the fiber optic is placed inside the cavity. An identical fiber is placed 90° away from the viewing direction of the input fiber to sample the irradiance from the cavity wall. The second fiber is then coupled directly into a detector. Signal acquisition and scanning from the OPO are accomplished through a comprehensive LabView Visual Interface.

Pump Laser

The OPO system is pumped using a Spectra-Physics Quanta-Ray Pro 290 neodymium-doped yttrium aluminum garnet (Nd:YAG) laser. The gain medium for Nd:YAG lasers, Nd^{3+}:YAG, is a five level system with four lasing transitions in the near infrared. Nd:YAG lasers have narrow gain bandwidth of 0.6 nm which allows for a high efficiency pump process. These lasers can be pumped by either a a separate laser diode or through flashlamps. Because of the strong broadband absorption around the flash lamp emission of 800 nm, flashlamp pumping is very common for high energy systems. This is the method used by

The cell and tissue experiments describe in this chapter as well as later chapters were performed at the Triservice Research Laboratory in San Antonio. This research was carried out under tissue sharing protocols under IACUC RHDO-15-12

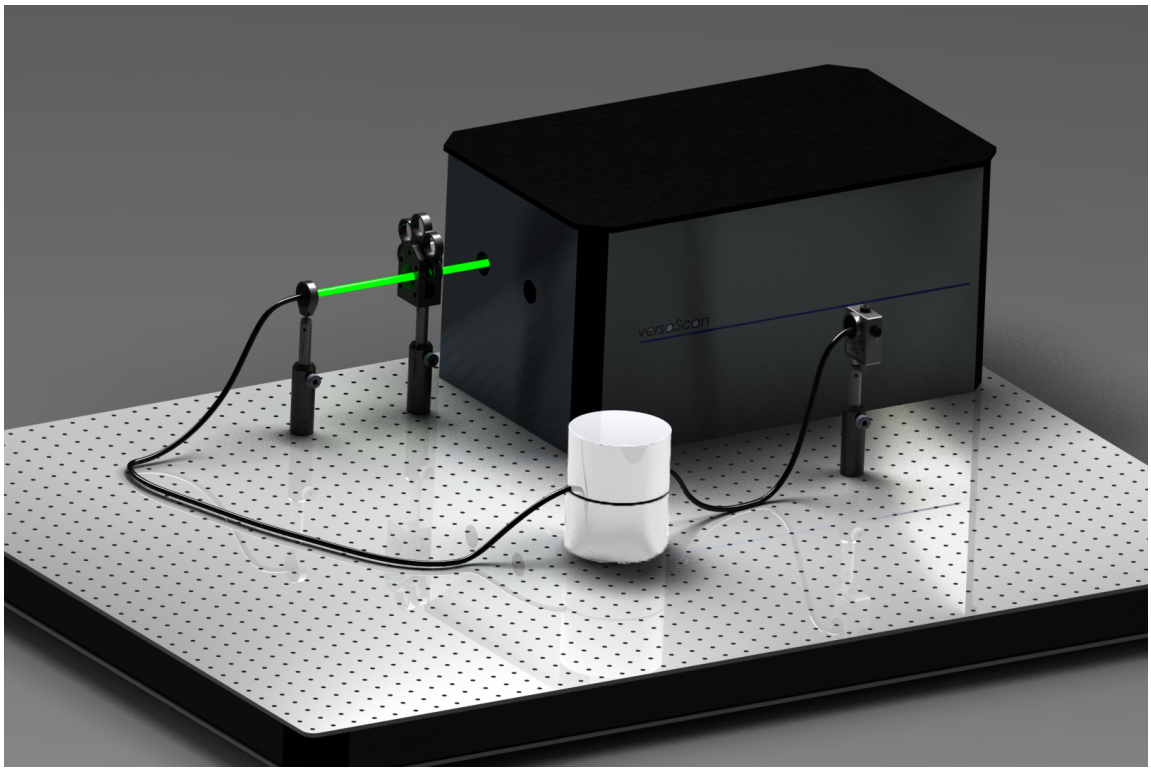

Figure IX.1: A schematic of the experimental setup of an ICRDS measurement

the Quanta-Ray Pro 290 system.

While laser emission wavelengths of 946, 1064, 1123, and 1319 are all achievable with Nd:YAG systems, 1064 nm is the most commonly used laser emission since it is the strongest transition. Achieving other emission wavelengths requires suppression of stimulated emission of the 1064 nm line. This can be achieved through the use of dichroic mirrors designed to reduce the cavity Q factor (a parameter that is proportional to the average lifetime of a resonant photon in the cavity) for 1064 nm.

With a 1064 nm laser emission, the second, third, and fourth harmonics at 532, 355, and 266 nm are obtained. Harmonic generation involves combining the energies of two or more photons to create a single photon with energy equal to the combined energies of the two photon. Recall that the energy for a photon is inversely proportional to the wavelength

by

$$E = \frac{hc}{\lambda} \tag{IX.1}$$

such that the second harmonic of 1064 nm is 532 nm. That is, the energy from two 1064 nm photons combine to form a single 532 nm photon. A schematic of the process has been provide for your convenience in Fig. IX.2 where the dotted line represents a virtual energy level. The process is usually performed in a nonlinear crystal such as barium borate (BBO) or periodically poled lithium niobate (PPLN). The harmonic conversion efficiency, the efficiency in which two lower energy photons combine to make a higher energy photon, is determined by phase matching within the nonlinear crystal. Phase matching requires that a proper phase relationship between two interacting photons within a nonlinear crystal be maintained. This is often performed by adjusting the spatial orientation of the nonlinear crystal with respect to the incoming beam.

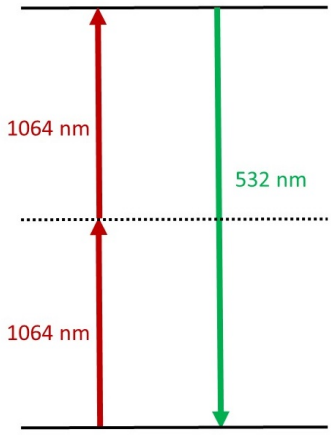

Figure IX.2: Energy level structure of second harmonic generation from an Nd:YAG laser

Operation Procedures and Specifications for the Pump Laser

Operation of the Quanta-Ray 290 first requires an external chilled water line to cool the distilled water circulation system for flash lamp cooling through use of a heat exchanger. Distilled water is used in contact with the flash lamps since impurities can diminish the lifetime of the lamp. Once circulation of the distilled water is initiated, a high voltage is applied to the flashlamps to provide a simmer current through each lamp. A simmer current is a resting current that is applied to maintain the plasma between flashes of the lamp. This reduces the total amount of energy needed for each pulse of the flash lamp. A 20 minute warm-up time is applied to allow the system to reach a steady-state temperature. When the temperature is reached, the flash lamps are pulsed and the system is allowed to pulse with the Q-switch in the off position to inhibit lasing. At this time, the amplifying stage is powered up to maximize the power output during operation. After 30 minutes, the Q-switch is placed in the on position. The laser emission is passed through a second and third harmonic crystal to generate a 532 nm and 355 nm beam. The energy output of the third harmonic, 355 nm, is observed using a Coherent power meter. If the total power output is poor, the position of the second or third harmonic (or both) crystal needs to be adjusted to improve phase matching. This is accomplished by adjusting the knob on two separate micrometers located inside the laser cavity. Adjustments made to the second harmonic crystal will always impact the third harmonic crystal. Therefore, the second harmonic crystal is always optimized first. The two crystals are adjusted until a maximum energy is reached.

Once fully operational, the Spectra Physics Quanta-Ray 290 Nd:YAG produces 2 J of 1064 nm (1 J of 532 nm, 550 mJ of 355 nm, etc.) at a repetition rate of 10 Hz. The maximum power is only achievable while the amplifying stage is in use. The factory specifications quote the temporal pulse width to be 8-12 ns for 1064 nm. For shorter

wavelengths, the temporal pulse width is less.

Optical Parametric Oscillator

An Optical Parametric Oscillator uses parametric conversion to convert the energy from a strong pump wave into two lower energy output waves, the signal and idler, in a crystal with a large nonlinear susceptibility. This process is consistent with conservation of energy in that,

$$\omega_p = \omega_s + \omega_i, \tag{IX.2}$$

where $\omega_{p(s,i)}$ denotes the frequency of the pump(signal, idler) and conservation of momentum,

$$\mathbf{k}_p = \mathbf{k}_s + \mathbf{k}_i \tag{IX.3}$$

where $\mathbf{k}_i$ denotes the respective wave vector. The signal is always denoted as the wave with the higher frequency for historical reasons. If the nonlinear crystal is placed in the cavity where either the signal or idler are resonant, amplitude gain can be achieved for the resonant wave, yielding laser-like emission similar to stimulated emission. It is important to note that the OPO is different from an optical parametric amplifier (OPA) in that the nonlinear crystal is placed inside of a resonant cavity for an OPO. The resonator helps to amplify the gain of either the signal or the idler.

Eq. IX.2 and Eq. IX.3 imply that an infinite number of signal and idler combinations are achievable. Different frequency combinations are achieved by adjusting the phase-matching condition. OPO tuning is accomplished by rotation of the nonlinear crystal or by changing the temperature. Rotation is often preferable due to its fast response.

Standard Operation and Specification of OPO

The versaScan 355 Broadband OPO operates by rotating a specially coated BBO crystal using a computer controlled actuator. When the OPO is powered down, the crystal is returned to a resting position. To avoid damage to the BBO crystal during the OPO initiation cycle, the OPO is powered with the pump laser turned off. This is often performed during the electronic warm up stage of the pump laser when the Q-switch is not engaged. Once the actuator has finished moving the BBO crystal into position, the Q-switch is engaged and pumping of the OPO begins.

Since the nonlinear frequency conversion of the BBO crystal is temperature dependent, a warm-up time of 10-20 minutes is required to achieve efficient output. If after a sufficient warm-up time, the output energy of the OPO is low, the output energy of the the third harmonic is checked and adjusted for maximum output.

To ensure that the proper wavelength is obtained, a system calibration must be performed to ensure that the electronically controlled actuator moves the crystal into the appropriate position. A spectrometer is used to sample the output of the OPO. The output pulse is never fired directly into the spectrophotometer as large pulse energies can cause permanent damage. The spectrometer measures the spectral output at several wavelengths along the total spectral range of the OPO. When a certain wavelength is selected, the OPO tunes the actuator to a designated position specified by a calibration file. To re-calibrate the OPO, the OPO is tuned to the appropriate actuator position for each wavelength, if the output wavelength deviates from the desired wavelength, electronically adjust the position of the actuator until the desired wavelength is reached. This process repeats for approximately 5 different wavelengths. Once each wavelength is successfully calibrated, a calibration function assigns actuator positions to the remaining wavelengths, resulting in reliable spectral production.

The versaScan 355 Broadband OPO has a maximum output pulse energy of 205 mJ (signal + idler) over a spectral range from 410-2550 nm. The repetition rate is determined by the pump pulse which is set to 10 Hz. The OPO has a quoted bandwidth at 0-3 ns less than the pump beam. The oscillator is a doubly resonant cavity which amplifies both the signal and idler waves. While the quoted pump energy damage threshold for the system is quoted at 500 mJ, typical operation uses approximately 290 mJ of 355 nm.

Filter Wheels

Following the output coupler of the OPO, three filter wheels are used to help control the beam energy and wavelength. The first wheel contains several filters used for wavelength selection. Since the versaScan is a doubly resonant cavity amplifying both the signal and idler, spectral filters are required to create a monochromatic beam. Recall that the energy from a 355 nm photon is used. Therefore, a degeneracy occurs at 710 nm where the output wavelengths of the signal and idler are the same. For regions surrounding the degeneracy, the difference between the signal and idler is small and requires a sharp edge filter to select only the desired wavelength. As a result, four separate filters were rotated into the beam path to create a monochromatic beam: (1) a low pass filter with a cutoff at 690 nm, (2) a band pass filter with a range from 695-706 nm, (3) a band pass filter with a range from 703-715 nm, and (4) a long pass filter with a cutoff at 710 nm. The second and third filter wheels contain up to 6 neutral density filters (ND). The second filter wheel has from filters ranging from 0 (blank) - to 5 ND optical thickness for coarse tuning of the beam intensity. The third filter wheel is filled with ND filters ranging from 0.1-.0.6 ND optical thickness for fine tuning of the the beam energy. Intensity tuning is important to prevent detector saturation when the beam is injected into the cavity.

Fibers and Cavity Configuration

After passing through the filter wheels, the beam is gently focused onto a fiber optic using a fused silica lens with a focal length of 75 cm. The fiber has a 200 μm diameter, pure silica core with a fluorine-doped silica cladding. The fiber numerical aperture is listed as 0.22. The outside is covered in a TECS hard fluropolymer. The fiber operates with a spectral range from 250-1200 nm. On one end of the fiber, a standard SMA detector is connected. This end is placed into an X-Y translation mount to facilitate coupling of light into the fiber. The other end is cleaved and optically polished. A one cm long piece of the fluoropolymer coating is removed leaving just the cladding and core.

The cleaved end of the fiber is placed on top of the bottom of the quartz powder cylinder so that the coating free region is exposed to the sample cavity region. If the red fluoropolymer coating is placed in the open cavity, the effective reflectivity of the cavity could diminish due to the coating's absorption. Once the fiber is positioned, the fiber is secured by taping the fiber to the fused silica containing cylinder surrounding the fumed silica cavity (See Chapter 2). The tape is placed such that it does not come in contact with the powder. A separate identical detection fiber is placed 90° offset from the input fiber for sampling of the optical signal. The 90° offset is applied to prevent the input light from directly coupling into the detection fiber. The detection fiber is secured similar to the input fiber.

The top fumed silica cylinder is placed on top of the the bottom cylinder to create a complete cavity. The machined cavity regions are carefully aligned. To ensure the cavity configuration remains the same after opening and closing the cavity, a single piece of electrical tape is placed across the seam between the top and bottom cylinder. Using a sharp blade, the tape is sliced along the cavity seam to re-separate the top and bottom cavity halves. When the cavity is opened to add or remove a sample, the configuration is

restored by aligning the two pieces of tape from the top and bottom cavity (Fig. IX.3).

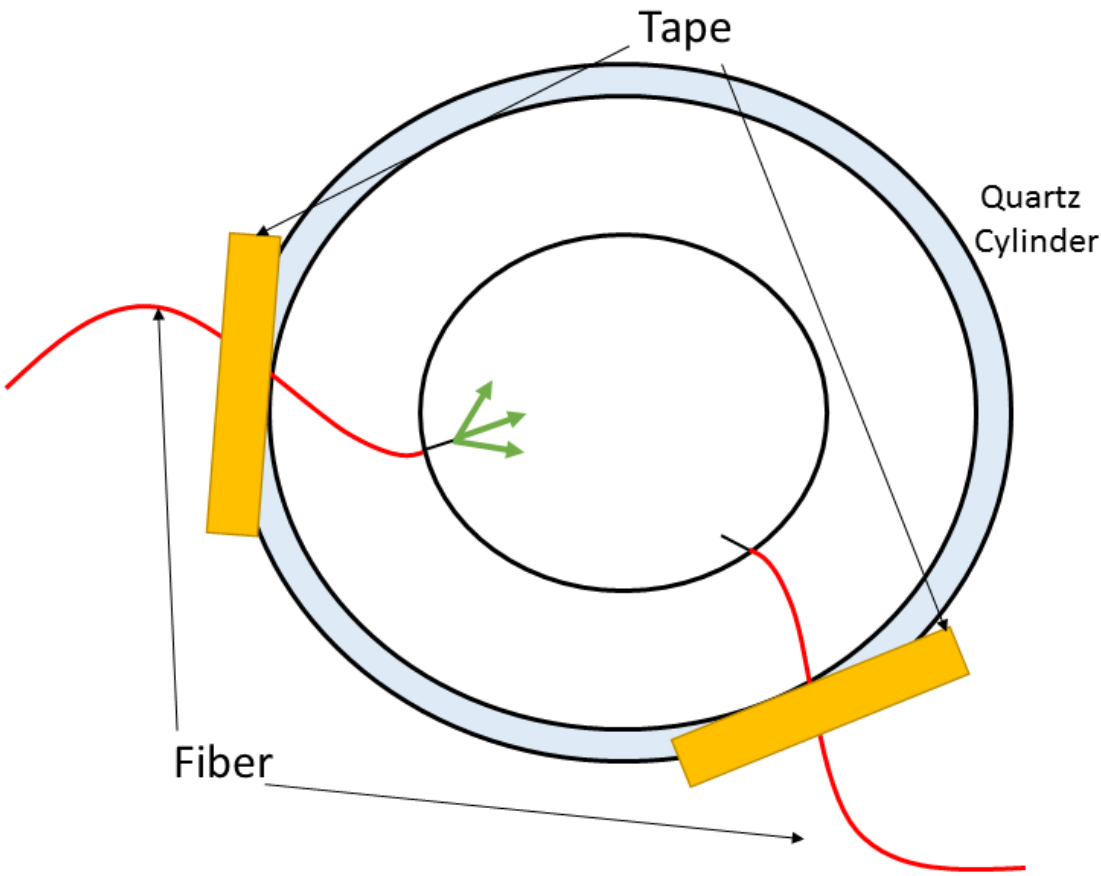

Figure IX.3: A schematic of the the fiber orientation for an ICRDS measurement

Because ICRDS measures the temporal response of an input pulse, shielding from ambient light effects is unnecessary. Effects from room lights will only add a constant offset to the signal. This has no impact of the temporal decay constant. The beam from the OPO, however, is contained completely in beam tubing until it reaches the fiber to prevent stray reflections from the pulse. These stray reflections may have an impact of the decay

constant of the cavity since they occur at the same repetition rate as the input pulse.

Amplified Photodiode Detector and Oscilloscope

The SMA end of the detection fiber is attached to silicon trans-impedance amplified photodetector with a range from 200-1100 nm. A 50 Ω termination was used to achieve a fixed gain of 5kV/A. A silicon detector was chosen because of its bandwidth range, low dark current, high speed, and low cost.

The signal from the photodiode was fed into a Tektronix TDS 2024 with 200 MHz bandwidth and a 2 GS/s sampling rate. The oscilloscope was triggered using a sync signal from the the pump laser. To eliminate shot to shot noise, an average of 512 pulses, the maximum number of averages supported by the oscilloscope, was taken using the oscilloscope's internal averaging algorithm.

Acquisition Software

The averaged decay curve from the oscilloscope was acquired using a single LabView VI. The front panel of the LabView VI is shown in Fig. IX.4. In addition to taking data from the oscilloscope, the program uses a USB port to tune the OPO to the desired wavelength. While the program has the capabilities to take multiple traces from the oscilloscope and average them, the internal averaging function of the oscilloscope was chosen because the GPIB can only send and receive data every 300 milliseconds. This greatly increases the total acquisition time of a measurement. By averaging with the oscilloscope, acquisition time is greatly reduced.

The program scans the OPO over a given wavelength range at a specified step size. At each wavelength, the averaged decay trace is taken and a fit function is applied to the trace. The fit function is a convolution of a Gaussian and an exponential decay. The Gaussian

function is chosen to account for the shape of the input pulse while the exponential decay accounts for the decay of the pulse once it has completely entered the cavity. The fit is applied using an internal Levenberg-Marquardt LabView algorithm.

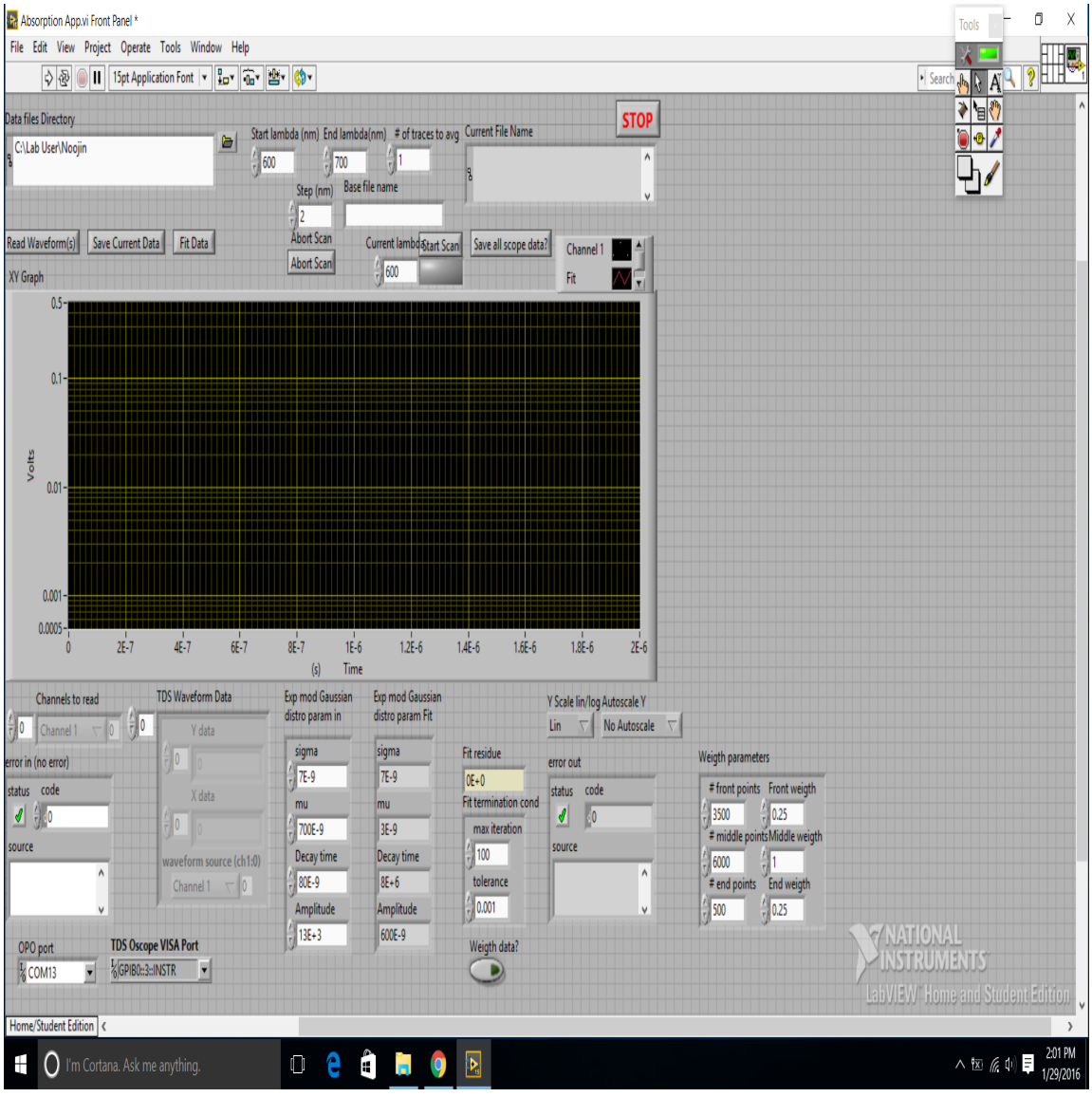

Figure IX.4: The LabView program used to measure the cavity decay constant for ICRDS

In reality, the input pulse is not a perfect Gaussian function which can result in errors

in the fit decay constant. To account for this, a weighting function can be applied so that only the exponential of the tail is fitted. The trace from each average is recorded in a text file and the fitting parameters are saved in another. Once measurements for a particular region are complete, the decay constants for each wavelength are compiled into a single text file. The values for the weight-fitted decay constants were checked against a simple-tail fit algorithm where the first 20 ns of the signal were ignored for fitting and only the exponential decay was fitted. Note that with a pulse length of 10 ns for the input pulse, this eliminates all effects from the initial pulse. The numbers between the two fitting methods agreed to within 1 ns.

CHAPTER X

MEASUREMENT OF THE ABSORPTION COEFFICIENT OF CELLS

The Chinese Hamster Ovary (CHO) (Fig. X.1) family of cell lines is a ubiquitous group of closely related cell lineages which have found use in nearly all subfields of biomedical research. Derived by T. T. Puck in 1957, CHO cells are uniquely suited to meet a wide range of research demands [69, 47, 72]. Given their low chromosome number (2n=22 or 11 chromosome pairs), lack of an epidermal growth factor receptor (EGFR), rapid doubling time and high rate of protein production, CHO cells are widely used as transfection targets, in fluorescence and scattering spectroscopy, and in recombinant protein manufacturing [59]. CHO-K1, a subclone of the original CHO lineage is one of the most commonly used cell types in biomedical research worldwide.

In recent years, in-vitro cell monolayers have proven particularly useful in the development of optical diagnostic and research tools. Techniques such as Light Scattering Spectroscopy (LSS) [8, 4] and angle-resolved Low Coherence Interferometry (a/LCI) [80, 37] are often first tested using cells plated on cover glass. The empirical results from such experiments are examined against Monte Carlo or Mie Theory simulations of photon propagation within biological matter, with results determined by correlation with the theoretical model. To ensure accurate measurements, precise knowledge of the optical properties of the cells of interest are of extreme importance. Unfortunately, biological samples have a large scattering cross section compared to their absorption cross section [35, 57, 13]. Hence, many traditional absorption measurements tend to overestimate the contributions. Prahl's Inverse Adding Doubling (IAD) attempts to characterize highly scattering media by entering the results from observed transmission and reflection experiments in a Monte Carlo Simulation. However, Monte-Carlo simulations do not produce exact values but a

Figure X.1: A bright field image of CHO-K1 Cells taken using a confocal microscope (Carl Zeiss LSM 710, Oberkochen,Germany.

statistical estimate whose accuracy is dependent upon the number of samples, which can increase computing time. A direct measurement eliminates the need for computation and requires no statistical estimation. Here, we present the first direct measurement of the absorption and scattering coefficients of CHO-K1 cells.

Materials and Methods

Scattering

The scattering coefficient, μ_s, was obtained by placing a homogeneous suspension of CHO-K1 cells into an Agilent Cary 6000i spectrophotometer. The spectrophotometer measures the extinction coefficient, $\mu = (\mu_a + \mu_s)$, for a given sample. If $\mu_a >> \mu_s$, the spectrophotometer would serve as a sufficient measure of the absorption coefficient. Using

the absorption measurement made with ICRDS, the scattering coefficient can be obtained by

$$\mu_s = \mu - \mu_a. \tag{X.1}$$

Cabrera et al. demonstrated success in finding the scattering coefficient using this technique with a titanium dioxide particle suspension [11]. In the spectrophotometer, our sample was placed as far as possible from the detector to minimize forward-scattered light from reaching the detector.

Cell Preparation

Chinese hamster ovary K1 cells, CHO-K1 cells (ATCC® CCL-61™) were obtained from the American Type Culture Collection [ATCC], Manassas, VA). Cultures were established and maintained according to standard protocols provided by ATCC. Briefly, cells were grown and maintained using a complete medium composed of F-12K Medium supplemented with 10% fetal bovine serum (ATCC® 30-2020™), and $1\frac{I.U.}{mL}$ Penicillin and $0.1\frac{\mu g}{mL}$ Streptomycin Antibiotic (ATCC® 30-2300). When the culture reaches maturity, the growth medium was removed from the six 75 cm^2 culture flasks, and each flask was rinsed with 10mL phosphate buffered saline (PBS) (Corning-MediaTech, Corning, NY). Cell monolayers were then treated with 2mL trypsin-EDTA (ATCC® 30-2101™) per flask and incubated at $37°$C in 5% CO_2 for 5 minutes. After incubation, 2mL of the complete medium was added to each flask to deactivate the trypsin. The solution was then aseptically removed from each flask, combined with the 4mL cell suspensions from the other flasks, and split into two 15mL conical centrifuge tubes (3 flasks, 12 mL total volume/tube). From each tube, duplicate cell counts were accomplished via the trypan blue exclusion method, using 15μL each of cells and trypan blue (0.4% solution in PBS) with

an Invitrogen Countess automated cell counter/hemocytometer (Eugene, OR). Cell counts were averaged, and then multiplied by the total volume to obtain an accurate total cell count for the experiment.

Next, cells were pelleted using a centrifuge (Thermo IEC Centra CL3R, Thermo Fisher Scientific Inc. Waltham, MA) at 650 relative centrifugal force (RCF) for 10 minutes. Following centrifugation, the supernatant was removed aseptically, and the pellet was washed by resuspension in a buffer solution, comprised of 2mM $MgCl_2$, 5mM KCl, 10mM HEPES, 10mM glucose, 0.2mM $CaCl_2$, and 135mM NaCl in deionized water. After washing, the cells were again pelleted at 650 RCF for 10 minutes, and the supernatant was again aseptically removed. This pellet was then resuspended in a volume of buffer appropriate for the intended experiment; 1mL for the ICRDS measurement and $\sim$ 3mL for the spectrophotometer transmission measurement. Given the short pathlength associated with the spectrophotometer ($\approx$ 1 cm), we assume the effects from scattering and absorption from the buffer are negligible. All measurements were taken within 30 minutes of final resuspension, and all spectra were normalized to the cell count obtained for that experiment.

Results and Discussion

Three measurements of the cell absorption coefficients were taken with cell counts of 80 million, 81.8 million, and 73.1 million. The raw decay constants for the ICRDS measurements of each of the outside buffer, the cell-buffer mixture, and the two dilutions of Irgalan Black are shown in Fig. X.2.

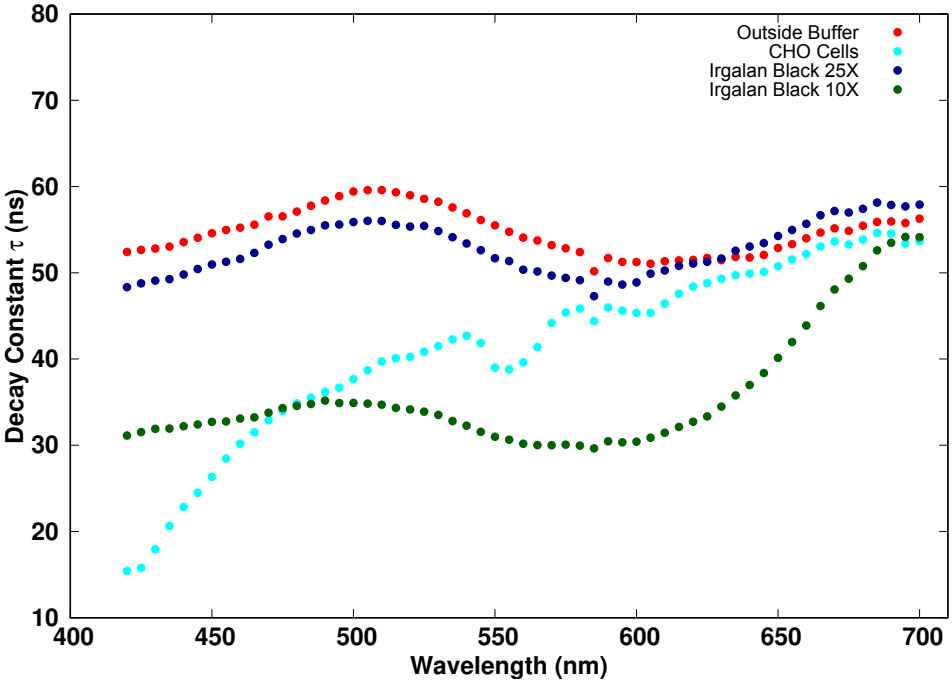

Figure X.2: The decay constant curves for each sample that makes up the ICRDS for CHO Cells; that is, (1) the outside buffer, (2) the buffer-cell mixture, (3) a 25X dilution of Irgalan Black, and (4) a 10X dilution of Irgalan Black

Fig. X.3 shows the average absorption coefficient of a CHO-K1 cell plotted with the average absorption coefficient of an unpigmented retinal pigmented epithelial cells obtained by Cone et. al. (RPE) [16]. The numerical values of the average absorption coefficient of a CHO cell is shown with the absorption coefficient value of an RPE cell in Table X.1.

Table X.1: The Average Absorption Coefficient Values of a Live CHO-K1 Cell, α_{CHO} and a Live RPE Cell, α_{RPE} Measured Using ICRDS

λ (nm)	α_{CHO} (cm^{-1})	α_{RPE} (cm^{-1})	λ (nm)	α_{CHO} (cm^{-1})	α_{RPE} (cm^{-1})
420	$3.39E-09$	$1.13E-08$	530	$6.28E-10$	$2.37E-09$
425	$3.21E-09$	$9.32E-09$	535	$5.74E-10$	$2.49E-09$
430	$2.70E-09$	$9.26E-09$	540	$5.47E-10$	$2.74E-09$
435	$2.14E-09$	$7.88E-09$	545	$5.61E-10$	$2.57E-09$
440	$1.80E-09$	$7.50E-09$	550	$7.09E-10$	$2.41E-09$
445	$1.59E-09$	$7.00E-09$	555	$6.91E-10$	$2.00E-09$
450	$1.40E-09$	$6.26E-09$	560	$6.21E-10$	$1.57E-09$
455	$1.20E-09$	$5.63E-09$	565	$5.29E-10$	$1.37E-09$
460	$1.07E-09$	$5.07E-09$	570	$3.88E-10$	$1.23E-09$
465	$1.00E-09$	$4.57E-09$	575	$3.31E-10$	$1.17E-09$
470	$9.20E-10$	$4.38E-09$	580	$3.01E-10$	$1.14E-09$
475	$8.82E-10$	$4.00E-09$	585	$2.99E-10$	$1.20E-09$
480	$8.25E-09$	$3.85E-09$	590	$2.82E-10$	$1.22E-09$
485	$8.01E-09$	$3.68E-09$	595	$2.82E-10$	$1.21E-09$
490	$7.78E-09$	$3.56E-09$	600	$2.90E-10$	$1.05E-09$
495	$7.49E-09$	$3.40E-09$	605	$2.70E-10$	$9.01E-10$
500	$7.20E-09$	$3.15E-09$	610	$2.43E-10$	$7.88E-10$
505	$6.74E-09$	$3.00E-09$	615	$1.97E-10$	$7.84E-10$
510	$6.56E-09$	$2.83E-09$	620	$1.77E-10$	$7.35E-10$
515	$6.40E-09$	$2.85E-09$	625	$1.67E-10$	
520	$6.71E-09$	$2.56E-09$	630	$1.58E-10$	
525	$6.43E-10$	$2.47E-09$	635	$1.50E-10$	
640	$1.42E-10$	$2.37E-09$			
645	$1.32E-10$	$2.49E-09$			
650	$1.24E-10$	$2.74E-09$			
655	$1.11E-10$	$2.57E-09$			
660	$1.06E-10$	$2.41E-09$			
665	$9.97E-11$	$2.00E-09$			
670	$9.02E-11$	$1.57E-09$			
675	$8.04E-11$	$1.37E-09$			
680	$6.97E-11$	$1.23E-09$			
685	$5.57E-11$	$1.17E-09$			
690	$4.58E-11$	$1.14E-09$			
695	$2.58E-11$	$1.20E-09$			

Notice that while the overall values for two different lines of epithelial cells are different, the structure of the absorption spectra are nearly identical. Fig 4 shows a comparison between the average absorption coefficient per cell and the average scattering coefficient per CHO-K1 cell. Measurements were made at 5 nm steps from $420 - 700$ nm to optimize spectral resolution while maintaining cell viability. Due to a lack of cavity mode structure, the resolution of ICRDS is limited only by the spectral resolution of the source and detector. However, pulses with wavelength below 420 nm were indistinguishable from noise. Also, the reflectivity of the fumed silica cavity decreases significantly for longer wavelengths. This feature, coupled with the diminished absorption coefficient for longer wavelengths, inhibits absorption coefficient measurements into the near-infrared (NIR).

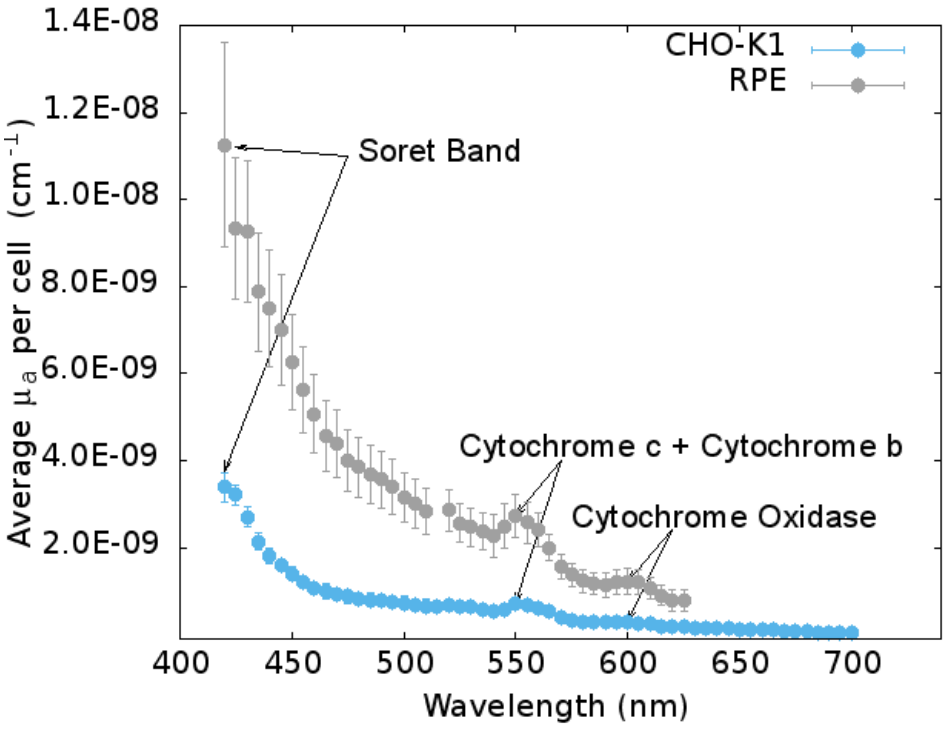

Figure X.3: The average absorption coefficient of a single CHO-K1 cell from $420 - 700$ nm compared with the absorption coefficient of RPE Cells obtained from Cone et. al. [16]

The peaks in Fig. X.3 at 420 nm, 550 nm and 605 are consistent with predictions from the literature. These structures are consistent with the well-known Soret band discovered in 1883. The Soret band arises from electron dipole movement within porphyrin ligand involving $\pi - \pi*$ transitions [71]. The intense peak band at about 420 nm is attributed to a transition from the ground state to the second excited state ($S_0 \rightarrow S_2$) (B band) while the smaller features are associated with a weak transition between the ground state and the first excited state ($S_0 \rightarrow S_1$) (Q Bands) [29].

One of the most well-known, naturally-occuring porphyrins is heme. Heme is most recognized for the role it plays as co-factor for hemoglobin but is also important in other hemoproteins such as cytochromes. Here, mitochondrial cytochrome is most likely the dominant absorber. Lance and Bonner [44] showed that the α-band of cytochrome oxidase (cytochrome a + cytochrome a_s) is located at 605 nm while the α-band of cytochrome c appears at $550nm$ with a shoulder at 560 nm corresponding to cytochrome b. Furthermore, the absorption in the Soret region is dominated by absorption from cytochrome b and cytochrome oxidase. Typically, cytochrome oxidase would appear as a shoulder in the Soret band but the error associated with measurements in that regime limit our ability to resolve fine structure.

The scattering coefficient was calculated by subtracting the absorption values obtained through the ICRDS measurement from the extinction values obtained through the spectrophotometer measurements. The scattering measurement was taken with a cell count of 68 million cells. The scattering coefficient was plotted with the absorption coefficient to demonstrate the impact of scattering on the extinction coefficient. As shown in Fig. X.4, the scattering coefficient varies from more than an order of magnitude to more than 3 orders of magnitude larger than the absorption coefficient, demonstrating the difficulty of deriving precise parameters from scatter-sensitive techniques and showing the superior capabilities of ICRDS in this regard. The scattering coefficient of the CHO cells is consis-

tent with Mie Theory. This is not surprising since the size of an average CHO cell (20μm) is much larger than the photon wavelengths in this study.

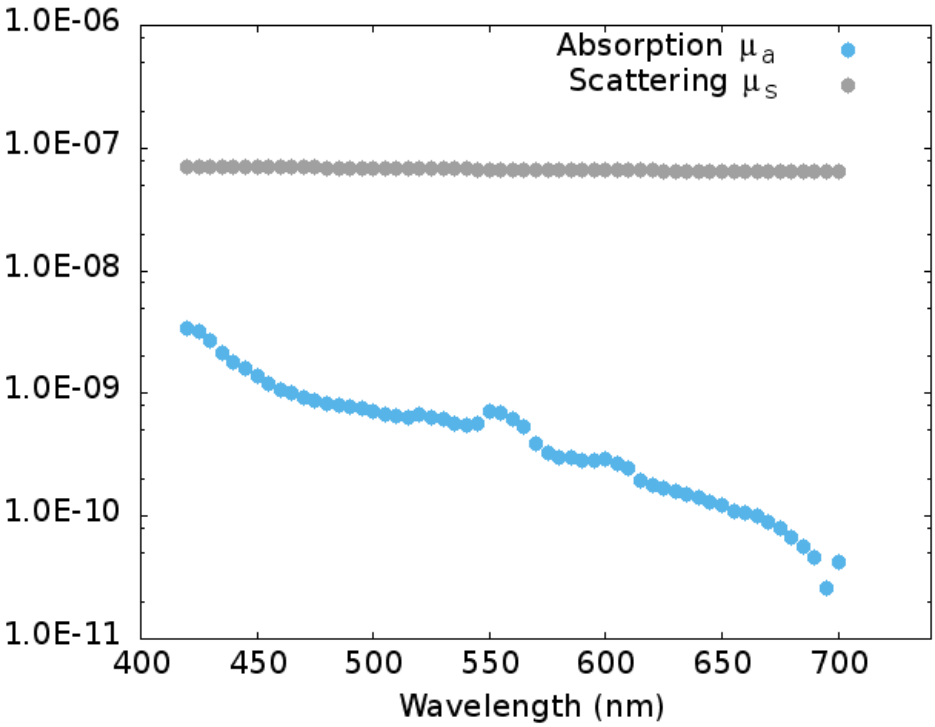

Figure X.4: The average scattering coefficient plotted with the average absorption coefficient for a single CHO-K1 cell from $420 - 700$ nm.

Conclusion

We have directly measured and characterized the absorption and scattering coefficients for CHO-K1 epithelial cells. The extinction coefficient, a sum of the absorption and scattering coefficients, is dominated by scattering events. Furthermore, we demonstrated that the CHO-K1 spectrum has features that are consistent with literature absorption values for heme groups, a component of cytochromes in the mitochondria corresponding to the electron transport chain.

CHAPTER XI

INTEGRATING CAVITY RING-DOWN SPECTROSCOPY FOR SOLID SAMPLES

Motivation

The invention of lasers has had significant implications for medical diagnostics and therapeutics. Lasers provide a source of energy that can be delivered non-invasively to a target sight. However, cells and tissue damage easily to exposure of high intensity laser radiation. When light incident on a biological sample is absorbed, some of the absorbed energy is transformed into thermal energy which heats the sample. If the sample temperature increases too much, the high temperature denatures the DNA and permanently damages the sample. The threshold intensity at which permanent damage occurs is a function of the absorption coefficient of the sample. Therefore, the threshold intensity will vary depending on the wavelength of the laser. In addition, the previous section also introduces ICRDS as an alternative to IAD where the demonstrated use of ICRDS to accurately measure the absorption coefficient of cells has been discussed. Unfortunately, the technique described in section 9 is only valid for samples that can be reduced to a series identical subdivisions such as cells. Under the assumption that each cell absorbs approximately the same amount of light energy, the absorption coefficient can be normalized by dividing by the total number of cells in the sample. The resulting number is equivalent to the average absorption coefficient per cell and is independent of the sample volume. However, since tissue samples are networks of cells, it is difficult to separate the sample into individual units. Therefore, the ICRDS procedure used for the cells would yield an absorption coefficient for the sample which would be dependent on the sample volume.

In addition, cells can be dissolved in a hospitable storage buffer because of their small

size. Because the cell sample is mostly liquid, a dye solution with the same volume can be used since it mimics the same geometry of the original sample with respect to the cavity. When trying to measure solid samples with ICRDS, a volume of dye that is identical to the sample can be selected, but it may have different geometrical orientation with respect to the cavity. As a result, absorption coefficients calculated using this method may deviate greatly from the true values. Hence, an alternative method needed to be derived. We will derive a method that requires no calibrating dye and compare it with results from IAD.

Introduction to Inverse-Adding-Doubling

IAD uses the results of three reflection measurements and six transmission measurements (three for the total transmission and three for unscattered transmission) as parameters for a Monte Carlo simulation to find the scattering, absorption, and anisotropy. The measurements for the total reflectance and total transmission are shown in Fig. XI.1. A total reflectance coefficient, M_R is acquired by collecting the reflection from the sample, $R(r_s^{direct}, r_s)$, as well as from a known reflectance standard, $R(r_{std}, r_{std})$, with an integrating sphere and measuring the irradiance on the cavity wall. A third measurement measures the direct transmission through the integrating sphere to eliminate background effects for the integrating sphere ($R(0,0)$) and establish a baseline signal. A pictorial representation of the reflectance measurements is shown on the left side of Fig. XI.1. The total reflectance coefficient is calculated by

$$M_r = r_{std} \cdot \frac{R(r_s^{direct}, r_s) - R(0,0)}{R(r_{std}, r_{std}) - R(0,0)} \tag{XI.1}$$

where r_{std} is the reflectivity of the reflectance standard.

The total transmittance coefficient, M_T, is calculated by measuring the unimpeded light coupled directly into the integrating cavity ($T(0,0)$), the light transmitted through the

sample into the integrating cavity ($T(r_s^{direct}, r_s), r_s)$), and the signal from the integrating cavity when the light is blocked (T_{dark}). The measured total transmittance is calculated from

$$M_T = \frac{T(r_s^{direct}, r_s) - T_{dark}}{T(0,0) - T_{dark}} \tag{XI.2}$$

The configuration of these measurements are shown pictorially on the right side of Fig. XI.1.

Finally, the coefficient for the measured unscattered transmittance, (M_U), is measured using the experimental configurations in Fig. XI.2. A broadband source is used to illuminate a sample while a detector measures the light that passes through the sample. An iris is used to limit the field of view of the detector such that only light that is unscattered makes it to the detector (U_s). (Note, light scattered at angles near 0° will still be measured but their contribution is assumed to be negligible if the aperture is kept small and the detector is located far from the detector.) A second identical measurement is made but this time the aperture is completely closed (U_0). This second measurement is performed to eliminate contributions from ambient light and background noise. A third measurement is performed with the aperture opened (the aperture size is the same as the first measurement) but the sample has been removed. The third measurement normalizes the measurement to the output of the source. M_u is calculated by

$$M_u = \frac{U_s - U_0}{U_{100} - U_0}. \tag{XI.3}$$

Prahl specifically notes that the measured unscattered transmittance is often "underestimated and difficult to get right" [57]. Error from any of these measurements can corrupt the Monte Carlo simulation to provide undetectable inaccuracies in the final results. Prahl notes that the old adage "garbage in, garbage out" aptly applies to IAD. As a result, an

independent measurement of even one of the optical properties found in IAD serves to validate the results of the Monte Carlo simulation. We will use ICRDS to verify the validity of Prahl's inverse adding-doubling technique by measuring the absorption coefficient of biological tissue.

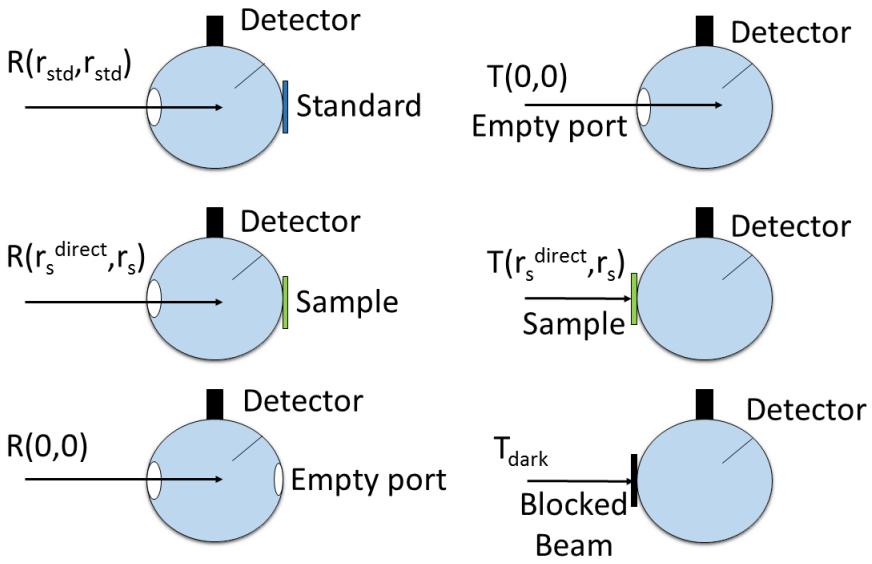

Figure XI.1: The experimental setup for the reflectance and transmission measurements for IAD

Theoretical Background for ICRDS

As described in the above cell section, a new measurement technique is needed to find the absorption coefficient of tissue that is volume independent. In an ideal experiment, the characteristic ring-down constants of the decay curve from an empty cavity and a cavity filled with the desired sample would be measured. Since the integrating cavity provides a uniform, isotropic illumination, the average distance $\bar{d}$ that light travels between reflections from the cavity wall in a cylindrical cavity with a diameter D and height H is

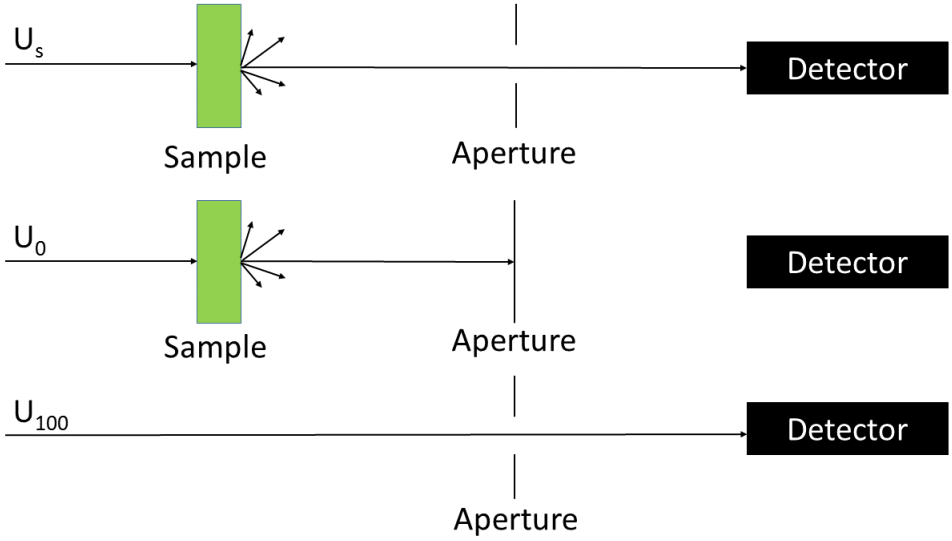

Figure XI.2: The experimental setup for the direct transmission (0°) measurements for IAD

$$\bar{d} = \frac{2DH}{2H + D} \tag{XI.4}$$

regardless of whether the cavity is filled or empty. If the cavity is only partially filled, then $\bar{d}$ for the sample volume is a function of the volume. Since the cavity produces a uniform, isotropic field, the decay constant of the cavity decreases linearly with increasing volume increments. Therefore, the decay constant τ_{Vol} for an arbitrary sample volume is

$$\tau_{vol} = lV_{sample} + \tau_{EC} \tag{XI.5}$$

where l is the change in the cavity decay constant per unit of volume. A similar relationship for the inverse decay time can be found, namely

$$\tau_{vol}^{-1} = mV_{sample}^{-1} + \tau_{EC}^{-1} \tag{XI.6}$$

where V_{sample} is the sample volume, τ_{EC} is the decay constant for the empty cavity, and m is the change in the inverse of the cavity decay constant per unit volume. If we measure the rate of change of the cavity decay constant with respect to the sample volume, we find

$$\frac{\partial \tau_{vol}}{\partial V_{Sample}} = m \tag{XI.7}$$

As a result of Eq. XI.6, the inverse decay constant for an arbitrary sample volume can be determined by measuring the decay constant of the empty cavity as well as the decay constant of several different volumes of a sample. If we choose $V_{sample} = V_{cavity}$, then decay constant for a cavity that is completely filled with sample can be found. Due to the difficulties described in the introduction for calibrating ICRDS measurements of solid samples, the full cavity decay constant can be used to find the sample absorption coefficient without a dye calibration.

Recall the expression for the decay constant of a cavity filled with a sample is (from Chapter 8)

$$\tau_s = \frac{1}{-\ln \rho + \alpha_s \bar{d}_s}(\frac{\bar{d}_s}{c_s} + \delta t). \tag{XI.8}$$

It has been shown by Cone et. al. that $\delta t << \frac{\bar{d}}{c}$ so Eq. XI.8 becomes

$$\tau_s \approx \frac{1}{-\ln \rho + \alpha_s \bar{d}_s}\frac{\bar{d}_s}{c_s} \tag{XI.9}$$

where d_s describes the average distance that light travels through the sample between reflections from the cavity wall and $c_s = \frac{c}{n}$ where n is the index of refraction of the material filling the sample volume. Similarly, the expression for an empty cavity is given by

$$\tau_{EC} = \frac{1}{-\ln \rho} \frac{d}{c} \tag{XI.10}$$

By rewriting Eq. XI.9 in terms of the inverse of Eq. XI.10, the expression becomes

$$\tau_s = \frac{1}{\frac{\bar{d}}{c}\tau_{EC}^{-1} + \alpha d_s} \frac{\bar{d}_s}{c_s}. \tag{XI.11}$$

Since an integrating cavity provides a uniform and isotropic distribution of radiation, $d = d_s$ for a full cavity. The above equation simplifies under these conditions to

$$\tau_s = \frac{1}{\tau_{EC}^{-1} + \alpha c} (\frac{c}{c_s}) \tag{XI.12}$$

or more simply

$$\tau_s = \frac{n}{\tau_{EC}^{-1} + \alpha c}. \tag{XI.13}$$

Solving for α, the expression is just

$$\alpha = \frac{n\tau_s^{-1} - \tau_{EC}^{-1}}{c}. \tag{XI.14}$$

Notice that this result differs from previous ICRDS derivations in that it does not require any calibrations.

Optical Absorption Coefficient of Synthetic Tissue

We will compare the optical absorption coefficient of synthetic skin tissue measured using IAD with the absorption coefficient of the same sample measured with ICRDS. The synthetic skin was a commercial product manufactured by SynDaver Labs called SynTissue. The SynTissue samples contain the same tensile modulus, abrasion resistance,

penetration force, coefficient of friction, thermal conductivity, dielectric constant, etc. as live skin tissue. As a result, the synthetic tissue is a perfect substitution for live tissue in experimental tests, especially in situations where tissue damage is likely. SynDaver has yet to characterize the optical properties of the synthetic tissue. Therefore, the synthetic skin was tested for its viability as a substitute for live tissue in optics based experiments. The absorption coefficient was measured using IAD and ICRDS using XI.14. ICRDS measurements were performed by incrementally adding a 1 mm by 1 mm by 1 mm pieces of synthetic skin to the cavity and measuring the cavity decay constant. These values were fitted using a linear regression to find the slope. The slope was then used to find the theoretical full cavity inverse decay constant. The results are shown in Fig. XI.5. The skin was pigmented to resemble Caucasian skin.

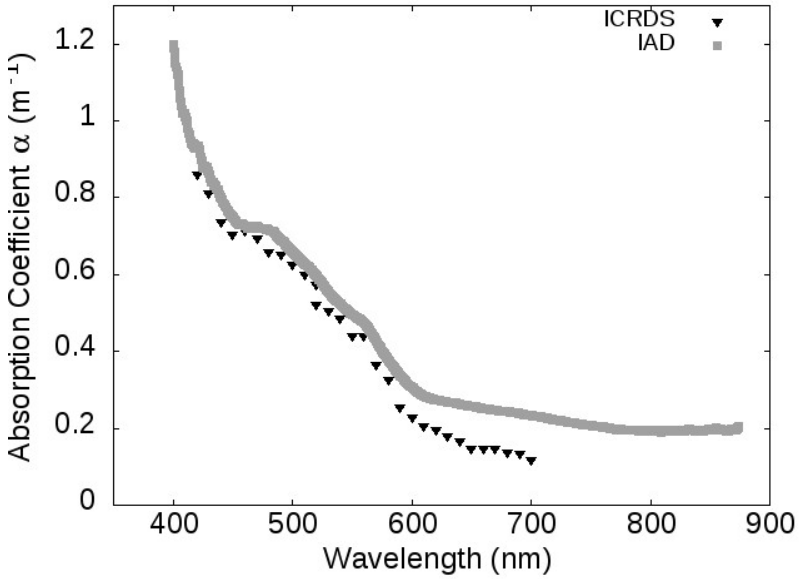

Figure XI.3: A comparison of the absorption coefficient of synthetic tissue measured using both ICRDS and IAD.

Acquisition of Swine Brain Tissue

ICRDS was also used to measure the absorption coefficient of tissue from the brain of a pig. This tissue was acquired under tissue sharing protocols with the Triservice Research Laboratory in San Antonio, Texas. The tissue was placed in a sucrose-rich storage buffer to minimize cell death. In addition to the brain, several pieces of the dura were removed for measurement and also placed in the buffer. The tissue is placed in a cutting buffer and a portion of the frontal lobe is removed. The remaining portion of the tissue is placed in a liquid formalin solution for long term use. Once in the cutting buffer, the visible arteries are removed. It is worth noting that the tissue is filled with many tiny capillaries which cannot be removed by hand. Once the large arteries are removed, the a 1 cm x 1 cm x 1 cm cube is cut and mounted to a chilled microtome cutting block using super glue.

A microtome is a machine designed to cut micron-sized slices of tissue accurately and consistently. While many different microtomes exist, the brain tissue for this study was cut using a vibrating microtome. The vibrating microtome uses a vibrating cutting blade (a razor blade) which allows for a cut to be made with less pressure than with a stationary blade. The cut thickness for a vibrating microtome is usually between 30-500 μm for live tissues and 10-500 μm for fixed tissue.

The mounted tissue is placed under the microtome blade. First, an initial cut is made that removes the top layer of the tissue and creates a smooth surface for cutting of the samples. Removing the top layer also ensures that the cutting surface of the blade is flush with the surface of the tissue. Following the initial cut, three 300 μm cuts are made resulting in three samples that are 1 cm x 1 cm x 300 μm. The samples are thinly cut so that the sample is completely illuminated during measurement. The samples are placed in a crucible with 1 mL of storage buffer and placed in the cavity for measurement.

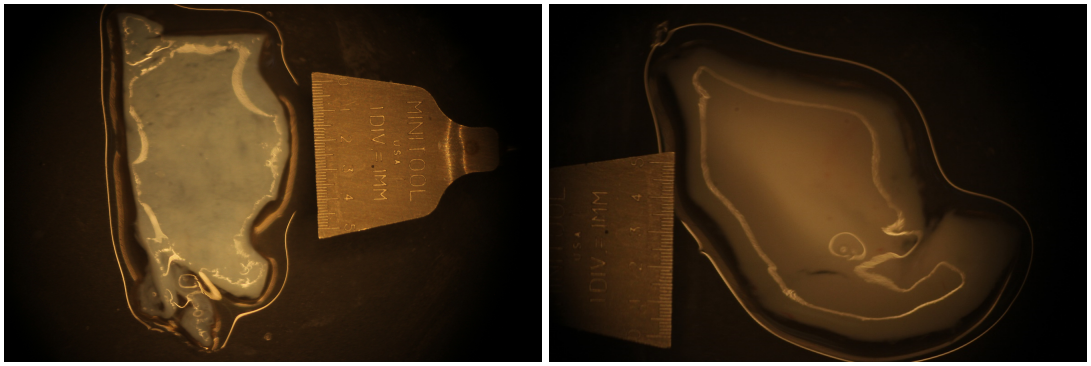

Figure XI.4: A sample image of a section of the dura mater (left) and frontal lobe (right) of a pig brain used in ICRDS

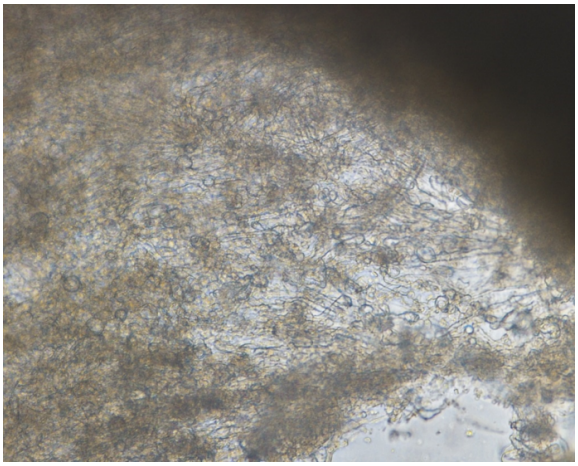

Figure XI.5: A confocal microscope image of the neural network of a pig brain

Results of Living Tissue compared with Formalin Tissue

Since the tissue was placed in a buffer solution the live tissue was measured using the ICRDS protocol described in Eq. 8.14. The results are shown in Fig. XI.6. The peaks located at 425 nm, 525 nm, and 550 nm are consistent with literature values of absorp-

tion from Heme structures, specifically Hemoglobin. Hemoglobin exists in two states: oxygenated and deoxygenated. Oxygenated hemoglobin has absorption peaks at approximately 540 nm and 580 nm while deoxygenated hemoglobin has a peak at approximately 550 nm. Comparing the results of this study with the literature, the measured brain tissue appears to be composed of mostly deoxygenated hemoglobin.

Furthermore, it is difficult to tell if the absorption peak at 420 nm is due to the absorption from the Soret band of the pig tissue or absorption from Hemoglobin in the blood capillaries. Both the Soret band and Hemoglobin have a strong absorption peak at 420 nm. This is most likely caused by hemoglobin, which is composed of heme porphyrin. Porphyrin is well known to have strong absorption in the blue and ultraviolet.

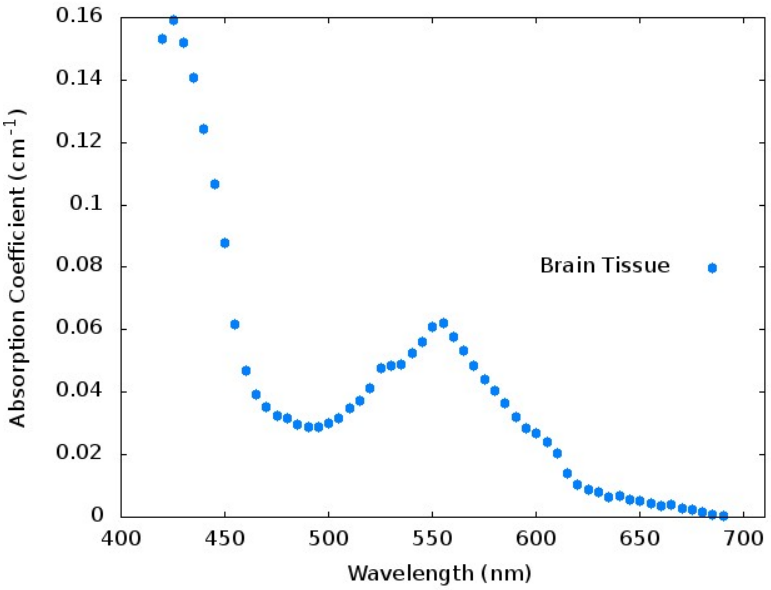

Figure XI.6: Absorption spectrum of a sample of the frontal lobe of a pig brain from 420-690 nm.

After one month, the brain tissue was removed from the formalin. The formalin creates

covalent chemical bonds between proteins in the tissue. This creates rigidity to the tissue and prevents it from decomposing. The fixed tissue was sectioned using the microtome into three 1 cm x 1 cm x 1 μm pieces. These pieces were placed in a crucible with 1 mL of Formalin and measured using ICRDS. The results are compared with the live tissue in Fig. XI.7.

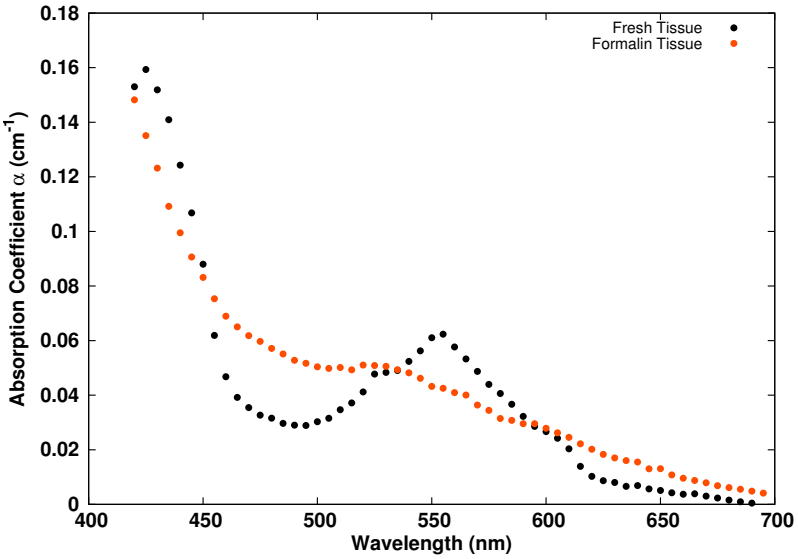

Figure XI.7: A cross section view of the ICAM-II.

The formalin spectrum in Fig. XI.7 has two noticeable differences from the live tissue spectrum. First, the large peak at 425 nm appears to have been blue shifted resulting in a new peak at a wavelength less than 420 nm. Unfortunately, the OPO used in this study was unable to produce wavelengths less than 420 nm. Therefore, this study was unable to determine the exact location of this peak. Furthermore, the strong Hemoglobin absorption peak located at 550 nm in the live tissue disappears for the fixed tissue. This may be caused by a chemical reaction between the hemoglobin and the fixing agent (formalin). The values for the absorption spectra of both samples is found in Table XI.1.

Table XI.1: The Absorption Coefficient Values of Live Brain Tissue, α_{LT} and Fixed Brain Tissue, α_{FT} Measured Using ICRDS

λ (nm)	α_{LT} (cm^{-1})	α_{FT} (cm^{-1})	λ (nm)	α_{LT} (cm^{-1})	α_{FT} (cm^{-1})
420	0.1530	0.1482	560	0.0577	0.0409
425	0.1593	0.1351	565	0.0533	0.0401
430	0.1518	0.1232	570	0.0487	0.0482
435	0.1409	0.1092	575	0.0439	0.0364
440	0.1242	0.0995	580	0.0406	0.0344
445	0.1068	0.0906	585	0.0367	0.0314
450	0.0880	0.0832	590	0.0323	0.0307
455	0.0619	0.0753	595	0.0286	0.0295
460	0.0467	0.0689	600	0.0267	0.0295
465	0.0392	0.0650	605	0.0242	0.0279
470	0.0355	0.0618	610	0.0204	0.0262
475	0.0327	0.0597	615	0.0139	0.0245
480	0.0316	0.0571	620	0.0102	0.0222
485	0.0296	0.0551	625	0.0087	0.0202
490	0.0290	0.0528	630	0.0080	0.0183
495	0.0289	0.0517	635	0.0066	0.0170
500	0.0303	0.0504	640	0.0069	0.0155
505	0.0316	0.0498	645	0.0057	0.0130
510	0.0347	0.0502	650	0.0051	0.0131
515	0.0372	0.0493	655	0.0042	0.0108
520	0.0412	0.0510	660	0.0037	0.0096
525	0.0477	0.0509	665	0.0039	0.0088
530	0.0483	0.0506	670	0.0030	0.0079
535	0.0490	0.0493	675	0.0023	0.0068
540	0.0524	0.0482	680	0.0015	0.0061
545	0.0562	0.0462	685	0.0009	0.0056
550	0.0610	0.0432	690	0.0005	0.0048
555	0.0623	0.0425			

CHAPTER XII

A ROBUST COMMERCIAL DIFFUSE REFLECTOR

Since the compressed fumed silica is fragile and susceptible to contamination, the potential applications of integrating cavities made from this material could be limited. As a result, a new solid white quartz (Heraeus Quartz HOD-300 ™) manufactured by Heraeus© was explored as a suitable alternative. The diffusive light reflecting nature of white quartz has been previously demonstrated by the work of Heath and Georgiev [30]. White quartz, which is manufactured by generating air pockets in a piece of solid quartz, uses the same reflections at quartz-air interfaces to create a robust diffuse reflector in the UV-VIS-NIR spectrum.

Experimental Test of White Quartz

The reflectivity of white quartz was tested using ICRDS. [17, 16] ICRDS differs from the well-known cavity ring down spectroscopy by injecting a temporally short ($\sim$ 6 ns) pulse into an integrating cavity rather than into a two mirror cavity. [3, 32, 53, 82] In ICRDS, if the diffuse reflectivity of the cavity wall is high, then at each bounce from the cavity wall, a very small portion of the light is lost. Over time, the amount of light in the cavity will exponentially decay or "ring down". Fig. XII.1 provides a comparison of simulated ring-down decay curves for a cavity of white quartz (diffuse reflectivity 99.4%) and for a cavity of Spectralon SRS-99 (diffuse reflectivity 99.3%). The latter is the highest quoted reflectivity for a Spectralon product in the UV-VIS regime [6, 41].

Part of the data reported in this chapter is reprinted with permission from "Robust commercial diffuse reflector for UV-VIS-NIR applications" by John D. Mason, Michael T. Cone, Matthew Donelon, Jeffery C. Wigle, Gary D. Noojin and Edward S. Fry, 2015 *Applied Optics*, Vol. 54, Issue 25, pp. 7542-7545.© 2016 Optical Society of America.

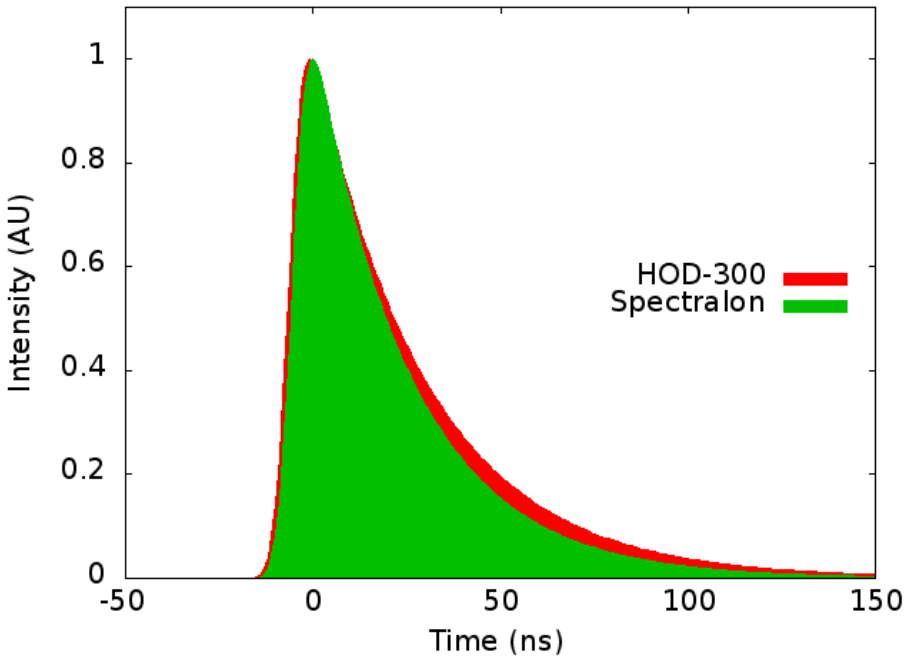

Figure XII.1: The simulated temporal decay curve of an injected pulse in a Spectralon cavity and in an HOD-300 cavity with the same dimensions (cylindrical, D=10.16 cm, H=5.72 cm) for a 6-ns pulse.

The decay constant τ for the optical energy in a cavity is obtained by fitting the decay curve with the convolution of a Gaussian and exponential. The dimensions of the cylindrical cavity used for Fig. XII.1 were $D = 10.16$ cm and $H = 5.72$ cm resulting in an average distance between reflections in the cavity of $\bar{d} = 5.39$ cm. Thus, the reflectivity ρ of a cavity wall is obtained from a measurement of the decay constant τ and the cavity dimensions.

Experimental Data

A cavity was formed using three round discs of HOD-300 quartz as shown in Fig. XII.2. The discs were 27.94 cm diameter and 5.72 cm thick, and one disk had a 10.16 cm

diameter hole in the center. A cylindrical cavity (10.16 cm diameter and 5.72 cm high) was formed by stacking the three discs with the piece containing the hole in the middle.

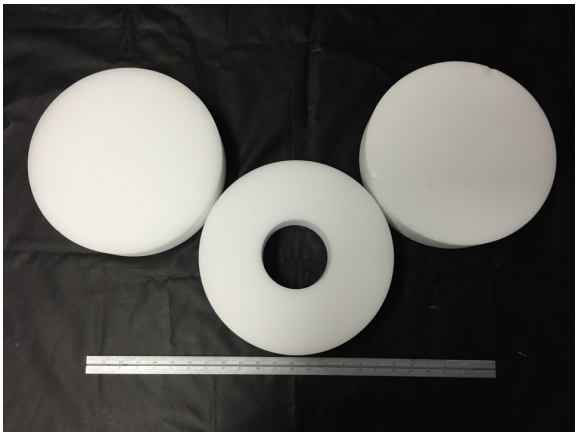

Figure XII.2: Three HOD-300 discs that create a cavity of opaque quartz

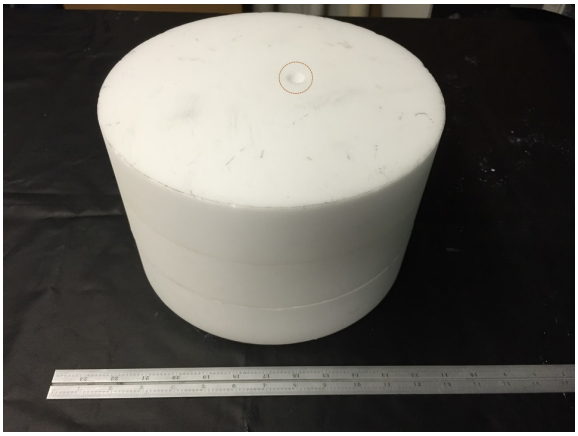

Figure XII.3: The stacked configuration of a White Quartz cavity. A red circle has been drawn to show the hole drilled for fiber coupling.

On one face of the top and bottom discs, there is a 1.27 cm diameter hole 3.18-cm deep

with a 0.127 cm hole at its center drilled the rest of the way through the disc (as shown in Fig. XII.3). This hole in the top and bottom discs was to accommodate the optical fibers coupling light into and out of the cavity. Note also that this hole is positioned away from the center of the disk. The three HOD-300 quartz pieces are stacked on top of one another. The top and bottom discs are arranged so that these two single holes for the optical fibers are diametrically opposite.

Results and Discussion

Fig. XII.4 shows the reflectivity of an HOD-300 quartz cavity with $D = 10.16$ cm and $H = 5.72$ cm from 270 - 1050 nm compared with the quoted reflectivity from Spectralon SRM-90 [6, 41]. Limitations of the source due to the cut of the doubling crystal restricted our ability to measure the reflectivity between 350 and 400 nm. At these wavelengths, the signal was too small to be useful. HOD-300 exhibits a flat spectral distribution over most of the UV-VIS-NIR with the exception of 2 features centered around ~ 920 nm and ~ 360 nm. The drop in reflectivity can most likely be attributed to a small absorption within the quartz. The reflectivity variance is much less than $.001\%$. HOD-300 compares favorably with Spectralon especially when considering applications in the UV.

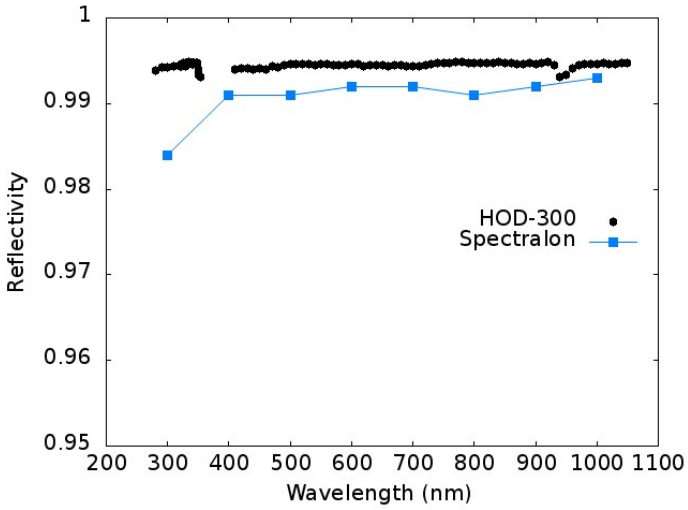

Figure XII.4: The reflectivity of an HOD-300 quartz cavity with D = 10.16 cm and H = 5.72 cm (circles) compared with the reflectivity of Spectralon (square)

While the reflectivity of HOD-300 does not yet match that of the fumed silica, the rigid and robust nature of these pieces offer a practical alternative. In addition, HOD-300 is easily machinable and, therefore, offers a larger array of practical configurations. For these reasons, in cases where the ultra-high reflectivity of fumed silica powder is not required, HOD-300 may prove to be a superior option. Alternatively, further efforts are being made to improve the reflectivity of HOD-300. Notice that in the SEM image of Fig.XII.5 the air pockets are moderately spaced with some notably large areas of continuous quartz. In these regions, light is able to propagate unimpeded for large distances without undergoing any reflection process. The major contribution to the difference in the diffuse reflectivity between the fumed silica and the HOD-300 is likely a combination of differences in the density of air-quartz interfaces and greater concentrations of trace contaminants in HOD-300 as opposed to the fumed silica powder. By increasing the number of air pockets in the HOD-300 pieces and improving the material purity, the reflectivity should be expected to significantly increase.

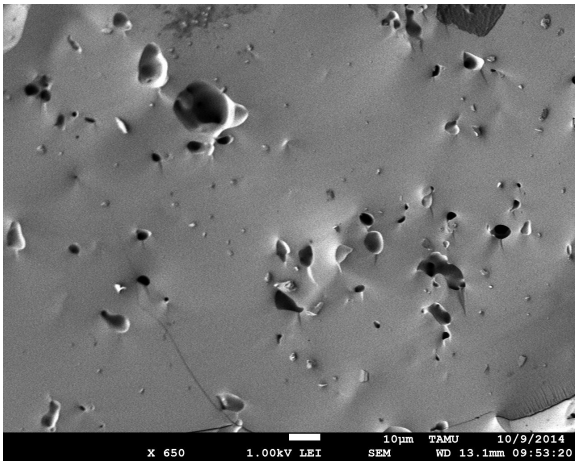

Figure XII.5: An SEM image of a piece of HOD-300. The small circular holes are approximately 1-10 μm in size and represent air bubbles intentionally engineered to create air-quartz interfaces.

Conclusions

The ubiquitous use of integrating cavities demonstrates the importance of continued innovation of new diffuse reflecting materials. HOD-300 has been demonstrated to have favorable characteristics compared to commercially available alternatives. The increased reflectivity in the UV-VIS range opens the door to new diffuse reflector applications. While the fumed silica powder has a superior reflectivity, the material stability of HOD-300 in various environments as well as the ability to mold and machine HOD-300 to different shapes and sizes offers a unique niche for varied applications.

CHAPTER XIII

SUMMARY AND CONCLUSIONS

The results presented in this dissertation research demonstrate the effectiveness of using fumed silica to measure the absorption spectrum of weakly absorbing samples with ICRDS and the ICAM. The high reflectivity of a fumed silica integrating cavity can significantly increase the path length of light through a sample. This increases the interaction between light and the sample enhancing phenomena such as absorption, Raman, and fluorescence. Furthermore, since light is scattered in all directions after any given bounce from the cavity wall, additional scattering from the sample has no impact on the light distribution inside the cavity. As a result, the absorption spectrum of a sample can be measured regardless of its scattering properties.

The improvements made by replacing the diffuse reflecting Spectralon with fumed silica have improved the sensitivity of the ICAM-II in ultraviolet and visible. The ICAM-II was used to measure pure water over the broad spectral range from 250-550 nm. The absorption measurements characterize a new minimum located at a wavelength of 344 nm with a value of 0.0008 m^{-1}. In the visible, the data agrees with the well-established literature for $\lambda > 420$ nm as well as $\lambda < 300$ nm. In addition, this dissertation presents the first known observation of 9^{th} harmonic of the O-H stretch of a water molecule.

Fumed silica cavities were further used to measure the absorption coefficient of many severely scattering samples. Through the use of ICRDS, the temporal domain of a decaying laser pulse was exploited to find the scattering-independent absorption spectrum of cells, living tissue, fixed tissue, and synthetic tissue. Several key absorption features were observed and characterized in each of these samples. These features correspond to well documented absorption phenomena such as the Soret band and heme structures.

Finally, we noted the characterization of new diffuse reflector made of solid quartz. While the effectiveness of the fumed silica powder is undeniable, the fragility of the material complicates the implementation of powder cavities for on-site sensing technologies. The new material, while having a lower reflectivity than fumed silica cavities, is an improvement over Spectralon, specifically in the ultraviolet.

REFERENCES

[1] K. Abe, Y. Hayato, T. Iida, M. Ikeda, C. Ishihara, K. Iyogi, J. Kameda, K. Kobayashi, Y. Koshio, Y. Kozuma, et al. Solar neutrino results in super-kamiokande-iii. *Physical Review D*, 83(5): 052010, 2011.

[2] N. Agmon. Tetrahedral displacement: The molecular mechanism behind the debye relaxation in water. *The Journal of Physical Chemistry*, 100(3): 1072–1080, 1996.

[3] D. Anderson, J. Frisch, and C. Masser. Mirror reflectometer based on optical cavity decay time. *Applied Optics*, 23: 1238–1245, 1984.

[4] V. Backman, R. Gurjar, K. Badizadegan, I. Itzkan, R. Dasari, L. Perelman, and M. Feld. Polarized light scattering spectroscopy for quantitative measurement of epithelial cellular structures in situ. *IEEE Journal of Selected Topics in Quantum Electronics*, 5(4): 1019–1026, 1999.

[5] H. Barthel, M. Heinemann, M. Stintz, and B. Wessely. Particle sizes of fumed silica. *Chemical Engineering & Technology*, 21: 745–752, 1998.

[6] J. Beaulieu. A guide to integrating sphere theory and applications. Technical report, Labsphere Inc., 1999, 2015.

[7] J. N. Bixler, M. T. Cone, B. H. Hokr, J. D. Mason, E. Figueroa, E. S. Fry, V. V. Yakovlev, and M. O. Scully. Ultrasensitive detection of waste products in water using fluorescence emission cavity-enhanced spectroscopy. *Proceedings of the National Academy of Sciences*, 111(20): 7208–7211, 2014.

[8] S. C. Boca, M. Potara, F. Toderas, O. Stephan, P. L. Baldeck, and S. Astilean. Uptake and biological effects of chitosan-capped gold nanoparticles on Chinese Hamster Ovary cells. *Materials Science and Engineering C*, 31(2): 184–189, 2011.

[9] C. F. Bohren and D. R. Huffman. *Absorption and Scattering of Light by Small Particles*. John Wiley & Sons, Inc., New York, NY, 1998.

[10] I. B. Butler, M. A. Schoonen, and D. T. Rickard. Removal of dissolved oxygen from water: a comparison of four common techniques. *Talanta*, 41(2): 211–215, 1994.

[11] M. I. Cabrera, O. M. Alfano, and A. E. Cassano. Absorption and Scattering Coefficients of Titanium Dioxide Particulate Suspensions in Water. *Journal of Physical Chemistry*, 100(51): 20043–20050, 1996.

[12] S. Chandrasekhar. *Radiative Transfer*. Dover Books on Intermediate and Advanced Mathematics. Dover Publications, 1960.

[13] W. F. Cheong, S. S. Prahl, and a. A. Welch. 1990.

[14] J. E. Cloern. The relative importance of light and nutrient limitation of phytoplankton growth: a simple index of coastal ecosystem sensitivity to nutrient enrichment. *Aquatic Ecology*, 33(1): 3–15, 1999.

[15] R. J. Cogdell. Carotenoids in photosynthesis. *Philosophical Transactions of the Royal Society of London B: Biological Sciences*, 284(1002): 569–579, 1978.

[16] M. T. Cone, J. D. Mason, E. Figueroa, B. H. Hokr, J. N. Bixler, C. C. Castellanos, G. D. Noojin, J. C. Wigle, B. A. Rockwell, V. V. Yakovlev, and E. S. Fry. Measuring the absorption coefficient of biological materials using integrating cavity ring-down spectroscopy. *Optica*, 2(2): 162–168, 2015.

[17] M. T. Cone, J. A. Musser, E. Figueroa, J. D. Mason, and E. S. Fry. Diffuse reflecting material for integrating cavity spectroscopy, including ring-down spectroscopy. *Applied Optics*, 54(2): 334, 2015.

[18] A. Corney. *Atomic and Laser Spectroscopy*. Clarendon Press, 2006.

[19] R. A. Cruz, A. Marcano, C. Jacinto, and T. Catunda. Ultrasensitive thermal lens spectroscopy of water. *Optics Letters*, 34(12): 1882–1884, Jun 2009.

[20] W. Demtröder. *Laser Spectroscopy*. Springer Publishing, Germany, 1996.

[21] P. Elterman. Integrating cavity spectroscopy. *Applied Optics*, 9(9): 2140–2142, 1970.

[22] R. Fernández-Prini and R. Dooley. Release on the refractive index of ordinary water substance as a function of wavelength, temperature and pressure. *International Association for the Properties of Water and Steam*, pages 1–7, 1997.

[23] C. J. Foot. *Atomic Physics*. Oxford University Press, New York, NY, 2005.

[24] E. S. Fry. Visible and near-ultraviolet absorption spectrum of liquid water: comment. *Applied Optics*, 39(16): 2743–2744, Jun 2000.

[25] E. S. Fry, G. W. Kattawar, and R. M. Pope. Integrating cavity absorption meter. *Applied Optics*, 31(12): 2055–2065, Apr 1992.

[26] E. S. Fry, J. Musser, G. W. Kattawar, and P.-w. Zhai. Integrating cavities: temporal response. *Applied Optics*, 45(August): 9053–9065, 2006.

[27] T. A. Germer, J. C. Zwinkels, and B. K. Tsai. *Spectrophotometry: Accurate Measurement of Optical Properties of Materials*, volume 46. Academic Press, 2014.

[28] J. A. Ghormley and C. J. Hochanadel. Production of hydrogen, hydroxide, and hydrogen peroxide in the flash photolysis of ice. *The Journal of Physical Chemistry*, 75(1): 40–44, 1971.

[29] M. Gouterman, G. H. Wagnière, and L. C. Snyder. Spectra of porphyrins : Part II. Four orbital model. *Journal of Molecular Spectroscopy*, 11(1-6): 108–127, 1963.

[30] D. F. Heath and G. Georgiev. *SPIE Optical Engineering and Applications*. International Society for Optics and Photonics, 2011.

[31] L. J. Heidt and A. M. Johnson. Optical study of the hydrates of molecular oxygen in water. *Journal of the American Chemical Society*, 79: 5587–5593, 1951.

[32] J. Herbelin and J. McKay. Development of laser mirrors of very high reflectivity using the cavity-attenuated phase-shift method. *Applied Optics*, 20: 3341–3344, 1981.

[33] B. H. Hokr, J. N. Bixler, M. T. Cone, J. D. Mason, H. T. Beier, G. D. Noojin, G. I. Petrov, L. A. Golovan, R. J. Thomas, B. A. Rockwell, and V. V. Yakovlev. Bright emission from a random raman laser. *Nature Communications*, 5, 2014.

[34] E. D. Industries. Product information: Aerosil eg50. Technical report, Evonik Industries, 2015.

[35] S. L. Jacques. Optical properties of biological tissues: a review. *Physics in Medicine and Biology*, 58(11): R37–61, 2013.

[36] M. Jonasz and G. Fournier. *Light Scattering by Particles in Water: Theoretical and Experimental Foundations*. Academic Press, 2011.

[37] M. Kalashnikov, W. Choi, C.-C. Yu, Y. Sung, R. R. Dasari, K. Badizadegan, and M. S. Feld. Assessing light scattering of intracellular organelles in single intact living cells. *Optics Express*, 17(22): 19674–81, 2009.

[38] H. G. Kjaergaard, B. R. Henry, H. Wei, S. Lefebvre, T. Carrington Jr, M. O. sonnich, and M. L. Sage. Calculation of vibrational fundamental and overtone band intensities of h20. *The Journal of Chemical Physics*, 100(9): 6228–6239, 1994.

[39] L. Kou, D. Labrie, and P. Chylek. Refractive indices of water and ice in the 0.65–2.5 μm spectral range. *Applied Optics*, 32: 3531–3540, 1993.

[40] L. Kröckel and M. A. Schmidt. Extinction properties of ultrapure water down to deep ultraviolet wavelengths. *Optics Materials Express*, 4(9): 1932–1942, Sep 2014.

[41] Labsphere. A guide to reflectance coatings and mateirals. Technical report, Labsphere Inc., 2006, 2015.

[42] Labsphere. A guide to reflectance coatings and materials. Technical report, Labsphere Inc., 2006, 2015.

[43] J. H. Lambert. *Lambert's Photometrie: Photometria, Sive De Mensura et Gradibus Luminus, Colorum et Umbrae*. Leipzig, 1760.

[44] C. Lance and W. D. Bonner. The respiratory chain components of higher plant mitochondria. *Plant physiology*, 1968.

[45] Z. P. Lee, K. L. Carder, and R. A. Arnone. Deriving inherent optical properties from water color: a multiband quasi-analytical algorithm for optically deep waters. *Applied Optics*, 41(27): 5755–5772, 2002.

[46] Z. Lee, J. Wei, K. Voss, M. Lewis, A. Bricaud, and Y. Huot. Hyperspectral absorption coefficient of "pure" seawater in the range of 350–550 nm inverted from remote sensing reflectance. *Applied Optics*, 54(3): 546–558, 2015.

[47] V. Ling, N. Kartner, T. Sudo, L. Siminovitch, and J. R. Riordan. Multidrug-resistance phenotype in Chinese hamster ovary cells. *Cancer Treatment Reports*, 67(10): 869–74, 1983.

[48] Z. Lu. *Optical Absorption of Pure Water in the Blue and Ultraviolet*. PhD thesis, Texas A&M University, 2006.

[49] I. H. Malitson. Interspeciment comparison of refractive index of fused silica. *Journal of the Optical Society of America*, 55(10): 1205–1209, Oct 1965.

[50] E. Millipore. Milli-q water purification systems range. Technical report, Millipore, 2007, 2016.

[51] A. Morel, B. Gentili, H. Claustre, M. Babin, A. Bricaud, J. Ras, and F. Tieche. Optical properties of the clearest natural waters. *Limnology and Oceanography*, 52(1): 217–229, 2007.

[52] T. Ohmi, A. Hogetsu, K. Ushikoshi, and M. Saito. June 1992. US Patent 5,124,033.

[53] A. O'Keefe and D. A. G. Deacon. Cavity ring-down optical spectrometer for absorption measurements using pulsed laser sources. *Review of Scientific Instruments*, 59(12): 2544–2551, 1988.

[54] J. M. Palmer and B. G. Grant. *The Art of Radiometry*, volume PM184. SPIE, 2009.

[55] C. Patel and A. Tam. Optical absorption coefficients of water. *Nature*, 1979.

[56] R. M. Pope and E. S. Fry. Absorption spectrum (380–700 nm) of pure water. ii. integrating cavity measurements. *Applied Optics*, 36(33): 8710–8723, Nov 1997.

[57] S. A. Prahl, M. J. C. van Gemert, and A. J. Welch. Determining the optical properties of turbid media by using the adding-doubling method. *Applied Optics*, 32(4): 559–568, 1993.

[58] R. W. Preisendorfer. *Hydrologic Optics*, volume 1 of *C&EE;135*. U.S. Dept. of Commerce, National Oceanic and Atmospheric Administration, Environmental Research Laboratories, Pacific Marine Environmental Laboratory, Honolulu, HI, 1976.

[59] T. T. Puck, D. Morkovin, P. I. Marcus, and S. J. Cieciura. Action of x-rays on mammalian cells. II. Survival curves of cells from normal human tissues. *The Journal of Experimental Medicine*, 106(4): 485–500, 1957.

[60] M. R. Querry, D. M. Wieliczka, and D. J. Segelstein. Water (H_2O). In *Handbook of Optical Constants of Solids II*, pages 1059–1077. Academic Press, 1991.

[61] T. I. Quickenden and J. A. Irvin. The ultraviolet absorption spectrum of liquid water. *Journal of Chemical Physics*, 72: 4416–4428, 1980.

[62] T. Quickenden and J. Irvin. The ultraviolet absorption spectrum of liquid water. *The Journal of Chemical Physics*, 72: 4416–4428, 1980.

[63] T. Rep. Universal arc lamp housing models 66000 through 66005. Technical report, Oriel Corporation, 1990.

[64] T. Rep. Dc arc lamps. Technical report, Oriel Corporation, 2016.

[65] T. Rep. Dk240 1/4 meter monochromator. Technical report, CVI Laser Optics, 2016.

[66] T. Rep. Liquid filters for light sources. Technical report, Oriel Corporation, 2016.

[67] T. Rep. Research arc lamp housings. Technical report, Oriel Corporation, 2016.

[68] O. Ryumyo and T. Takahashi. Vacuum uv absorption spectra of liquid water and ice. *Journal of the Physical Society of Japan*, 24(3): 548–550, 1968.

[69] H. Sasaki, B. Bothner, A. Dell, and M. Fukuda. Carbohydrate structure of erythropoietin expressed in Chinese hamster ovary cells by a human erythropoietin cDNA. *Journal of Biological Chemistry*, 262(25): 12059–12076, 1987.

[70] F. M. Sogandares. *The Spectral Absorption of Pure Water*. PhD thesis, Texas A&M University, August 1991.

[71] J. L. Soret. Analyse spectrale: sur le spectre d'absorption du sang dans la partie violette et ultraviolette. *Computes rendus de l'Académie de sciences*, 97: 1269–1270, 1883.

[72] P. Stanley, V. Caillibot, and L. Siminovitch. Selection and characterization of eight phenotypically distinct lines of lectin-resistant chinese hamster ovary cells. *Cell*, 6(2): 121–128, 1975.

[73] G. G. Stokes. On the intensity of the light reflected from or transmitted through a pile of plates. *Proceedings of the Royal Society of London, Philosophical Transactions of the Royal Society*, 11: 545 – 556, Jan, 1860.

[74] W. E. Sumpner. The direct measurement of the total light emitted from a lamp.

[75] H. A. Szymanski. *Volume 2 Raman Spectroscopy: Theory and Practice*. Plenum Press, New York, 1970.

[76] A. V. Tataurov, Y. You, and R. Owczarzy. Predicting ultraviolet spectrum of single stranded and double stranded deoxyribonucleic acids. *Biophysical Chemistry*, 133(1): 66–70, 2008.

[77] J. W. T. Walsh. *Photometry*. Constable and Co. Limited, London, third edition, 1953.

[78] L. Wang. *Measuring Optical Absorption Coefficient of Pure Water in UV Using the Integrating Cavity Absorption Meter*. PhD thesis, Texas A&M University, 2008.

[79] S. Weiss. Fluorescence spectroscopy of single biomolecules. *Science*, 283(5408): 1676–1683, 1999.

[80] J. D. Wilson, C. E. Bigelow, D. J. Calkins, and T. H. Foster. Light scattering from intact cells reports oxidative-stress-induced mitochondrial swelling. *Biophysical Journal*, 88(4): 2929–2938, 2005.

[81] B. Wozniak and J. Dera. *Light Absorption in Sea Water*. Springer, New York, New York, NY, 2007.

[82] P. Zalicki and R. N. Zare. Cavity ring-down spectroscopy for quantitative absorption measurements. *The Journal of Chemical Physics*, 102(7): 2708, 1995.